# Entropic Motors:
## Directed Motion without Energy Flow

Dissertation zur Erlangung des
mathematisch-naturwissenschaftlichen Doktorgrades

"Doctor rerum naturalium"

der Georg–August–Universität Göttingen

im Promotionsprogramm ProPhys
der Georg–August University School of Science (GAUSS)

vorgelegt von

Johannes Paul Blaschke

aus Lich, Hessen

Göttingen, 2014

Betreuungsausschuss:

apl Prof. Dr. Jürgen Vollmer
Max-Planck Institute for Dynamics and Self-Organization

apl Prof. Dr. Stephan Herminghaus
Max-Planck Institute for Dynamics and Self-Organization

Prof. Dr. Annette Zippelius
Georg-August-Universität Göttingen

Mitglieder der Prüfungskommission:

*Referent:* Prof. Dr. Reiner Kree
Georg-August-Universität Göttingen

*Korreferent:* apl Prof. Dr. Jürgen Vollmer
Max-Planck Institute for Dynamics and Self-Organization

Weitere Mitglieder der Prüfungskommission:

Prof. Dr. Annette Zippelius
Georg-August-Universität Göttingen

Prof. Dr. Devaraj van der Meer
University of Twente

apl Prof. Dr. Stephan Herminghaus
Max-Planck Institute for Dynamics and Self-Organization

Dr. Claus Heussinger
Georg-August-Universität Göttingen

**Tag der mündlichen Prüfung:**



[1] http://creativecommons.org/licenses/by/4.0/deed.en

# Abstract

Asymmetric test particles can rectify thermal fluctuations of impinging particles, if the test particles are not in equilibrium with their environment [2, 25, 42]. Due to this rectification, these test particles are called Brownian motors. One means of maintaining the Brownian motor out of equilibrium, is to introduce dissipation between impinging particles and Brownian motor.

So far, only Gaussian velocity distributions for the impinging particles have been considered [8, 12]. However, In order to maintain a steady state in the presence of dissipation, the impinging particles must have some sort of driving in order to replenish the energy that has been lost in collisions. This driving effects the velocity distribution of the impinging particles [53]. In this dissertation, we address the question: how do non-Gaussian velocity distributions affect the motion of the Brownian motor?

By considering an anisotropic velocity distribution for the impinging particles, we where able to identify a dimensionless parameter which identifies whether the anisotropy has an effect on the motor drift. In the regime where the anisotropy dominates the drift, a dramatic violation of equipartition has been observed.

When the impinging particles all have the same speed but random orientation, we found that the direction in which the motor drifts is a function of motor mass. We where able to identify a breakdown of ergodicity for motors which are lighter than the impinging particles.

In both cases, we found that the motor drift velocity approaches a constant value, independent of motor mass, in the limit of a massive motor. We have also found that rectification occurs even when there is no dissipation, we therefore argue that an entropy current, instead of an energy current, sustains motor drift.

*To Christin.*

# Contents

# Introduction

1

Brownian motors are devices capable of rectifying the fluctuations inherent to thermal systems [2, 25]. They are fascinating because, at first glance they seem to be capable of violating the second law of thermodynamics by turning thermal fluctuations into useful work. This is of course not the case! A Brownian motor is only capable of producing useful work when it is out of equilibrium with its environment.

One way of ensuring that a Brownian motor is out of equilibrium is to introduce a source of energy dissipation. Dry granular gasses, *i. e.* non-cohesive particles that dissipate energy upon collision [24, 30, 32], are a popular real-world systems exemplifying this mechanism. Since particles are macroscopic, and fabrication techniques allow for reasonably well defined material properties, studies can be carried out in the laboratory without needing extremely small, or large scales. Experimental and numerical studies have found a wide and fascinating range of phenomena, [4, 17, 38, 45] for just a few examples. Common to many of these experimental and numerical studies is that the granular gas is kept in a (far-from-equilibrium) steady state by shaking the container or its walls. This has the effect that the velocity distribution of the granular gas is non-Gaussian [53]. Another recent study has found rectification of a cog driven by impinging swimmers [15]. Here the distribution deviates from a Gaussian even more than a granular gas, as the swimmers have a narrow range of speeds.

This work examines the motion of asymmetric test particles, Brownian motors, that are immersed in a gas whose velocities are sampled from a non-Gaussian distribution. We ask the question: what is the effect of the non-Gaussian distribution on the motion of the motors?

## 1.1 Previous work

The present work was inspired by, and builds upon a number of studies addressing the motion of an asymmetric test particle undergoing random collisions with a bath. Here we shall give a short review of several non–equilibrium model systems that are relevant to Brownian motors.

### 1.1.1 *The Adiabatic Piston*

The adiabatic piston [23, 39] consists of a piston which moves without friction and does not conduct heat. The piston separates two reservoirs of different gasses, often modelled as hard–core gases.

The relevant question is: if the two gasses are not in thermodynamic equilibrium when the piston is released from rest, in which direction does the piston move? If the pressure of both gasses is the same, then classical thermodynamics makes no prediction about the motion of the piston.

This makes sense, when the pressures are identical, the system is in mechanical equilibrium, and so there is no net force (over time) acting on the piston. The only motion that remains are the tiny kicks that the piston receives from the gas.

This is problematic to thermodynamics, as it does not treat the gas atomistically. And so, thermodynamics cannot make any statements about the eventual motion of the piston [23].

Recalling that the piston moves without friction, and so it can be moved by atomic/molecular collisions. Then the question remains: in which direction, if at all, does the piston move? This was considered one of the controversial physical questions until still quite recently [39]. The answer is remarkable: the tiny kicks from the gas, cause the piston to fluctuate in the same way as the thermal fluctuations of the gas. Hence the piston's motion conducts heat, even though it is made up of a perfect insulator. This heat flow, via the piston's motion, equilibrate the gasses temperature. In the process the piston move *towards to hotter reservoir* [14, 21, 23, 39].

This basic model therefore elucidated the importance of addressing fluctuations, in order to understand the mean motion of objects in contact with heat baths.

### 1.1.2 *Brownian Motors*

The Brownian motor (or Feynman–Smoluchowski ratchet) is a basic Gedankenexperiment aimed at rectifying the random fluctuations of molecular statistical mechanics [31].

The idea is very simple, a ratchet–and–pawl mechanism is used to ensure a paddle–wheel can only turn in one direction. If the paddle–wheel is immersed in a gas of molecules, some collision would turn it into the allowed direction. Normally a paddle–wheel would not begin spinning on its own this way, as collisions turning it clockwise and anti–clockwise would average out over time. With the ratchet–and–pawl mechanism, this devices should spin in one direction all due to the thermal fluctuations in the molecular gas.

However, the full mathematical treatment [31] shows the pawl fluctuating also. In equilibrium, the pawl therefore skips equally many otherwise forbidden turns as it allows allowed turns.

Even though it did not yield a perpetuum-mobile, this Gedanken-experiment did open the door to the field of Brownian motors. If the Feynmman–Smoluchowski ratchet was, in some manner, kept out of equilibrium from its environment, then the device can be used to rectify the thermal fluctuations of the environment [1, 2, 25, 42, 51, 52].

In principle, all that is needed is spacial asymmetry, and time-reversal asymmetry. The former was supplied by the ratchet-and-pawl mechanism. And the latter is supplied by the non-equilibrium condition. Since a wide class of physical system can be used to perform rectification of thermal fluctuations this way, the term "Brownian-motor" is used to describe them.

### *1.1.3 Granular Brownian Motors*

Inelastic collisions with the wedge, lead to a finite steady–state drift of the wedge's position [8]. If the coefficient of restitution varies over the surface of the wedge, this drift can be enhanced [12]. These systems, where a finite steady–state drift is achieved via inelastic collisions have been called *granular Brownian motors* [11, 12, 22, 28]. A granular version of the Feynman-Smoluchowski ratchet has been also examined in the laboratory [18, 28].

Furthermore, since the state of the granular gas can be observed directly [16, 17] some of the physical mechanisms, such as convection are directly accessible to experimental observation.

Dissipative collisions are normally modelled using a coefficient of restitution [24, 29, 47]. This simple model captures the inelastic collisions, by removing a fraction of the normal component of the particle's relative velocity.

Here we shall consider a very basic geometry which breaks reflection symmetry: a triangular wedge[1], constrained to move in the horizontal direction only. When the wedge experiences elastic collisions, there is a finite transient drift as the motor approaches thermal equilibrium with the gas [50].

1. This breaks reflection symmetry in the horizontal direction, because the wedge is oriented so the horizontal axis goes through only one tip

### *1.1.4 Bacterial Brownian Motor*

A recent study observed that an asymmetric cog, driven by collisions with E. Coli bacterial, develops a finite steady-state speed of rotation [15]. This has been proposed as a means of stochastically driving microscopic machines.

## 1.2 THE AIM OF THE PRESENT WORK

So far, pertinent theoretical studies addressing these motors are based on thermostatted gasses. Impacting particles are sampled from a Gaussian velocity distribution. When thermostatting via

stochastic forcing, this is a reasonable assumption [12]. On the other hand, experimental realizations of granular gasses typically exhibit sustained heterogeneities in density and granular temperature [10, 16, 17, 45, 46]. Moreover, when shaking in the plane of observation, they exhibit noticeable anisotropy of the granular temperature [53]. Consequentially we denote them as anisotropic gasses.

The fact that the velocity distribution of a granular gas does not follow a Gaussian distribution is not surprising. After all, we expect a Gaussian velocity distribution in local equilibrium. The studies on the motion of a granular Brownian motor in an isotropic gas [8, 12] have shed an important light on the nature of a system out of equilibrium due to dissipation. We see that, due to the constant flow of energy being dissipated, some velocity fluctuations of the wedge's motion are rectified to produce finite steady-state drift. Here we explore the additional effects of anisotropy on the motion of the granular motor is.

An anisotropic gas can still be considered near equilibrium. After all, if the anisotropy is mild, then the deviation from the Gaussian distribution is just a small perturbation. Hence we will complement our findings by examining an extreme case of a non–equilibrium system: a gas of self–propelling swimmers.

We will take an important step towards bridging the gap between theory and experiment for both granular and bacterial Brownian motors.

## 1.3 OVERVIEW

This work is structured into 3 principal chapters giving an exposition of the central results. In the results chapters of this dissertation, we will address two model systems for the gas:

1. A gas whose particle velocities are sampled from a squeezed Gaussian distribution;

2. A gas where all particles have the same speed, but random orientation.

### *1.3.1 Chapter 2: Model System*

In chapter 2 we introduce the model systems used throughout the present work. The mathematical notations and conventions are also presented here.

### *1.3.2 Chapter 3: Kinetic Theory*

Much of this work relies on the kinetic theory of Markov processes. In chapter 3, we introduce the basic features of Markov processes.

Then we proceed to review a computer algorithm which efficiently computes the time evolution of such processes.

We then proceed onto the master equation, that is how velocity probability density function may be calculated from the single-collision equations of motion and the statistics of encountering a specific collision. The method presented here is a generalization of the published approach [35], allowing it to be applied to a wider range of problems. It allows us to determine the moments of the motor velocity probability density function.

### *1.3.3 Chapter 4: Kinetic Theory for a Granular Brownian Motor in an Anisotropic Granular Gas*

Up to now, the kinetic theory had not explicitly addressed the particle velocity probability density function, $\phi$. In chapter 4 the method of moment-hierarchies is used to show that rectification occurs when $\phi$ is a squeezed Gaussian. The asymptotic analysis for a massive motor is used to introduce a dimensionless number which serves as a faithful criterion for whether rectification is due to dissipative collisions, or due to anisotropy.

In the traditional study of Brownian motor, the usual explanation for rectification is that the motor is out of equilibrium with the gas since dissipation ensures that the motor's temperature is lower than that of the gas. Surprisingly, rectification due to anisotropy occurs even when the motor is almost at the same temperature as the gas. We argue that this kind of rectification is due to the flow of *entropy*, rather than *energy*.

### *1.3.4 Chapter 5: Brownian Motor in a Bath of Swimmers*

Inspired by this insight into rectification due to entropy flow, rather than energy, chapter 5 addresses a model where the particles have identical energy (and therefore speed) but move with uniformly random orientation. This provides interesting theoretical challenges, since the transition rates are no longer defined on a convex surface. The kinetic theory for this system requires the treatment of the partitioned phase space, discussed in the chapter on the kinetic theory. As an alternative to the kinetic theory, the beginnings of the path integral treatment are also motivated at this point.

We find rectification of the velocity fluctuations here as well. Contrary to the previous chapter, though, we find that the direction of the motor drift depends on the mass ratio between motor and gas particles. Furthermore, realizations of motor trajectories show that the first moment of the velocity probability distribution of the motor no longer corresponds to the motor's average displacement per unit time when the motor mass is less than the swimmer's mass.

# Model of the Brownian Motor and Mathematical Conventions

2

In this chapter, we shall review the basic elements of the model system used whenever performing explicit calculations. This is followed by an introduction to the mathematical conventions and notation used throughout this work.

## 2.1 Model

Central to this work is the study of asymmetric objects, whose motion is driven by collisions with gas particles. For brevity, we refer to the asymmetric object as the *motor*, and the gas particles simply as *particles*.

In this introduction we shall give a general description of our model system (cf. [8] for the original publication). That is, the geometry of the motor, and its interaction with the gas particles. The velocity distribution function of the particles will be discussed in chapters 4, and 5.

### *2.1.1 Motor*

The motor is taken to be a smooth 2-dimensional wedge, with wedge angle $2\theta_0$ and mass, $\tilde{M}$. It is allowed to move only in one direction,

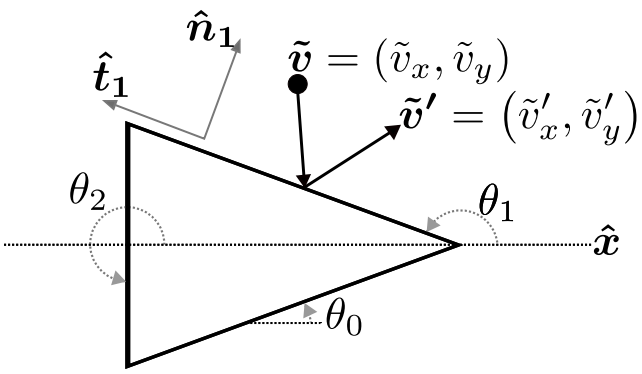


Figure 2.1: A particle (black circle) colliding with the Brownian motor (triangular wedge with wedge angle $2\theta_0$). The angles of the edges, $i \in \{0, 1, 2\}$, are measured counter-clockwise from the positive $\hat{x}$-axis to the *outside* of the motor, yielding $\theta_0$, $\theta_1 = \pi - \theta_0$, and $\theta_2 = 3\pi/2$, respectively.

which we take to be the $\hat{x}$-axis. Fig. 2.1 gives a simple sketch of this. The motor will move freely with velocity $\boldsymbol{V} = V\hat{e}_x$ between collisions. Hence the state of the motor can be characterized by $(x, V)$, where $x$ is the motor's position.

The length of the $n$-th side is given by

$$w_0 = w_1 = \frac{1}{2(1+\sin\theta_0)} \qquad w_2 = \frac{\sin\theta_0}{1+\sin\theta_0} \tag{2.1}$$

where the total length has been normalized such that $w_1 + w_2 + w_3 = 1$. Under the assumption of molecular chaos[1] [33], and since the total side length is 1, the probability of a particle striking side $i$ is equal to its length.

1. Also called Stosszahlansatz

### 2.1.2 *Gas*

Gas particles have mass, $\tilde{m}$, and velocity $\tilde{\boldsymbol{v}} = (\tilde{v}_x, \tilde{v}_y)$. Different gas baths have been examined throughout this work, the exact nature of the gas bath will be addressed at the appropriate time. We do assume that there exists an energy scale, allowing particle velocities to be non-dimensionalized: $\boldsymbol{v} = (v_x, v_y)$. Henceforth, velocities without a tilde represent the non-dimensionalized velocities, obtained via this energy scale.

From a mathematical point of view, the gas bath will enter the theory through the gas particle velocity distribution: $\phi(v_x, v_y)$. In order to avoid the complexity of the Boltzmann equation, the gas particle velocities are thermostated such that their velocities always resemble the distribution $\phi$. We refrain from modifying the theory so that it includes feedback of the motor on the gas is possible. It is possible in principle. However, this amounts to significant technical complexity, without promising new insights.

### 2.1.3 *Motor-Gas Interaction*

A collision event is illustrated in Fig. 2.1. Collision rules depend on which side of the motor, $i \in \{0, 1, 2\}$, is being impacted and on the coefficient of restitution, $r$. Since the motor's surface is perfectly smooth, there is no change in the tangential component of the gas particles velocity,

$$\boldsymbol{v}' \cdot \hat{\boldsymbol{t}}_{\boldsymbol{i}} = \boldsymbol{v} \cdot \hat{\boldsymbol{t}}_{\boldsymbol{i}} \,, \tag{2.2a}$$

where $\hat{\boldsymbol{t}}_i = (\cos\theta_i, \sin\theta_i)$ is the tangential vector to the surface being impacted[2]. In contrast, due to restitution the reflection law for the normal direction becomes,

$$(\boldsymbol{V}' - \boldsymbol{v}') \cdot \hat{\boldsymbol{n}}_{\boldsymbol{i}} = -r\,(\boldsymbol{V} - \boldsymbol{v}) \cdot \hat{\boldsymbol{n}}_{\boldsymbol{i}} \,, \tag{2.2b}$$

where $\hat{\boldsymbol{n}}_{\boldsymbol{i}} = (\sin\theta_i, -\cos\theta_i)$ is the normal vector. Single collisions obey conservation of momentum,

$$v_x' + \mathcal{M}V' = v_x + \mathcal{M}V \,, \tag{2.2c}$$

2. Note that indexing vectors do not represent the vector's components

where $\mathcal{M} := \tilde{M}/\tilde{m}$ is the mass ratio. Altogether Eqs. (2.2) determine the change in the motor velocity,

$$u_i := V' - V = \gamma_i \left( v_x - V - v_y \cot \theta_i \right) \ , \tag{2.3a}$$

where

$$\gamma_i \equiv \gamma(r, \mathcal{M}, \theta_i) := (1 + r) \frac{\sin^2 \theta_i}{\mathcal{M} + \sin^2 \theta_i} \ . \tag{2.3b}$$

## 2.2 NOTATIONS

Here I shall summarize the mathematical notation used throughout this work. This sections serves to make the reader familiar with the conventions used in the present work, and to introduce those conventions that are not widely used.

### *2.2.1 Symbols*

#### *2.2.1.1 In-line Division*

When specifying the fraction

$$\frac{x}{yz} \tag{2.4}$$

within text, then Eq. (2.4) becomes $x/yz$. Everything to the *right of the division sign* is to be considered in the denominator, until the next addition or subtraction operation.

#### *2.2.1.2 Place holders*

The symbol $\bullet$ will be used as a generic place holder. It shall be used in place of arguments, indices, and expressions when these are not relevant to the text discussed. For example, say there are two quantities $x_\mathrm{A}$ and $x_\mathrm{B}$ being discussed. The statement $x_\bullet > 0$ is to be read as "both $x_\mathrm{A} > 0$ and $x_\mathrm{B} > 0$".

#### *2.2.1.3 Sets*

Important sets are denoted using the black-board-bold[3] symbols. Any symbol displayed using this font is a set.

3. LaTeX: `\mathbb`

**Definition 1** The following symbols are reserved for specific sets:

*Real numbers*: These are denoted by $\mathbb{R}$.

*Indexing set*: A set for counting members of a family is denoted by $\mathbb{I}$. This is by definition countable, but not necessarily finite.

**Definition 2** Let $\mathbb{X}$ be a set. The subset of *positive* values is denoted by

$$\mathbb{X}^+ := \{x \in \mathbb{X} \mid x \geq 0\} \tag{2.5a}$$

and the subset of *negative* values is denoted by

$$\mathbb{X}^- := \{x \in \mathbb{X} \mid x \leq 0\} \tag{2.5b}$$

Within the context of this work, most sets of continuous quantities are intervals. These can either be either connected, or the union of disconnected intervals. Here there basic notation for addressing such sets is introduced.

**Definition 3** Let $\Omega$ be a set. We say that $\Omega$ can be *partitioned*, if it can be written as a disjoint union of countably many sets $\Omega_i$, that is

$$\Omega = \bigsqcup_{i \in \mathbb{I}} \Omega_i \tag{2.6}$$

If each $\Omega_i$ is an interval, we say that $\Omega$ can be *partitioned into intervals*.

**Definition 4** Let $\Omega$ be a set. Then the set $\partial\Omega$ is the *boundary* of $\Omega$. If $\Omega$ can be partitioned into intervals, then

$$\partial\Omega := \bigcup_{i \in \mathbb{I}} \partial\Omega_i \tag{2.7}$$

**Definition 5** Say the set $\Omega$ can be partitioned into intervals. Let $x \in \partial\Omega_i \subset \partial\Omega$, then we define the function

$$\mathrm{bnd}(x) = \begin{cases} 1 & \text{if } x \text{ is the upper bound of } \partial\Omega_i \\ -1 & \text{if } x \text{ is the lower bound of } \partial\Omega_i \end{cases} \tag{2.8}$$

**Definition 6** Say the set $\Omega$ can be partitioned into intervals and let $f$ be a function defined on the boundary of $\Omega$. Then we write $f$, evaluated on the boundary of $\Omega$ as

$$f(x)|_{\partial\Omega} := \sum_{x \in \partial\Omega} \mathrm{bnd}(x) f(x) \tag{2.9}$$

#### *2.2.1.4 Vectors*

Vectors shall be displayed as bold symbols. Hence $\boldsymbol{v}$ is a vector. Furthermore, hatted vectors are unit vectors.

**Definition 7** Let $\boldsymbol{v}$ be a vector, then $\hat{\boldsymbol{v}}$ is the unit vector pointing in the direction of $\boldsymbol{v}$. The unit vectors forming the basis of the Cartesian coordinate system are denoted by $\hat{\boldsymbol{e}}_{\boldsymbol{x}}$, $\hat{\boldsymbol{e}}_{\boldsymbol{y}}$, $\hat{\boldsymbol{e}}_{\boldsymbol{z}}$, and so on.

#### 2.2.1.5 Dimensionless Units

In this work, the models are non-dimensionalized before being treated mathematically. Hence, most quantities encountered will be dimensionless quantities. Quantities with a tilde will represent quantities with physical dimension. The plain counterparts are their non-dimensionalized form.

**Definition 8** Let $\tilde{x}$ be a variable in a model. The tilde denotes that it has a physical dimension. The non-dimensionalized counterpart will be written without the tilde, $x$.

Since the nature of non-dimensionalization is dependent on the model used, the relationship of dimensionless quantities to their dimensional counterparts will be addressed wherever appropriated.

### 2.2.2 Integration and Transforms

#### 2.2.2.1 Integral Boundaries

For integration boundaries we employ the notation where the integration domain is represented as subscript of the integral sign.

**Definition 9** Let $(\mathbb{X}, \Sigma, \mu)$ be a measure space. Let $f$ be a measurable function with respect the this measure. Let $A \subset \mathbb{X}$, then the integral of $f$ over $A$ with respect to the measure $\mu$ is denoted as

$$\int_A f \, \mathrm{d}\mu \tag{2.10}$$

This way we can save considerable effort, especially when partitioning $\mathbb{X}$.

**Remark 1** The integral over the entire real line, $\int_{-\infty}^{\infty} \bullet \, \mathrm{d}\mu$ is now simply $\int_{\mathbb{R}} \bullet \, \mathrm{d}\mu$. Likewise, the integral over an interval $\Omega \subset \mathbb{R}$ is written as $\int_{\Omega} \bullet \, \mathrm{d}\mu$.

#### 2.2.2.2 Characteristic Function and Moments

Integral transforms, such as the Fourier transform are represented by writing the transformed space coordinate as $k$ and the transformed time coordinate as $\omega$.

**Definition 10** Let $f(x, y)$ be a distribution. Provided it exists, its *characteristic function* with respect to $y$ is written as $f(x, k)$. Such that:

$$f(x, k) = \int_{\mathbb{R}} \mathrm{e}^{\mathrm{i}yk} f(x, y) \, \mathrm{d}y \tag{2.11}$$

**Definition 11** Let $f(x)$ be a probability density function. The $k$-th *moment* is defined as:

$$M_k := \int_{\mathbb{R}} x^k f(x)\,\mathrm{d}x \tag{2.12}$$

**Remark 2** The moments of the probability density function, $f(x)$, are related to the characteristic function via the derivatives:

$$M_n = \partial_{\mathrm{i}k}^n f(k)|_{k=0} \tag{2.13}$$

**Remark 3** The cumulants of the probability density function, $f(x)$, are related to the characteristic function via the derivatives:

$$\kappa_n = \partial_{\mathrm{i}k}^n \ln f(k)|_{k=0} \tag{2.14}$$

**Definition 12** Let $f(x)$ be a probability density function. The $k$-th *partial moments over* $\Omega \subset \mathbb{R}$ are defined as

$$M_{k,\Omega} := \int_{\Omega} x^k f(x)\,\mathrm{d}x \tag{2.15}$$

### *2.2.3 Special Functions*

#### *2.2.3.1 Brackets*

**Definition 13** Let $f$ be a probability density function. Angled brackets represent expectation values. Angled brackets without subscript are assumed to be taken over the whole domain of $f$. Without loss of generality, we assume that this domain is $\mathbb{R}$.

$$\langle g(x) \rangle := \int_{\mathbb{R}} g(x) f(x)\,\mathrm{d}x \tag{2.16a}$$

A subscript, $\Omega \subset \mathcal{R}$ represents the domain of the integral making up the expectation value operator:

$$\langle g(x) \rangle_{\Omega} := \int_{\Omega} g(x) f(x)\,\mathrm{d}x \tag{2.16b}$$

**Definition 14** Let $\mathcal{S}$ be a statement that is either true or false. We define the *Iverson bracket* as:

$$[\![\mathcal{S}]\!] := \begin{cases} 1 & \text{if } \mathcal{S} \text{ is True} \\ 0 & \text{if } \mathcal{S} \text{ is False} \end{cases} \tag{2.17}$$

**Remark 4** The Iverson bracket constitutes a convenient building block for many other distributions. Some examples of note are:

Kronecker delta: $\delta_{i,j} = [\![i = j]\!]$

Heaviside theta function: $\theta(x) = [\![x > 0]\!]$

Indexing function: $\mathbf{1}_A(x) = [\![x \in A]\!]$

In the absence of spatial correlations, particle collision rates are proportional to relative velocity. However, when the velocity is negative particles are moving away from each other, and so the collision frequency should be zero. The collision rate is hence a ramp function with respect to relative velocity. We therefore save time by employing the notation of the Macaulay bracket.

**Definition 15** Let $x \in \mathbb{R}$, then we define the *Macaulay bracket* as:

$$\langle\!\langle x \rangle\!\rangle := x\,[\![x > 0]\!] \tag{2.18}$$

#### *2.2.3.2 Distributions*

**Definition 16** We write the Dirac-$\delta$ function as $\delta[\bullet]$.

### *2.2.4 Limiting Relations*

We adopt the following consistent notation for *proportionality*, *asymptotic behaviour* and *leading order of an expansion*.

The symbol, $\sim$, is used to indicate that two quantities are proportional. Frequently this would be used when the coefficients of an expression have been dropped.

**Definition 17** Let $x$ and $y$ be two quantities that are proportional to one another. Then we write $x \sim y$.

The symbol, $\asymp$ is used to mean that the "asymptotic behaviour" of one function is that of the other. How quickly the asymptotics are reached is not specified.

**Definition 18** Let $f$ and $g$ be functions such that $f$ asymptotically approaches $g$ in the limit of some parameter $x \to \infty$. We write this as $f \asymp g$.

**Remark 5** If $f$ can be expanded as a power series, then $g$ is not only the lowest order term of this power series, but any function that is asymptotically approached.

Finally, the symbol $\simeq$ in conjunction with a power series expansion is used to show the "leading order" behaviour of a function. To which order is being considered can be seen by the order of the expansion.

**Definition 19** Let $f$ be a function that can be represented as a power series in terms of $x$,

$$f(x) = \sum_{i=0}^{\infty} a_i x^i \ . \tag{2.19}$$

Then we write the leading order(s) of this expansion as $f(x) \simeq a_0 + a_1 x + a_2 x^2 + \cdots + a_n x^n$.

# Kinetic Theory of the Model

3

In this chapter, we shall review the kinetic theory approach employed. For specified distributions of the gas particle velocities, we solve for the stochastic motion of the motor, and its velocity probability density function. We do this in 4 steps:

1. We introduce Markovian dynamics.
2. We discuss the means of resolving the motor's time-dependent position and velocity[1] by stochastically sampling velocity changes.
3. We review the Kramers–Moyal expansion, which allows the integro-differential master equation to be reduced to an infinite order, non-linear differential equation.
4. We show how this may be further reduced to a linear system of equations describing the moments of the velocity probability density function.

1. Also called "tracking" the motor's trajectory.

In the appendix, we review how a distribution can be approximated from its moments.

## 3.1 Markovian dynamics

Fig. 3.1 shows an illustration of the stochastic dynamics of the motor. At random times, a collision occurs. This changes the velocity discontinuously by $u = V_2 - V_1$.

A central consequence of molecular chaos is that the motor follows Markovian dynamics [20]. Given a motor velocity $V$, we write the transition rate of a collision resulting in a change of velocity $V \to V + u$ as $W(V; u)$. The central feature of a Markovian process is that the transition rates $W(V; u)$ depend only on the state $V$ and not the motor's history, $(V_n, V_{n-1}, \cdots)$.

Throughout this work, $W$ will frequently be written in the form $W(\text{state}\,;\text{change in state})$. Sometimes, it is more convenient to use

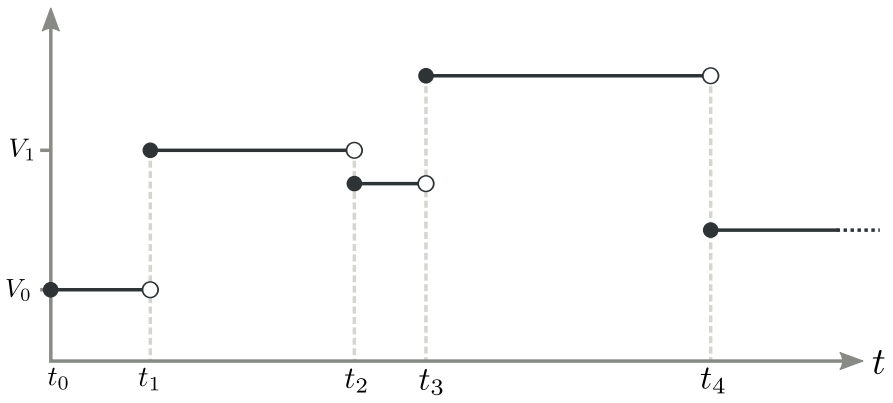


Figure 3.1: Illustration of the time evolution of the motor velocity. At random times, $t_n$, a collision changes the motor velocity discontinuously. Digram reprinted and modified from [54], with the author's consent.

the notation $W(\text{state} \to \text{next state})$. The conversion between the two is trivial:

$$W(x_n \to x_{n+1}) := W(x_n; x_{n+1} - x_n) \,. \tag{3.1}$$

Note that $W(x_1 \to x_2)$ is a collision *rate*. That is, the quantity

$$\int_{\mathbb{R}} W(x_1 \to x_2)\, \mathrm{d}x_2 = a_0(x_1) \tag{3.2}$$

is the collision rate[2] experienced while in the state $x_1$. The transition rates may now be easily converted to transition probabilities

$$\mathcal{P}(x_1 \to x_2) := \frac{W(x_1 \to x_2)}{a_0(x_1)} \,. \tag{3.3}$$

For a Markov process, the probability of observing a trajectory consisting of the transitions $x_1 \to \cdots \to x_n$ factorizes into the transition probabilities for each individual transition,

$$\mathcal{P}_n\left(x_1 \to \cdots \to x_n\right) = \mathcal{P}\left(x_1 \to x_2\right) \mathcal{P}\left(x_2 \to x_3\right) \cdots \mathcal{P}\left(x_{n-1} \to x_n\right) \,. \tag{3.4}$$

This is also called the *Markov property*. Consequently, the probability of observing a trajectory $(x_1, x_2, \cdots, x_n)$ is simply

$$P\left(x_1, x_2, \cdots, x_n\right) = P(x_1) \mathcal{P}_n\left(x_1 \to \cdots \to x_n\right) \,. \tag{3.5}$$

Here $P(x_1)$ is the probability of observing state $x_1$.

The subscript $n$ denotes that this trajectory consists of $n$ transitions[3]. The probability of observing any transition from $x_1 \to x_n$ consisting of exactly $n$ steps is given by integrating Eq. (3.4) over all intermediary steps,

$$\mathcal{P}_n\left(x_1 \to x_n\right) = \underbrace{\int_{\mathbb{R}} \cdots \int_{\mathbb{R}}}_{n-2 \text{ many}} \mathcal{P}_n\left(x_1 \to \cdots \to x_n\right) \underbrace{\mathrm{d}x_2 \cdots \mathrm{d}x_{n-1}}_{n-2 \text{ many}} \tag{3.6a}$$

$$= \int \mathcal{D}\boldsymbol{x}\; \mathcal{P}_n\left(x_1 \to \cdots \to x_n\right) \tag{3.6b}$$

2. Also called the *escape rate*.

3. Technically $\mathcal{P}(x_1 \to x_2)$ should have a subscript 1, but this has been dropped as it is self–evident

which is a path integral over all possible ways to get from $x_1$ to $x_n$. Eq. (3.6a) is the explicit integral over all intermediate values, and Eq. (3.6b) is the same integral written in path integral notation, where $\boldsymbol{x} := (x_2, \cdots, x_{n-1})$.

## 3.2 MOTOR TRAJECTORIES

The path integral, Eq. (3.6b) cannot be solved analytically in general. Instead, direct numerical solutions are possible, by using Monte-Carlo techniques to find realizations of paths corresponding to the transition probabilities Eq. (3.3).

The method of Monte-Carlo integration has two principal steps:

1. Many states, sampled from an initial distribution, are evolved using the transition probabilities, Eq. (3.3).

2. To find the final density $P(V,t)$, the result of step 1 is histogrammed.

Step 1 requires an appropriate time discretization. This is granted because collisions between motor and particles depend only on the motor's instantaneous velocity $V$. More precisely, the rate at which collisions take place given a motor velocity $V$ is $a_0(V) := \int_{\mathbb{R}} W(V;u)\,\mathrm{d}u$. Hence the probability, $P_0(t;V)$, that a collision *does not* take place within a time interval $t$ is given by the Poisson statistics:

$$P_0(t;V) = a_0(V)\,\mathrm{e}^{-a_0(V)t}\ . \tag{3.7}$$

Sampling the free-flight time between collisions from Eq. (3.7) provides us with a very natural time discretization.

Even though the time of free flight between collisions does not explicitly depend on the history of previous collisions, this is not quite *independence*. A prior collision which caused a change in velocity $V \to V+u$ does influence the likelihood of the next collision by having changed $V$. After all, we are modelling the collisions between motor and gas as a Markovian process.

### *3.2.1 Slice Sampling*

Sampling collisions from Eq. (3.4) requires an algorithm that can sample from an arbitrary distribution.

Broadly speaking, algorithms for sampling pseudo-random numbers work by first generating uniformly distributed pseudo-random numbers. Then these uniform pseudo-random numbers are transformed so that they have the desired statistics. In general, this is achieved in one of the following three ways:

1. Inverse transform sampling, which transforms sampled pseudo-random numbers by inverting the cumulative probability function.

2. Rejection sampling which transforms pseudo-random numbers by accepting only those numbers which fulfil a prescribed condition.

3. Markov-chain Monte-Carlo methods which solves a stochastic process chosen such that its invariant distribution coincides with the desired distribution.

Category (1.) and (2.) algorithms are computationally efficient for a certain distributions. They cannot, however, produce pseudo-random numbers with arbitrary desired statistics. This is precisely what we need so solve the stochastic process prescribed by Eq. (3.9).

Category (3.) algorithms can cope with a very large range of distribution, yet they produce serially-dependent pseudo-random numbers. If the goal is to sample independent pseudo-random numbers, as is the case for this work, an algorithm whose sampled pseudo-random numbers decorrelate quickly is desired. The slice-sampling algorithm [37] has been chosen for this reason.

Slice-sampling is a Markov-chain sampling algorithm, meaning that it produces the next pseudo–random number given the current one. These sampled pseudo-random numbers are not independent. Yet they tend to decorrelate faster than those produced by the Metropolis–Hastings algorithm[4]. This is because, unlike the Metropolis–Hastings algorithm, slice-sampling adapts its step size to the local shape of the desired Distribution. Especially in the presence of intervals where the desired distribution goes to zeros, slice-sampling avoids bottlenecks, where the Metropolis–Hastings algorithm's output would produce long correlation times.

4. Which is a frequently chosen algorithm in the statistical physics community.

The algorithm is based on a very simple principle: if we sampled points $(x, y) \in \mathbb{R}^2$ uniformly[5] with $y > 0$, and rejected all those not below the graph of the distribution, then we would produce pseudo-random numbers with the desired distribution. Of course, no one should use this kind of algorithm: if the desired distribution deviates significantly form the uniform distribution this algorithm would waste a large amount of pseudo-random numbers.

5. For the purposes of this illustration we shall ignore the fact that this is impossible in reality as $\mathbb{R}^2$ is not bounded.

Instead, slice-sampling divides the distribution, $P(x)$, into infinitely thin horizontal slices. A slice is picked uniformly at random, followed by uniformly sampling an $x$-coordinate from within the slice. In order to pick the slice, one samples the $y$-coordinate from the interval $(0, P(x)]$ uniformly, where $x$ is the previously sampled $x$-coordinate. If the boundary of each slice is known precisely, then no random numbers are wasted at all. Otherwise, if only upper bounds are known, then rejected sampling is used to determine the $x$-coordinate.

Algorithm 1, below, details the pseudo-code used to implement the slice-sampling method used in this work. Here $P(u)$ is the probability that a collision results in a change in motor velocity from $V \to V + u$, given the instantaneous motor velocity $V$. It is related to the transition rates by Eq. (3.3)

**Algorithm 1** Sample $x$, the next pseudo-random number in a sequence of pseudo-random numbers, distributed according to $P$ over a domain $\Omega \subset \mathbb{R}$

**Require:** Intervals $\Omega_i \in \Omega$ over which $P$ is monotonic.
**Require:** Let $x$, be a random variable distributed according to $P$.
It is the previous state of the random number generator.

1: Sample $y \in (0, P(x)]$ uniformly
2: **loop**
3: Select those intervals $\Omega_i$ such that $\max_{x \in \Omega_i} P(x) \geq y$
4: Sample $i$, weighted by the length of each $\Omega_i$
5: Sample $z \in \Omega_i$ uniformly
6: **if** $P(z) \geq y$ **then**
7: $x \leftarrow z$
8: **return** $x$
9: **else**
10: Let $\Omega_i = [a_i, b_i]$ and $m_i = (a_i + b_i)/2$
11: **if** $P(m_i) \geq y$ **then**
12: **if** $z > m_i$ **then**
13: $b_i \leftarrow z$
14: **else**
15: $a_i \leftarrow z$
16: **end if**
17: **else**
18: **if** $z > m_i$ **then**
19: $b_i \leftarrow m_i$
20: **else**
21: $a_i \leftarrow m_i$
22: **end if**
23: **end if**
24: $\Omega_i \leftarrow [a_i, b_i]$
25: **end if**
26: **end loop**

A naive implementation of the slice-sampling algorithm is still prone to bottlenecks if the distribution becomes very narrow above some $y$-value (the "slice"). Hence, a standard solution is to shrink the slice whenever a sampled value is rejected by line 9. This is accomplished by lines 10 to 24. The monotonicity of the distribution within each $\Omega_i$ ensures that they shrink, yet keep bounding the slice inside the graph of $P(u)$.

In order to ensure that the sequence of pseudo-random numbers produced by Algorithm 1 has decorrelated, a sufficiently long sequence of pseudo-random numbers needs to be generated, before the last number taken as the actual outcome of the collision. This is acomplished by Algorithm 2 (below), which is executed to sample each collision from $W$.

**Algorithm 2** Sample a velocity change, $u$, due to a collision from the transition rates $W$ given by Eq. (3.9)

**Require:** Instantaneous motor velocity, $V$, transition rates $W(V;u)$ and thermalization sample $N$

1: $P(u) \leftarrow \frac{W(V;u)}{a_0(V)}$
2: Sample $n$ uniformly from $\{N, N+1, \cdots, 2N\}$
3: Initialize Algorithm 1 with random previous pseudo-random number, the returned value is $u_0$.
4: **for** $i = 1$ **to** $n$ **do**
5: $\quad u_i$ is sampled from $P$ using Algorithm 1, with $u_{i-1}$ used as $x$ (the previous state of the Algorithm).
6: **end for**
7: **return** $u_n$

Algorithm 2 ensures that the collisions are not correlated due to correlations in the pseudo-random number generator. The correlation time had been determined for a range of $V$ and system parameters. Taking $N = 10$ showed an auto-correlation within the limits of noise. The additional randomization of the initialization length (line 2) ensures that any residual correlations do not result in systematic errors. Unless stated otherwise, the rest of this work uses[6] $N = 10$ whenever invoking Algorithm 2.

6. Determined by checking that for $N = 10$, no correlations from the pseudo-random number generator could be observed.

## 3.3 MASTER EQUATION

The dynamics of the motor is driven by collisions with the gas alone. Under the assumption of molecular chaos, this becomes a Markov process. Instead of considering individual trajectories here we examine the the probability density, $P(V,t)$, of finding a motor with velocity $V$ at time $t$. For a Markov process, the time evolution of $P(V,t)$ follows the master equation,

$$\partial_t P(V,t) = \int_{\mathbb{R}} W(V-u;u)P(V-u,t)\,\mathrm{d}u - \int_{\mathbb{R}} W(V;u)P(V,t)\,\mathrm{d}u\,, \tag{3.8}$$

where $W(V;u)\,\mathrm{d}u$ is the transition rate of a motor experiencing a collision resulting in a velocity change $V \to V+u$. Since the particle velocities are thermostated and thus collisions can be sampled from an invariant distribution, the conditional probabilities can be expressed as an integral involving three specifications:

1. Selecting only those outcomes which are commensurate with single collisions, cf. Eqs. (2.3).

2. Weighting single particle collisions by the impact frequency, where care has been taken to ensure collisions occur only with the outside surface. The impact frequency is given by $(\boldsymbol{V} - \boldsymbol{v}) \cdot \hat{\boldsymbol{n}}_i$.

3. Sampling over all possible impact speeds and the motor's sides, where $w_i(\theta_0)$ is the probability of picking the side $i$.

Hence we arrive at the expression for the transition rates:

$$W(V;u) = \sum_{i\in\{0,1,2\}} \int_{\mathbb{R}} \int_{\mathbb{R}} \underbrace{\delta\left[u - \gamma(r,\mathcal{M},\theta_i)(v_x - V - v_y \cot\theta_i)\right]}_{\text{(i)}} \underbrace{[\![(\boldsymbol{V}-\boldsymbol{v})\cdot\hat{\boldsymbol{n}}_i]\!]}_{\text{(ii)}} \underbrace{\phi(v_x,v_y)\mathrm{d}v_x\mathrm{d}v_y\, w_i(\theta_0)}_{\text{(iii)}} \tag{3.9}$$

where $\phi(v_x, v_y)$ is the velocity density function for the particles, and $r$, $\mathcal{M}$, $\gamma(r,\mathcal{M},\theta)$ and $\hat{\boldsymbol{n}}_i$ are defined in the single-collision theory in section 2.1. Consequently, the steady-state solutions of Eq. (3.8) are selected by the gas distribution, $\phi(v_x, v_y)$, the single-collision kinematics $\gamma(r,\mathcal{M},\theta)$, and the wedge angle $2\theta_0$.

## 3.4 KRAMERS–MOYAL EXPANSION

The integral-form master equation (Eq. (3.8)) can be transformed into to a non-linear infinite-order partial differential equation. This is accomplished by the Kramers–Moyal expansion.

The proof reviewed in the section only[7] demands of the function, $W(V;u)$, that its characteristic function,

$$W(V;k) := \int_{\mathbb{R}} \mathrm{e}^{\mathrm{i}uk}\, W(V;u)\,\mathrm{d}u\,, \tag{3.10}$$

exists. Before evaluating the integral, however, we expand the exponential function $\mathrm{e}^x \simeq 1 + x + x^2/2 + \ldots$ yielding

$$W(V;k) = 1 + \sum_{n=1}^{\infty} \frac{(\mathrm{i}k)^n}{n!} a_n(V)\,, \tag{3.11}$$

where $a_n(V)$ are the jump moments defined by the integral

$$a_n(V) := \int_{\mathbb{R}} u^n W(V;u)\,\mathrm{d}u\,. \tag{3.12}$$

7. Another commonly published proof is to consider the Taylor expansion of the $W(V-u;u)P(V-u)$ term around $V$. While in principle correct, this kind of proof assumes that the Taylor expansion of $W(V;u)$, in the first variable, has an infinite radius of convergence. This is not guaranteed for general transition rates.

Hence the transition rates may be written as the inverse transform of Eq. (3.11)

$$W(V;u) = \frac{1}{2\pi}\int_{\mathbb{R}} \mathrm{e}^{-\mathrm{i}uk}\left[1+\sum_{n=1}^{\infty}\frac{(\mathrm{i}k)^n}{n!}a_n(V)\right]\mathrm{d}k$$
$$= \delta(u) + \sum_{n=1}^{\infty}(-1)^n\frac{a_n(V)}{n!}\delta^{(n)}(u) \tag{3.13}$$

where $\delta^{(n)}$ is the $n$-th derivative of the Dirac delta function. The second expression in Eq. (3.13) straightforwardly follows from the identity $\delta^{(n)}(x) = (2\pi)^{-1}\int_{\mathbb{R}}(-\mathrm{i}k)^n\mathrm{e}^{-\mathrm{i}xk}\,\mathrm{d}k$ for $\forall n \in \mathbb{N}$.

The velocity probability density function evolves according to Eq. (3.8), which becomes

$$\partial_t P(V,t) = \int_{\mathbb{R}} \delta(u) + \sum_{n=1}^{\infty}(-1)^n\frac{a_n(V-u)}{n!}\delta^{(n)}(u)\,P(V-u,t)\,\mathrm{d}u$$
$$-\int_{\mathbb{R}} \delta(u) + \sum_{n=1}^{\infty}(-1)^n\frac{a_n(V)}{n!}\delta^{(n)}(u)\,P(V,t)\,\mathrm{d}u\,, \tag{3.14}$$

after inserting Eq. (3.13). The integrals in Eq. (3.14) can be evaluated using the distributional derivative of the $\delta$–function:

$$\int_{\mathbb{R}}\delta^{(n)}(x)f(x)\,\mathrm{d}x = (-1)^n\int_{\mathbb{R}}\delta(x)f^{(n)}(x)\,\mathrm{d}x = (-1)^n f^{(n)}(0) \tag{3.15}$$

where $f^{(n)}(x)$ denotes the $n$-th derivative of the function $f(x)$. An important consequence of this derivative is that $\int_{\mathbb{R}}\delta^{(n)}(x)f(-x)\,\mathrm{d}x = f^{(n)}(0)$. Furthermore, integrals of the form $\int_{\mathbb{R}}\delta^{(n)}(u)\,\mathrm{d}u = 0$. Hence, the integral over the second sum in Eq. (3.14) evaluates to zero. Integrating over the $\delta$-functions then eliminates the integrals giving

$$\partial_t P(V,t) = \sum_{n=1}^{\infty}\frac{(-1)^n}{n!}\partial_V^n\left[a_n(V)P(V,t)\right]\,, \tag{3.16}$$

which is the well known[8] Kramers–Moyal expansion [44].

8. Since truncating the Kramers–Moyal expansion at second order gives the well studied Fokker–Planck equation, the Kramers–Moyal expansion is often also called the Generalized Fokker–Planck equation.

The sum in Eq. (3.16) is semi-convergent, and solutions to the truncated form of Eq. (3.16) frequently exhibit oscillations that grow in amplitude with increasing truncation order [43]. In fact, a theorem by Pawula [44] shows that all but the second-order truncation of Eq. (3.16) exhibit solutions where $P(V,t)$ is negative in some regions. Hence Eq. (3.16) is essentially a formal series expansion, and not an asymptotic expansion.

### *3.4.1 Drift and Diffusion*

The Kramers–Moyal expansion can be thought of as the generalized form of the Fokker–Planck equation. A naive approach would then

be to identify a term analogous to the drift term in the Kramers–Moyal expansion:

$$\begin{aligned}\partial_t P(V,t) &= \sum_{n=1}^{\infty} \frac{(-1)^n}{n!} \partial_V^n \left[a_n(V) P(V,t)\right] \\ &= -\partial_V \left[\sum_{n=1}^{\infty} \frac{(-1)^{n-1}}{n!} \partial_V^{n-1} \left[a_n(V) P(V,t)\right]\right] . \end{aligned} \tag{3.17}$$

In general, a probability current, $j(V)$ can be defined as

$$\partial_t P(V,t) =: -\partial_V j(V) . \tag{3.18}$$

Probability currents can be expanded in terms of drift coefficient, $\mu(V)$, and diffusion coefficient, $\nu(V)$. These are allowed to be functions:

$$j(V) =: \underbrace{\mu(V)}_{\text{drift}} P(V) - \partial_V [\underbrace{\nu(V)}_{\text{diffusion}} P(V)] + \cdots . \tag{3.19}$$

The naming convention of drift and diffusion is justified by considering constant $\mu(V) = \mu$ and $\nu(V) = \nu$. It is then easy to see that $\partial_t \langle V \rangle = \mu$ and $\partial \langle (V-\mu)^2 \rangle = \nu$.

We see that truncating the Kramers–Moyal expansion at the second order yields $\mu(V) = a_1(V)$ and $\nu(V) = a_2(V)/2$ which is the famous Fokker–Planck equation. This makes sense, as $a_1(V)$ reflects the transferred moment, and $a_2(V)$ the transferred energy per collision.

Eq. (3.17) gives an expression for the probability current, $j(V)$:

$$j(V) := a_1(V)P(V) - \partial_V \underbrace{\left[\sum_{n=2}^{\infty} \frac{(-1)^n}{n!} \partial_V^{n-2} \left[a_n(V) P(V)\right]\right]}_{\text{(i)}} \tag{3.20}$$

$$\begin{aligned} &:= a_1(V)P(V) - \partial_V \underbrace{\left[\sum_{n=2}^{\infty} \frac{(-1)^n}{n!} \partial_V^{n-2} \left[a_n(V)\right] P(V)\right]}_{\nu(V)P(V)} \\ &\quad - \partial_V \underbrace{\left[\sum_{n=3}^{\infty} \frac{(-1)^n}{n!} \sum_{m=1}^{n} \binom{n}{m} \partial_V^{n-2-m} \left[a_n(V)\right] \partial_V^m \left[P(V)\right]\right]}_{\text{(ii)}} \end{aligned} \tag{3.21}$$

where the diffusion coefficient $\nu(V)$ is found by considering all the coefficients of $P(V)$ (*i. e.* none of the coefficients of the higher derivatives of $P(V)$) in the derivative term. This gives

$$\nu(V) = \sum_{n=2}^{\infty} \frac{(-1)^n}{n!} \partial_V^{n-2} a_n(V) \tag{3.22}$$

by invoking the product law of the derivative inside term (i) in Eq. (3.20). The drift term is found by realizing that term (ii) in Eq. (3.21) only contains $\partial_V^m [P(V)]$ terms where $m \geq 1$. Hence the coefficient of $P(V)$ in $j(V)$ is

$$\mu(v) = a_1(V) \, . \tag{3.23}$$

### 3.4.2 *Fokker–Planck Approximation*

Traditionally one arrives at the Fokker–Planck equation by taking only the first two terms of the Kramer–Moyal expansion. A practical advantage of this is that the Fokker–Planck equation, even with non-linear drift and diffusion terms, is essentially a heat equation. One therefore has the the full compliment of mathematical tools at their disposal, for finding $P(V, t)$.

Here, a slightly different approach as been taken, giving a slightly less naive approximation. Instead of truncating the Kramers–Moyal expansion, Eq. (3.16), the expression of the probability current, Eq. (3.19), is truncated at the second order derivative in $P(V)$. This is equivalent to ignoring the (ii) term in Eq. (3.21). One expects that this approximation gives improved results over truncating the Kramers–Moyal expansion at the second order, when the higher-order jump moments dominate the expansion.

Direct numerical solutions of the Fokker–Planck equation equation require numerical second derivatives. This can be avoided by introducing the secondary probability current

$$j_2(V) := \nu(V) P(V) \tag{3.24a}$$

hence

$$j_1(V) = \mu(V) P(V) - \frac{1}{2} \partial_V j_2(V) \, . \tag{3.24b}$$

Time derivatives are,

$$\partial_t j_2(V) = -\nu(V) \partial_V j_1(V) \tag{3.25a}$$

and

$$\partial_t j_1(V) = -\mu(V) \partial_V j_1(V) - \frac{1}{2} \partial_V \left[ \partial_t j_2(V) \right] \tag{3.25b}$$

which involve only the first derivatives.

### 3.4.3 *Direct Solution Scheme*

Eqs. (3.25) introduce an auxiliary variable, $j_2(V)$. This could be generalized to the Kramers–Moyal expansion in general:

$$\partial_t P_t(V) = -\partial_V j_1(V) \, , \tag{3.26a}$$

$$j_n(V) = a_n(V) P_t(V) - \frac{1}{n+1} \partial_V j_{n+1}(V) \, . \tag{3.26b}$$

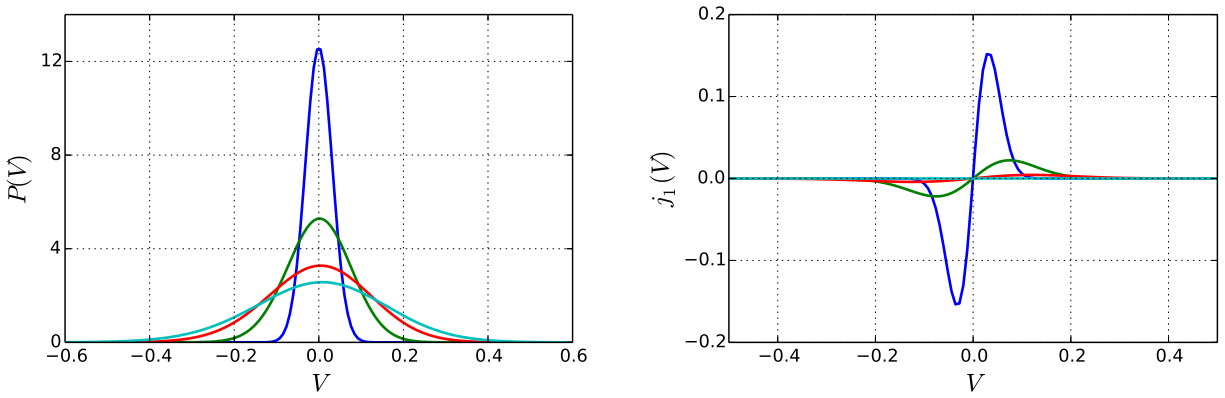


Figure 3.2: Illustration of the Fokker–Planck approximation, applied to a motor undergoing elastic, $r = 1$ collisions with gas whose velocities are sampled from a Maxwell–Boltzmann distribution. The motor to particle mass ratio is $\mathcal{M} = 100$. Different lines indicate increasing time. Cyan lines are the steady state solution. *Left Panel:* Motor velocity distribution. *Right Panel:* Probability current Eq. (3.18). The amplitude of the probability current can be used to determine whether it has reached a steady state.

This allows the $n$-th order Kramers–Moyal expansion to be solved, by solving the hierarchy of "probability currents"

$$\partial_t P_t(V) = -\partial_V j_1(V) \tag{3.27a}$$
$$\partial_t j_n(V) := -a_n(V)\partial_V j_1(V) \tag{3.27b}$$
$$\partial_t j_{n-1}(V) = -a_{n-1}(V)\partial_V j_1(V) - \frac{1}{n}\partial_V \left[\partial_t j_n(V)\right] \tag{3.27c}$$
$$\vdots$$
$$\partial_t j_1(V) = -a_1(V)\partial_V j_1(V) - \frac{1}{2}\partial_V \left[\partial_t j_2(V)\right] \tag{3.27d}$$

The trick here is to truncate the hierarchy and solve for the time derivative of the $n$-th order current first, then move onto the $(n-1)$-th order, and so on. This way, one does not require numerical approximations of the $n$-th derivative, at the expense of introducing more auxiliary variables.

## 3.5 SOLUTIONS TO THE MASTER EQUATION USING MOMENT HIERARCHIES

A natural means of truncating Eq. (3.16), while avoiding negative regions in $P(V,t)$, is to apply it to the moments[9] of $P(V,t)$, $M_k(t)$,

9. First published by [34, 35].

$$\dot{M}_k(t) = \int_{\mathbb{R}} V^k \partial_t P(V,t)\,\mathrm{d}V \ . \tag{3.28a}$$

Applying Eq. (3.16) to Eq. (3.28a) gives

$$\begin{aligned}\dot{M}_k(t) &= \int_{\mathbb{R}} V^k \sum_{n=1}^{\infty} \frac{(-1)^n}{n!} \partial_V^n \left[a_n(V)P(V,t)\right] \mathrm{d}V \\ &= \sum_{n=1}^{\infty} \frac{(-1)^n}{n!} \int_{\mathbb{R}} V^k \, \partial_V^n \left[a_n(V)P(V,t)\right] \mathrm{d}V \,. \end{aligned} \tag{3.28b}$$

This kind of integral will be encountered repeatedly in slightly different settings. The following lemma allows us to evaluate this kind of integral.

**Lemma 1** *Let $(\mathbb{R}, \Sigma, \mathrm{d}V)$ be a measure space. Let $\Omega \subset \mathbb{R}$ be an interval. Let $\partial\Omega$ be its boundary, we have*

$$\begin{aligned}&\int_{\Omega} V^k \, \partial_V^n \left[a_n(V)P(V)\right] \mathrm{d}V \qquad (*) \\ &\quad = B_{k,n}(t) + \begin{cases} \frac{(-1)^n k!}{(k-n)!} \int_{\Omega} V^{k-n} a_n(V)P(V) \, \mathrm{d}V & k \geq n \\ (-1)^k k! \; \partial_V^{n-k-1} \left[a_n(V)P(V)\right]\Big|_{\partial\Omega} & \text{otherwise} \end{cases}\end{aligned} \tag{3.29}$$

*where:*

$$B_{k,n} = \sum_{j=0}^{k-1} \frac{k!}{(k-j)!} V^{k-j} \; \partial_V^{n-j-1} \left[a_n(V)P(V)\right]\Big|_{\partial\Omega} \,. \tag{3.30}$$

Proof We simply apply integration by parts to $(*)$, where the $V^k$ term is differentiated, and the $\partial^n$ term is anti-differentiated. This can be done until either: 1) the $\partial^n$ term has been anti-differentiated away, or 2) the $V^k$ has been differentiated away. Each iteration of integration by parts gives an additional term in $B$ due to any boundaries of $\Omega$.

**Corollary 1** *For processes where $V^{m+1}\partial_V^m \left[a_n(V)P_t(V)\right]$ vanish for $V$ on $\partial\Omega$, $\forall m \leq n \in \mathbb{N}$,*

$$(*) = \begin{cases} \int_{\Omega} \frac{(-1)^n k!}{(k-n)!} V^{k-n} a_n(V)P(V) \, \mathrm{d}V & k \geq n \\ 0 & \text{otherwise} \end{cases} \tag{3.31}$$

Applying corollary 1 which together with Eq. (3.28b) and $\Omega = \mathbb{R}$ gives

$$\begin{aligned}\dot{M}_k(t) &= \sum_{n=1}^{k} \frac{k!}{n!(k-n)!} \int_{\mathbb{R}} V^{k-n} a_n(V)P(V,t) \, \mathrm{d}V \\ &= \sum_{n=1}^{k} \binom{k}{n} \left\langle V^{k-n} a_n(V) \right\rangle \,. \end{aligned} \tag{3.32}$$

This is a very elegant way of dealing with the Kramers–Moyal expansion.

Eq. (3.32) has the advantage over the master equation (Eq. (3.8)) that it is a first order finite system of partial differential equations, as opposed to being an integro-differential equation. However, it does not constitute a practical improvement over the master equation as it is not closed! In order to evaluate the right hand side of Eq. (3.32), the distribution $P(V,t)$ needs to be known.

To achieve closure, we relate the $\langle \bullet \rangle$ in Eq. (3.32) term to the moments of the distribution: The most straight forward way to do this, is to write the jump moments, $a_n(V)$, as a formal power-series[10],

$$a_n(V) = \sum_{i=0}^{\infty} d_{n,i} V^i \ . \tag{3.33}$$

10. It might seems strange, to go to some lengths to avoid relying on the Taylor expansion at the beginning of this sections, and yet to introduce a power series now. This is not pathological however, as we will show later, since *any* formal series expansion here would do.

Inserting this into Eq. (3.32) gives

$$\begin{aligned} \dot{M}_k(t) &= \sum_{n=1}^{k} \sum_{i=0}^{\infty} \binom{k}{n} d_{n,i} M_{k-n+i}(t) \\ &= \sum_{j=0}^{k-1} \sum_{i=0}^{\infty} \binom{k}{k-j} d_{k-j,i} M_{j+i}(t) \end{aligned} \tag{3.34a}$$

where the second step is the result of the change of summation variables, such that $j = k - n$. Then $j \in \{0, \ldots, k-1\}$. Furthermore, we desire to collect like $M_l$. Hence we re-index the double sum such that $l = i + j$. Then $i = l - j$ and $j \in \{0, \min[l, k-1]\}$. This reduces Eq. (3.32) to an infinite linear system,

$$\dot{M}_k(t) = \sum_{l=0}^{\infty} A_{k,l} M_l(t) \ , \tag{3.34b}$$

reminiscent of a matrix equation with matrix elements,

$$A_{k,l} := \sum_{j=0}^{\min[l,k-1]} \binom{k}{k-j} d_{k-j,l-j} \ , \tag{3.35}$$

11. Note, the indices start at 0.

which corresponds to the infinite matrix[11]:

$$A = \begin{pmatrix} 0 & 0 & 0 & 0 & \cdots \\ d_{1,0} & d_{1,1} & d_{1,2} & d_{1,3} & \cdots \\ d_{2,0} & 2d_{1,0} + d_{2,1} & 2d_{1,1} + d_{2,2} & 2d_{1,2} + d_{2,3} & \cdots \\ d_{3,0} & 3d_{2,0} + d_{3,1} & 3d_{1,0} + 3d_{2,1} + d_{3,2} & 3d_{1,1} + 3d_{2,2} + d_{3,3} & \cdots \\ d_{4,0} & 4d_{3,0} + d_{4,1} & 6d_{2,0} + 4d_{3,1} + d_{4,2} & 4d_{1,0} + 6d_{2,1} + 4d_{3,2} + d_{4,3} & \cdots \\ \vdots & \vdots & \vdots & \vdots & \ddots \end{pmatrix} \tag{3.36}$$

Hence we have reduced the Kramers–Moyal expansion to an infinite-order linear system of ordinary differential equations for the

moments of the distribution. Since we see a clear interdependence of the time evolution of the different moments, and since moments the moments of a distribution are not independent from one another, this is appropriately called a moment *hierarchy*.

While the moment hierarchy approach has been first reported in [35], the matrix formalism presented here is a new generalization of the moment hierarchy technique. All the details of the physical processes are represented by the expansion coefficients $d_{n,i}$, and the matrix $A$, Eq. (3.36), is universal.

### *3.5.1 Truncation of the Infinite Moment Hierarchy*

Eq. (3.35) shows that the infinite system of linear ordinary differential equations represented in Eq. (3.34b) is strongly coupled. In order to numerically solve Eq. (3.34b) we require a means to truncate the matrix $A$ at some finite size, without introducing artefacts from the truncation of the system.

Let us consider, that Eq. (3.33) is truncated at some finite order. In this way, we essentially model arbitrarily closely the physical system by another one, where the finite order expansion of Eq. (3.33) is exact. Unfortunately, this does not guarantee that the system of equations becomes closed. For instance, if we truncate Eq. (3.33) at order 2, then Eq. (3.35) becomes

$$A_2 = \begin{pmatrix} 0 & 0 & 0 & 0 & \cdots \\ d_{1,0} & d_{1,1} & d_{1,2} & 0 & \cdots \\ d_{2,0} & 2d_{1,0}+d_{2,1} & 2d_{1,1}+d_{2,2} & 2d_{1,2} & \cdots \\ d_{3,0} & 3d_{2,0}+d_{3,1} & 3d_{1,0}+3d_{2,1}+d_{3,2} & 3d_{1,1}+3d_{2,2} & \cdots \\ \vdots & \vdots & \vdots & \vdots & \ddots \end{pmatrix}$$

As we can see, the time evolution of the first moment (second line) only depends on the first and second moment, and no longer on any higher moments. Likewise the time evolution of the second moment (third line) depends on the first, second, and third moment. Hence, truncating at order $N$, while constituting an improvement over simply truncating Eq. (3.36), does not lead to formal closure as the $N$-th moment's time evolution still depends on th $(N+1)$-st moment. In fact, it is coupled by the constant $Nd_{1,N}$. Therefore, in order to achieve closure in the limit as $N$ approaches a large number, this truncation scheme requires that $d_{1,N}$ approaches zero faster than $1/N$.

Furthermore, this kind of truncation scheme will most likely lead to modified physics. If we look at the definition of the first two jump moments, then

$$a_1(V) := \int_{\mathbb{R}} u\, W(V;u)\mathrm{d}u = \langle \rho \rangle(V) \tag{3.37a}$$

$$a_2(V) := \int_{\mathbb{R}} u^2\, W(V;u)\mathrm{d}u = \langle E \rangle(V) \tag{3.37b}$$

where $\langle\rho\rangle(V)$ and $\langle E\rangle(V)$ is the average momentum and energy of a collision, respectively, given an instantaneous motor velocity $V$. Clearly $\langle\rho\rangle$ is a signed quantity, therefore it should be expanded to an odd power, yet $\langle E\rangle$ is always positive, and therefore should be expanded to an even power. This makes the case for truncating Eq. (3.33) at an appropriate order depending on $n$, and not at some fixed order. For instance, if we truncate the power series of $a_n$ at $n^{12}$ we find that Eq. (3.36) becomes

$$A_1 = \begin{pmatrix} 0 & 0 & 0 & 0 & \cdots \\ d_{1,0} & d_{1,1} & 0 & 0 & \cdots \\ d_{2,0} & 2d_{1,0}+d_{2,1} & 2d_{1,1}+d_{2,2} & 0 & \cdots \\ d_{3,0} & 3d_{2,0}+d_{3,1} & 3d_{1,0}+3d_{2,1}+d_{3,2} & 3d_{1,1}+3d_{2,2}+d_{3,3} & \cdots \\ \vdots & \vdots & \vdots & \vdots & \ddots \end{pmatrix}$$

which represents a fully decoupled system. Of course, the decoupling disappears once again when we wish to more closely model the jump moments. We shall discuss the details of truncation in the next sections, whenever numerical solutions to Eq. (3.34b) are found.

12. This being the lowest order at which to truncate $a_n$, while still remaining commensurate with Eqs. (3.37).

## 3.6 EXPANSION OF THE JUMP MOMENTS FOR FACTORIZABLE VELOCITY DISTRIBUTIONS

For many distributions, it is possible to write a probability distribution, $\phi(x)$ in terms of

$$\phi(x) = p(x)\omega(x)\ , \tag{3.38}$$

where $p(x)$ is an infinite-order polynomial [6] in $x$, and $\omega(x)$ is a "weight function". Usual choices for $\omega(x)$ are Gaussian, or exponential functions. The details of this expansion can be found in the appendix, section A. The polynomial, $p(x)$, can be written as

$$p(x) = \sum_{k=0}^{\infty} b_k^{(\omega)} x^k\ . \tag{3.39}$$

Different probability density functions can thus be characterized by the sequence $\left\{b_k^{(\omega)}\right\}_{k=0}^{\infty}$.

Here this representation is used to generalize the problem of finding a series expansion for $a_n(V)$, Eq. (3.33), given a factorizable distribution of particle velocities, $\phi(v_x, v_y) = \phi_x(v_x)\phi_y(v_y)$. Hence, in Eq. (3.9) we factorize the $\phi(v_x, v_y)$ term and subsequently expand each $\phi_\bullet$. This gives

$$W(V;u) = \sum_{k_1=0}^{\infty}\sum_{k_2=0}^{\infty} b_{k_1}^{(\omega_x)} b_{k_2}^{(\omega_y)} \hat{W}_{k_1,k_2}(V;u)\,, \tag{3.40a}$$

where

$$\hat{W}_{k_1,k_2}(V;u) := \sum_{i\in\{0,1,2\}} \int_{\mathbb{R}}\int_{\mathbb{R}} \delta\left[u-\gamma(r,\mathcal{M},\theta_i)(v_x-V-v_y\cot\theta_i)\right] \\ \left[\!\left[(\boldsymbol{V}-\boldsymbol{v})\cdot\hat{\boldsymbol{n}}_i\right]\!\right] v_x^{k_1}v_y^{k_2}\omega_x(v_x)\omega_y(v_y)\mathrm{d}v_x\mathrm{d}v_y\, w_i(\theta_0)\ . \tag{3.40b}$$

Here, the $x$ and $y$ components of $\phi$ have been expanded in terms of potentially different weight functions. Hence, the jump moments become

$$a_m(V) := \sum_{k_1=0}^{\infty}\sum_{k_2=0}^{\infty} b_{k_1}^{(\omega_x)} b_{k_2}^{(\omega_y)} \hat{a}_{k_1,k_2,m}(V) \tag{3.40c}$$

where

$$\hat{a}_{k_1,k_2,m}(V) := \int_{\mathbb{R}} u^n \hat{W}_{k_1,k_2}(V;u)\,\mathrm{d}u\,. \tag{3.40d}$$

Using this expansion, we can find a method for determining the expansion coefficients. The Taylor expansion coefficients are given by $d_{m,n} = a_m^{(n)}(0)/n!$, hence the expansion coefficients are

$$d_{m,n} := \frac{\partial_V^n a_m(0)}{n!} = \sum_{k_1=0}^{\infty}\sum_{k_2=0}^{\infty} \frac{b_{k_1}^{(\omega_x)} b_{k_2}^{(\omega_y)}}{n!} \partial_V^n \hat{a}_{k_1,k_2,m}(0)\ . \tag{3.41}$$

Reducing the problem of computing the expansion coefficients, $d_{m,n}$, to computing the derivatives $\partial_V^n \tilde{a}_{k_1,k_2,m}(0)$. These are subject to the useful recursion relation

$$\partial_V \hat{a}_{k_1,k_2,m}(V) = k_1 \hat{a}_{k_1-1,k_2,m}(V) - \frac{1}{\sigma_x}\hat{a}_{k_1+1,k_2,m}(V)\ , \tag{3.42}$$

if $\omega_x(x) \sim \exp\left[-x^2/2\sigma_x\right]$. Alternatively

$$\partial_V \hat{a}_{k_1,k_2,m}(V) = k_1 \hat{a}_{k_1-1,k_2,m}(V) - \frac{1}{\sigma_x}\hat{a}_{k_1,k_2,m}(V)\ , \tag{3.43}$$

if $\omega_x(x) \sim \exp\left[-|x|/\sigma_x\right]$.

## 3.7 SUMMARY

Here we have reviewed the basic details for the kinetic theory of the Brownian motor model introduced in chapter 2. The assumption of molecular chaos allows us to model the dynamics of the motor as a Markov process, introduced in section 3.1. At discrete times, distributed according to Eq. (3.7), a gas particle collides with the motor. This results in a velocity change $V \to V+u$, whose transition rate is given by Eq. (3.9).

In section 3.2, we have reviewed the slice-sampling algorithm, which allows for the efficient sampling of the velocity changes according to the transition rates given in Eq. (3.9).

This is followed by a review of the Kramers–Moyal expansion in section 3.4. Here the Kramers–Moyal expansion is derived, and used to solve the master equation, governing the time evolution of the motor's velocity distribution. The Fokker–Planck expansion is briefly discussed as a special case of the Kramers–Moyal expansion. The method of moment hierarchies is introduced as a means of solving the Kramers–Moyal expansion. Here a previously unpublished generalization of the moment-hierarchy method is presented.

Finally, we explore a general method of expanding the jump moments provided the velocity distribution of the gas particles can be factorized. In other words, if the components of the particle velocities are statistically independent, the expansion of the jump moments is given by the recursion relations in Eqs. (3.42) and (3.43).

## 3.8 OUTLOOK

In this chapter, we have reviewed the basic tools that shall be employed in the following chapters. We will examine two separate models, each requiring a different tool reviewed in this chapter.

In chapter 4, the gas particle velocity distribution is a squeezed Gaussian. We find that there exists an analytical expansion for the jump moments, and so the moment-hierarchy method will prove to be very useful there.

When considering a gas where all particles have the same speed, as is the case in chapter 5, the jump moments are no longer analytical. Hence, we have to resort to the method tracking motor trajectories numerically (cf. section 3.2).

# Rectification due to Anisotropy: Granular Brownian Motors

4

## 4.1 Introduction

When a non-cohesive granular gas is driven by shaking, [53] have shown that the typical velocity distribution of the gas particles can be faithfully approximated by a squeezed Gaussian.

Even though granular Brownian motors have been realized experimentally [18, 22, 28], an analysis of the effect of gas anisotropy was lacking in the literature. In this chapter, we report on the motion of the motor in a gas with an anisotropic velocity distribution. The effect of the anisotropy is compared to the effect of dissipation. This chapter is largely based on, and expands upon the details, our article recently published in Physics Review E (Rapid Communications) [5]. A copy of this paper may be found in the appendix, section B.1

## 4.2 Model

An outline of the model for the motor, and the motor–gas interaction, is given in section 2.1. What remained to be specified at the end of the previous chapter is the velocity distribution for the gas particles.

### *4.2.1 Gas Velocity Distribution*

Following [53], we model an anisotropic velocity distribution using a squeezed Gaussian,

$$\phi(\hat{v}_x, \hat{v}_y) = \frac{m}{2\pi k\sqrt{T_x T_y}} \exp\left[-\frac{m}{2}\left(\frac{\hat{v}_x^2}{kT_x} + \frac{\hat{v}_y^2}{kT_y}\right)\right], \tag{4.1}$$

where $m$ is the particle mass, $k$ is Boltzmann's constant, $T := \left\langle m(\hat{v}_x^2 + \hat{v}_y^2)\right\rangle_\phi /(2k) =: (T_x + T_y)/2$ is the gas temperature averaged over both degrees of freedom, and $T_x$ and $T_y$ are the granular temperatures in the $\hat{x}$ and $\hat{y}$ direction, respectively. Anisotropy is

quantified via the squeezing parameter, $\alpha^2 := T_y/T_x$. Without loss of generality, let $\alpha \geq 1$.

### 4.2.2 *Shaking*

We require independent control of the the gas temperature and its anisotropy[1]. To avoid artefacts due to an increased granular temperature of the gas $\alpha$ is changed under the constraint

$$\text{constant} \equiv T = \frac{T_x + T_y}{2} \,. \tag{4.2}$$

Setting the constant to 1 we arrive at and expression for $T_x$ and $T_y$ given $\alpha$:

$$T_x = \frac{2}{\alpha^2 + 1} \qquad\qquad T_y = \frac{2}{\alpha^{-2} + 1} \,. \tag{4.3}$$

1. In the laboratory, only the shaking strength can be varied freely. This would increase both, the granular temperature, and anisotropy.

### 4.2.3 *Dimensionless Units*

Introducing dimensionless velocities, $v := \hat{v}/\sqrt{kT/m}$, reduces the velocity distribution to,

$$\phi_\alpha(v_x, v_y) = \frac{1}{4\pi}\frac{\alpha^2+1}{\alpha} \exp\left[-\frac{1}{2}\left(\frac{\alpha^2+1}{2}v_x^2 + \frac{\alpha^{-2}+1}{2}v_y^2\right)\right], \tag{4.4}$$

which depends on $\alpha$ only. The parameters $m$, $k$, $T_x$ and $T_y$ have been absorbed into the dimensionless velocities. Normalization of Eq. (4.4) *i. e.* $\phi(\hat{v}_x, \hat{v}_y)\,\mathrm{d}\hat{v}_x\mathrm{d}\hat{v}_y = \phi_\alpha(v_x, v_y)\,\mathrm{d}v_x\mathrm{d}v_y$ is still fulfilled.

Time is non-dimensionalized using the gas density (which is related to the collision frequency at rest). The gas density cannot be freely chosen. We model collisions as independent. Hence the gas density needs to remain low enough, to avoid feedback from the motor's motion on the gas causing local density correlations. [12] discuss the upper bound on the collision rate, to ensure that local density correlations, due to a collision, dissipate before the next collision.

## 4.3 TRANSITION RATES

Given Eq. (4.4), the transition rates, $\hat{W}_{0,0}(V; u)$, and jump moments, $\hat{a}_{0,0,m}$, are given by Eqs. (3.40) for

$$\omega_x(v_x) = \sqrt{\frac{1+\alpha^2}{4\pi}} \exp\left[-\frac{1+\alpha^2}{4}v_x^2\right] \tag{4.5a}$$

$$\omega_y(v_y) = \sqrt{\frac{1+\alpha^{-2}}{4\pi}} \exp\left[-\frac{1+\alpha^{-2}}{4}v_y^2\right] \tag{4.5b}$$

Evaluating the $v_x$ integral in $\hat{W}_{0,0}(V;u)$ gives[2]

$$\hat{W}_{0,0}(V;u) = \sum_{i\in\{0,1,2\}} w_i(\theta_0) \frac{[\![-u\sin\theta_i]\!]}{\gamma^2(r,\mathcal{M},\theta_i)} \int_{\mathbb{R}} \phi\left(\frac{u}{\gamma(r,\mathcal{M},\theta_i)} + V + v_y\cot\theta_i, v_y\right) \mathrm{d}v_y \ , \tag{4.6}$$

2. the additional factor of $1/\gamma$ is due to evaluating an integral over a $\delta$-function, where the argument is multiplied by $\gamma$

where $\gamma(r,\mathcal{M},\theta)$ is given by Eq. (2.3b). The remaining integral can be evaluated by substituting Eqs. (4.5) for $\phi(v_x,v_y) = \omega_x(v_x)\omega_y(v_y)$ giving

$$\int_{\mathbb{R}} \phi\left(\frac{u}{\gamma(r,\mathcal{M},\theta_i)} + V + v_y\cot\theta_i, v_y\right) \mathrm{d}v_y = \sqrt{\frac{1+\alpha^2}{4\pi\left(1+\alpha^2\cot^2\theta_i\right)}} \exp\left[-\frac{1+\alpha^2}{4+4\alpha^2\cot^2\theta_i}\left(V + \frac{u}{\gamma(r,\mathcal{M},\theta_i)}\right)^2\right] \tag{4.7}$$

After evaluating the sum, we find that the transition rates have the following analytical form which can be decomposed into transitions going forward ($u>0$) and backward ($u<0$)

$$\hat{W}_{0,0}(V;u) = \hat{W}^{+}_{0,0}(V;u)[\![u>0]\!] + \hat{W}^{-}_{0,0}(V;u)[\![u<0]\!] \tag{4.8a}$$

with the forward ($+$), and backward ($-$) transition rates being

$$\hat{W}^{\pm}_{0,0}(V;u) = \pm\frac{1}{2\sqrt{\pi}} \frac{\sqrt{4\beta_\pm}}{1+\operatorname{cosec}\theta_0} \lambda_\pm^2 u\, \mathrm{e}^{-\beta_\pm(\lambda_\pm u+V)^2} \tag{4.8b}$$

where the following quantities have been defined for brevity:

$$\lambda^+ := \frac{1+\mathcal{M}}{1+r} \qquad \beta^+ := \frac{1}{4}\left(1+\alpha^2\right) \tag{4.8c}$$

$$\lambda^- := \frac{1+\mathcal{M}\,\cos^{-2}\,\theta_0}{1+r} \qquad \beta^- := \frac{1}{4}\,\frac{1+\alpha}{1+\alpha^2\cot\theta_0} \tag{4.8d}$$

## 4.4 JUMP MOMENTS

The jump moments can be computed using Eqs. (4.8) directly.

$$a_m(V) = a_m^+(V) + a_m^-(V) \ , \tag{4.9}$$

where

$$a_m^\pm(V) := \int_{\mathbb{R}^\pm} u^n \hat{W}^\pm_{0,0}(V;u)\,\mathrm{d}u \ . \tag{4.10}$$

### 4.4.1 *Expansion of the Jump Moments*

One can use the Taylor-series expansion coefficients, Eq. (3.41), together with the recursion relation, Eq. (3.42), to calculate the power series expansion. This requires least effort, but numerical evaluation has shown that this power series has a small radius of convergence of small motor to gas particle mass ratio, $\mathcal{M}$. As a consequence it can lead to divergent solutions to the moment hierarchy. Instead of taking this direct approach we present here a series expansion with infinite radius of convergence.

All exponential terms in Eq. (4.8a) have the same basic structure. So one alternative strategy of finding a power-series expansion for Eq. (4.9) is to use the power-series expansion for the exponential function. The exponential term is expanded so that we obtain polynomials in $V$:

$$
\begin{aligned}
I(u,\beta,\lambda) &:= \mathrm{e}^{-\beta(\lambda u+V)^2} && \text{(4.11a)}\\
&= \mathrm{e}^{-\beta\lambda^2u^2-\beta\left(2\lambda uV+V^2\right)} \\
&= \mathrm{e}^{-\beta\lambda^2u^2}\sum_{n=0}^{\infty}\frac{\left(-\beta\left(2\lambda uV+V^2\right)\right)^n}{n!} && \text{(4.11b)}\\
&= \mathrm{e}^{-\beta\lambda^2u^2}\sum_{n=0}^{\infty}\frac{(-\beta)^n}{n!}\sum_{m=0}^{n}\binom{n}{m}(2\lambda u)^{n-m}V^{n+m} && \text{(4.11c)}\\
&= \mathrm{e}^{-\beta\lambda^2u^2}\left[\sum_{\substack{m=0\\ m\text{ even}}}^{\infty}c_n^{(\mathrm{e})}(\beta,\lambda,u)V^m+\sum_{\substack{m=0\\ m\text{ odd}}}^{\infty}c_n^{(\mathrm{o})}(\beta,\lambda,u)V^m\right]. && \text{(4.11d)}
\end{aligned}
$$

Here the first step, Eq. (4.11b), is simply the expansion of the exponential function for all terms involving $V$. The second step, Eq. (4.11c), applies the binomial theorem. The final step, Eq. (4.11d), is the result of grouping like powers in $V$. Resulting in the following coefficients for even and odd powers

$$
\begin{aligned}
c_m^{(\mathrm{e})}(\beta,\lambda,u) &:= \sum_{s=0}^{m/2}\frac{(-\beta)^{\frac{m}{2}+s}}{\left(\frac{m}{2}+s\right)!}\binom{\frac{m}{2}+s}{\frac{m}{2}-s}(2\lambda u)^{2s} && \text{(4.12a)}\\
c_m^{(\mathrm{o})}(\beta,\lambda,u) &:= \sum_{s=0}^{(m-1)/2}\frac{(-\beta)^{\frac{m-1}{2}+1+s}}{\left(\frac{m-1}{2}+1+s\right)!}\binom{\frac{m-1}{2}+1+s}{\frac{m-1}{2}-s}(2\lambda u)^{2s+1} && \text{(4.12b)}
\end{aligned}
$$

The procedure of expanding the exponential terms of Eq. (4.8a) relies only on the power series expansion of the exponential function. Hence, its radius of convergence is infinite.

The expansion coefficients of the jump moments, Eq. (4.9), are obtained from the coefficients, Eqs. (4.12), of the exponential

integrand expansion by integrating over $u$. That is

$$a_n = \frac{\sqrt{2}-1}{2\sqrt{\pi}}\lambda_+^2\sqrt{1+\alpha^2}\int_{\mathbb{R}^+} u^{n+1} I\left(u,\beta_+,\lambda_+\right)\,\mathrm{d}u + \frac{\sqrt{2}-2}{2\sqrt{2\pi}}\lambda_-^2\int_{\mathbb{R}^-} u^{n+1} I\left(u,\beta_-,\lambda_-\right)\,\mathrm{d}u \tag{4.13a}$$

$$= \sum_{\substack{m=0\\ m\text{ even}}}^{\infty} d_{n,m}^{(\mathrm{e})} V^m + \sum_{\substack{m=0\\ m\text{ odd}}}^{\infty} d_{n,m}^{(\mathrm{o})} V^m \tag{4.13b}$$

where the expansion coefficients are:

$$d_{n,m}^{\bullet} = \frac{\sqrt{2}-1}{2\sqrt{\pi}}\lambda_+^2\sqrt{1+\alpha^2}\int_{\mathbb{R}^+} u^{n+1}\,\mathrm{e}^{-\beta_+\lambda_+^2u^2} c_m^{\bullet}\left(\beta_+,\lambda_+,u\right)\,\mathrm{d}u + \frac{\sqrt{2}-2}{2\sqrt{2\pi}}\lambda_-^2\int_{\mathbb{R}^-} u^{n+1}\,\mathrm{e}^{-\beta_-\lambda_-^2u^2} c_m^{\bullet}\left(\beta_-,\lambda_-,u\right)\,\mathrm{d}u \tag{4.14}$$

where the $\bullet$ refers to the even, (e), or odd, (o), coefficient. The integrals in Eq. (4.14) are all of the form:

$$\Lambda_n^{\pm}(\lambda) := \int_{\mathbb{R}^{\pm}} u^n\,\mathrm{e}^{-\lambda u^2}\,\mathrm{d}u = \frac{(\pm 1)^n}{2}\lambda^{-\frac{1+n}{2}}\Gamma\left[\frac{1+n}{2}\right] \tag{4.15}$$

so that Eq. (4.14) can be evaluated explicitly using Eqs. (4.12) and substituting $u^s \to \Lambda_s^{\pm}(\beta_{\pm}\lambda_{\pm}^2)$ depending on the integral domain, $\pm$. Eq. (4.15) also shows an important scaling with respect to motor mass. We see the scaling $\Lambda_n^{\pm} \simeq \lambda_{\pm}^{-(1+n)/2}$ with respect to $\lambda$. Furthermore, $\lambda_{\pm} \simeq \mathcal{M}$ for large $\mathcal{M}$ irrespective or integral domain. Hence $d_{n,m}^{\bullet}$ vanishes for large $n$ in the limit $\mathcal{M} \to \infty$. Fig. 4.1 confirms this observation.

Numerical values for a variety of parameters are shown in Fig. 4.1. Here for decreasing $\mathcal{M}$, the values of $d_{m,n}$ diverge for increasing $m$. This is pathological to the truncated Kramers–Moyal expansion. The Kramers–Moyal expansion formally holds for all stochastic processes where the jump moments exist: however, for our model any motors $\mathcal{M} \lesssim 4$ cannot be solved with the truncated moment hierarchy.

## 4.5 TIME-RESOLVED VELOCITY DISTRIBUTION

To get a first look at the effect of the different model parameters we solve the Kramers-Moyal expansion for the time evolution of the velocity distribution (as defined by the transition rates in Eqs. (4.8)). First we use the Fokker-Planck approximation to give an approximation to velocity distribution $P(V,t)$. Then we use the moment-hierarchy approach to determine the moments of the velocity distribution. At that point we establish for which parameters the Fokker-Planck equation is an appropriate approximation.

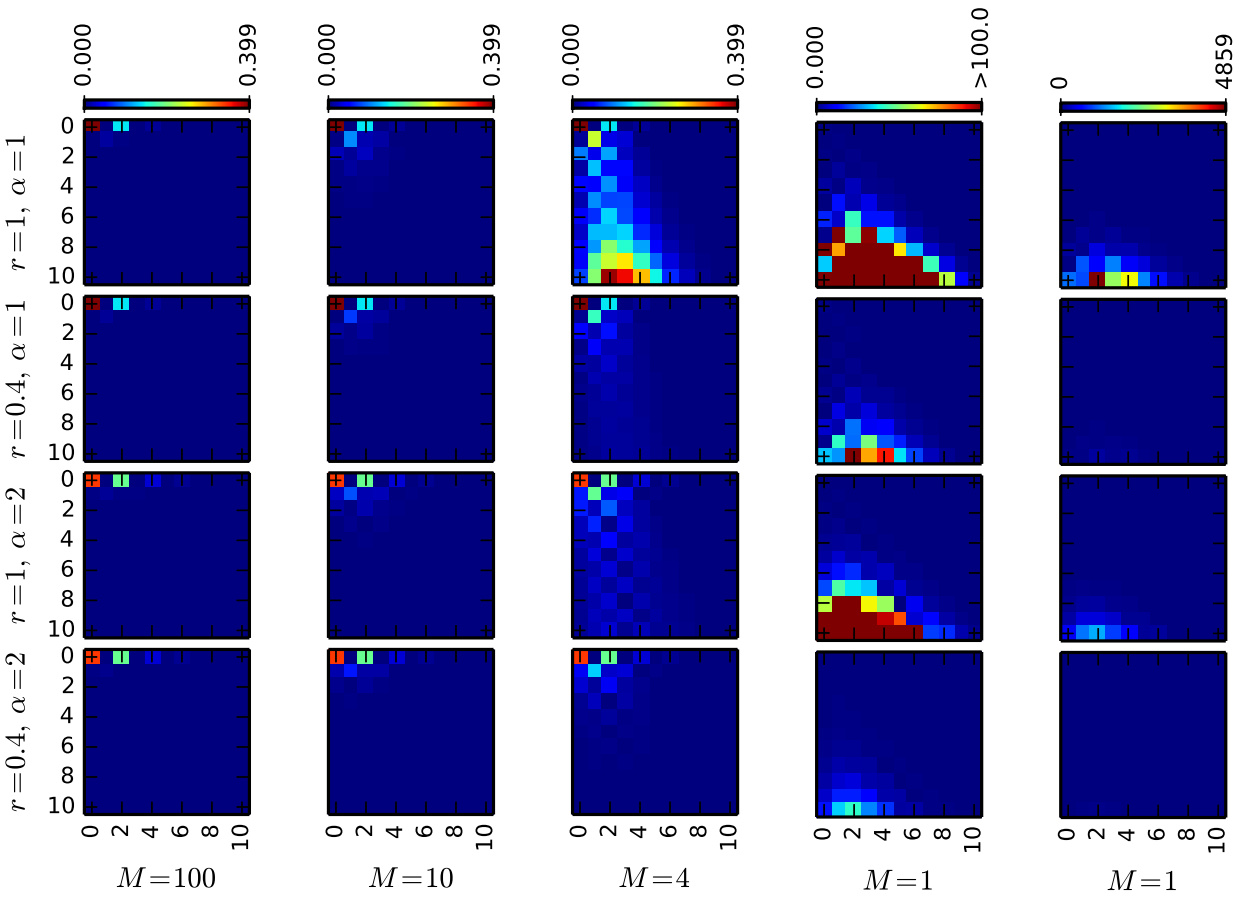


Figure 4.1: Graphical representation of the $|d_{m,n}|$ matrices. The colour bar for each column is shown on top. Note that the fourth column (corresponding to $M = 1$) has an open-end color bar. Here certain a very small number of values exceed $|d_{m,n}| > 4850$. An unabridged representation of this column is shown in the last column.

### *4.5.1 Fokker-Planck Approximation*

The decreasing dependence on the jump moments of higher order than two (as seen by the decreasing amplitude of $d_{n,m}$ with $\mathcal{M}$ in Fig. 4.1), shows that for increasing $\mathcal{M}$ the Fokker–Planck equation becomes an increasingly good approximation. Hence, Eqs. (3.25) are solved numerically for the initial condition $P_0(V) = \exp[-V^2/2\delta]/\sqrt{2\pi\delta}$ for $\delta = 1/10\mathcal{M}$.

Fig. 4.2 shows solutions to the Fokker–Planck equation. The effect of changing $\alpha$ and $r$ are compared. The top panel illustrates how a change in $\alpha$ of $10^{-2}$ causes a significant drift[3]. A change in $r$ or 0.7 does not produce such a large effect on the drift, yet it significantly decreases with width of the velocity distribution. We conclude that, for massive motors, anisotropy predominately affects motor drift, while dissipation predominantly affect width of the velocity distribution (the "motor temperature").

3. Here we see the effect of the drift in the distribution because the mean is moved slightly into the negative direction.

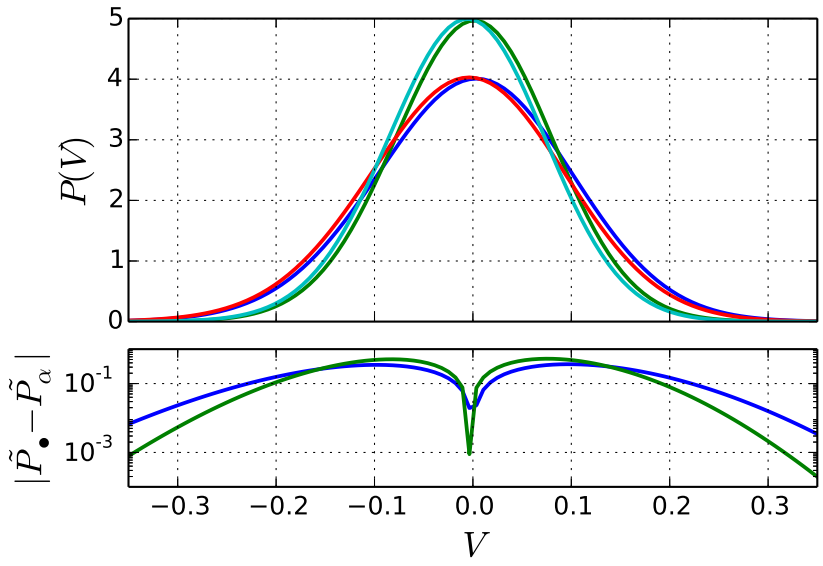


Figure 4.2: Steady-state solutions to the Fokker–Planck equation for $\mathcal{M} = 100$, showing the effect of changing $\alpha$ and the effect of changing $r$. *blue line:* $r = 1 \quad \alpha = 1$; *red line:* $r = 1 \quad \alpha = 1.02$; *green line:* $r = 0.3 \quad \alpha = 1$; *cyan line:* $r = 0.3 \quad \alpha = 1.02$. The bottom pannel shows the difference between the respective curves. The *blue line* shows the difference between the red and blue lines in the top panel. The *green line* shows the difference between the green and cyan lines in the top panel.

### *4.5.2 Moment Hierarchy*

In order to solve the Kramers–Moyal expansion numerically, Eq. (3.36) is truncated at the $N$-th order leading to the system of linear equations

$$\dot{M}_k(t) = \sum_{l=0}^{N} A_{k,l} M_l(t) \ . \tag{4.16}$$

Inserting the expansion coefficients, $d_{n,i}$, computed in Eq. (4.14), into $A$ (given explicitly by Eq. (3.36)) provides an analytical, albeit tedious, expression for Eq. (4.16). In the remainder of this chapter, we will discuss these solutions. To illustrate the parameter-dependence of $A$, the magnitude of its elements is shown in Fig. 4.3. When the diagonal dominates $A$ accurate solutions are obtained by truncating at $N = 20$. However, for $\mathcal{M} \lesssim 4$, $a_{n,m}$ diverges with increasing $n$, and so that the result is strongly dependent on the truncation order $N$. Hence, we must restrict our analysis to $\mathcal{M} > 4$.

Asymptotic analysis of Eq. (4.14) reveals that $d_{n,i} \sim -i^{-i/2}$ for large $i$. For $\mathcal{M} > 4$ this results in a combined truncation error in Eq. (4.16) of the order of $10^{-10}$ for $N = 20$. As such, we will solve Eq. (4.16) for $N = 20$ and a wedge angle $\theta_0 = \pi/4$ unless stated otherwise. The initial condition will always be an ensemble where all the motors are initially at rest: $\boldsymbol{M}(0) = (1, 0, 0, \cdots)$.

Fig. 4.4 shows typical time dependencies of the motor drift, $\langle V \rangle$, and motor temperature ,$\mathcal{T}$, (cf. Eq. (4.22)) for $\mathcal{M} = 10$, and 40. We see that the time evolution for the following physical settings:

**Elastic collisions** For elastic collisions and an isotropic gas, the ensemble undergoes a finite transient drift while it heats up to the temperature of the gas [50]. Subsequently, the drift ceases

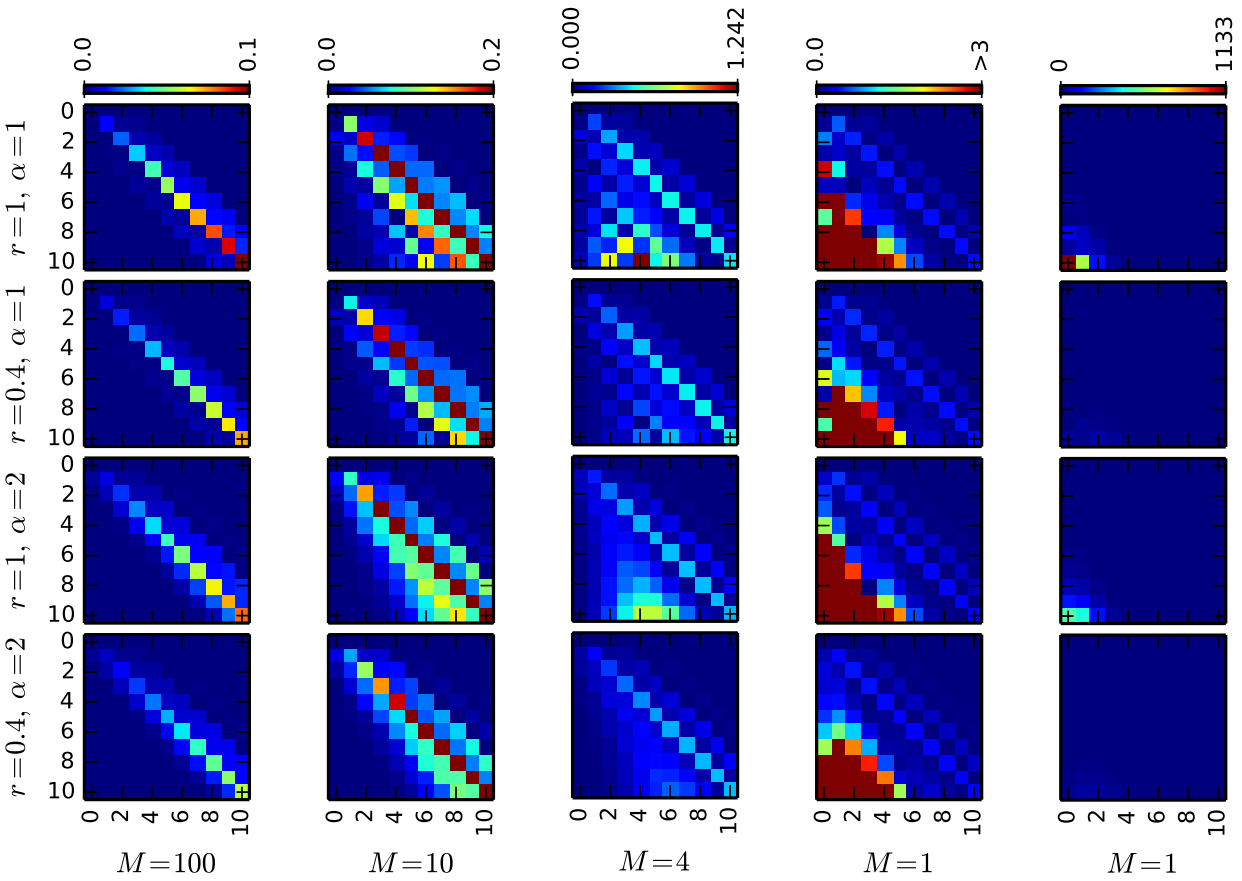


Figure 4.3: Graphical representation of the $|a_{m,n}|$ matrices. The colour bar for each column is shown on top. Note that the fourth column (corresponding to $M = 1$) has an open-end color bar. Here certain a very small number of values exceed $|a_{m,n}| > 1130$. An unabridged representation of this column is shown in the last column.

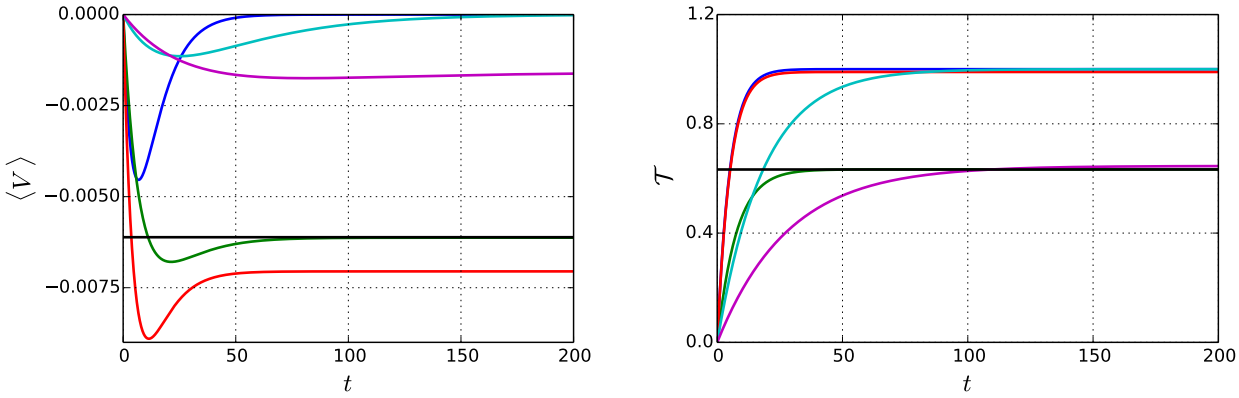


Figure 4.4: Motor drift, $\langle V \rangle$ (left panel) , and temperature, $\mathcal{T}$ (right panel), against $t$ for motors with mass ratio $\mathcal{M} = 10$, and 40, and $\theta_0 = \pi/4$. *Blue and cyan lines:* $r = 1$ and $\alpha = 1$, elastic collisions with an isotropic gas. *Green and magenta lines:* $r = 0.3$ and $\alpha = 1$, strongly inelastic collisions with an isotropic gas. The motor relaxes to the values predicted by [8] (black horizontal lines). *Red lines:* $r = 1.0$ and $\alpha = 1.02$, elastic collisions with a slightly anisotropic gas. The magenta and cyan lines represent motors with $\mathcal{M} = 40$. We see that increasing mass increases the time it takes for the motor to reach the steady-state, as we might expect for a constant input of power.

(see Fig. 4.4, *blue* and *cyan* lines). This is what we expect when the motor is in equilibrium with the gas.

**Dissipative collisions** When introducing inelastic gas-motor collisions, the steady-state acquires a finite drift velocity and a temperature significantly lower than the gas (see Fig. 4.4, *green* and *magenta* lines, and also Fig. 4.5). For comparison, the published [8] result for an isotropic gas with $\mathcal{M} = 10$ and $r = 0.3$ is represented by the black horizontal lines.

**Anisotropic gas** A small amount of squeezing, $\alpha = 1.02$, causes a drift similar to the drift in a system with strongly inelastic collisions (see Fig. 4.4, *red* lines). This squeezing hardly affects the temperature.

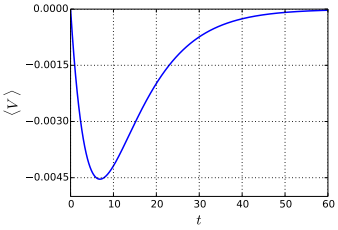


Figure 4.5: Closeup of the time evolution of $M_1(t)$ for $\mathcal{M} = 10$, $r = 1$, and $\alpha = 1$. We see that initially there is some motor drift which ceases as the motor equilibrates with the gas.

Additionally (here examining the magenta and cyan lines), increasing the motor mass results in an increased thermalization time (the time it takes for the motor to reach the same temperature as the gas). When this happens, the motor drift has reached a steady state. This is is quite reasonable as the collision rate between motor and gas particles does not change with motor mass. Hence, the gas' power input into the motor's motion is unchanged by changing motor mass.

Having examined drift and temperature, we now examine the *shape* of the motor velocity distribution, $P(V)$. This information can be characterized by the higher order moments and cumulants of the distribution. In particular, we are interested in how asymmetric the distribution is about its mean, and how important its tails are. Asymmetry, or *skewness*, about a mean is measured using the third cumulant, $\kappa_3$. And "fatness", or *excess kurtosis* is measured using the fourth cumulant, $\kappa_4$. In order to avoid the variance affecting the skewness, it is defined as $\kappa_3/\kappa_2^{3/2}$. Likewise, $\kappa_4/\kappa_2^2$ defines the excess kurtosis[4].

Fig. 4.6 shows the time evolution of the skewness and the excess kurtosis of the velocity distribution. Initially the velocity distribution is highly non-Gaussian. The skewness tells us that the distribution is highly positively skewed. Likewise, there is a high positive excess kurtosis, indicating that $P(V)$ is broader than a Gaussian. The skewness is likely due to the asymmetric shape of the motor. As the motor equilibrates with the gas it develops a negative skewness in those cases where the motor has non-zero drift: if collisions are inelastic or anisotropic. This is reasonable, after all, the ensemble develops a drift in the negative direction. If collisions are elastic and the gas is isotropic then a slight positive skewness is retained. The heavier motors retain less skewness and excess kurtosis, indicating that for increasing mass, the steady-state velocity distribution is more like a Gaussian than for light motors. For inelastic or anisotropic systems, the motor retains a positive

4. If generalized to all $n$ cumulants, the only distribution yielding 0 for all $n > 2$ is the Gaussian distribution. Hence $\kappa_3$ and $\kappa_4$ characterize the *non-Gaussianity* of the distribution

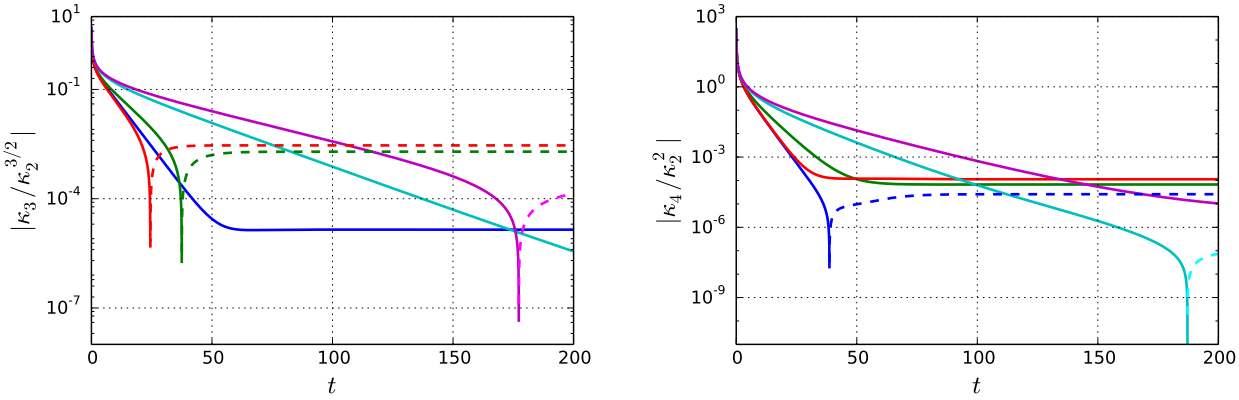


Figure 4.6: Skewness (left panel) and excess kurtosis (right panel) of the motor velocity distribution for motors with mass ratio $\mathcal{M} = 10$, and 40, and $\theta_0 = \pi/4$. Dashed lines represent negative values. *Blue and cyan lines:* $r = 1$ and $\alpha = 1$, elastic collisions with an isotropic gas. *Green and magenta lines:* $r = 0.3$ and $\alpha = 1$, strongly inelastic collisions with an isotropic gas. *Red lines:* $r = 1.0$ and $\alpha = 1.02$, elastic collisions with a slightly anisotropic gas. The magenta and cyan lines represent motors with $\mathcal{M} = 40$.

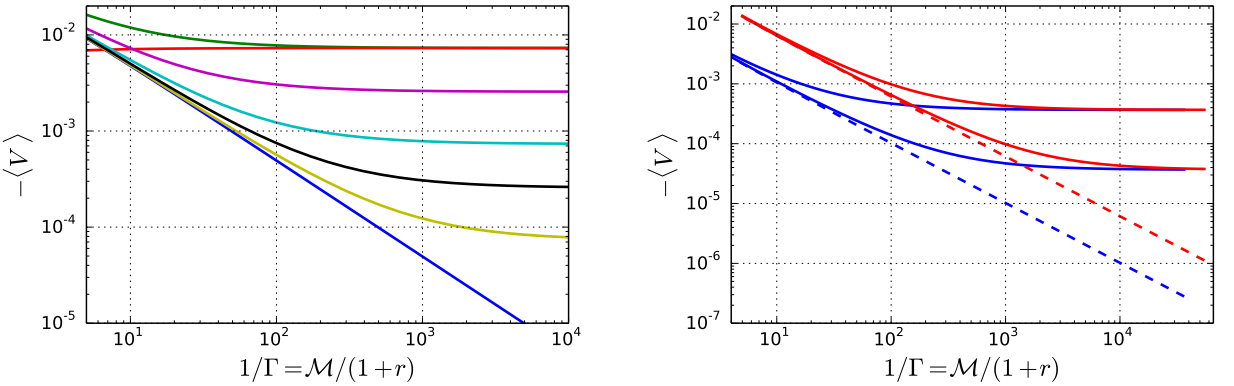


Figure 4.7: Effect of anisotropy on the drift-mass scaling. (left) Motor drift as a function of mass. The blue line represents the motor drift with inelastic collisions in an isotropic gas. The red line represents the motor drift with with elastic collisions in an anisotropic gas. All other curves are for inelastic collisions ($r = 0.3$) for a range of anisotropies: $\alpha \in \{1.02, 1.007, 1.002, 1.0007, 1.0002\}$ all from top to bottom. Increasing anisotropy causes increasing drift at high $\mathcal{M}$. (right) An illustration of the effect of anisotropy compared to the effect of inelastic collisions. Colour represents different coefficient of restitution $r = 0.8$ (blue lines), and $r = 0.2$ (red lines). For small mass the effect of anisotropy is negligible, and for increasing mass, the effect of inelastic collisions can be ignored.

excess kurtosis, indicating that the steady-state distribution remains wider than a Gaussian.

In the subsequent sections, we examine the parameter dependence of the steady-state drift, $\langle V \rangle$, and motor temperature, $\mathcal{T}$, respectively.

## 4.6 MOTOR DRIFT

Here we shall examine the dependence of the steady-state motor drift, $\langle V \rangle$, as a function of mass. As we have seen in Fig. 4.3, increasing the motor mass means that the matrix, $A$, governing the time evolution of the moment expansion becomes increasingly diagonal. Consequently, the moment hierarchy becomes less strongly coupled for increasing $\mathcal{M}$. This shall be the basis of an asymptotic theory for the motor drift (and diffusion) with $\mathcal{M}$ as a control parameter.

Fig. 4.7 (left panel) shows the drift as a function of $\mathcal{M}$ for a fixed coefficient of restitution[5], $r = 0.3$, and a range of anisotropies $\alpha \in \{1.02, 1.007, 1.002, 1.0007, 1.0002\}$. The blue line shows the mass-dependence of the drift for inelastic collisions with particles with isotropic velocity distribution. In agreement with the theory for the isotropic gas [8], the velocity initially scales as $1/\mathcal{M}$.

5. A coefficient of restitution of $r = 0.3$ corresponds to a *very* inelastic material

In contrast, the red line shows the converse; motor drift due to elastic collisions with particles whose velocity distribution is anisotropic. While, for inelastic collisions, the drift velocity decreases for increasing mass, for collisions with anisotropic velocity distribution, the drift is independent of motor mass. For large $\mathcal{M}$ and $\alpha \neq 1$ it approaches a constant value depending only on $\alpha$ and $\theta_0$. This is illustrated by the right panel. It shows what happens when collisions are both inelastic and particles have anisotropic velocities.

**Light Motors:** The drift for light motors is essentially only dependent on the coefficient of restitution, $r$. The effect of gas anisotropy is negligible compared to the effect of dissipative collisions. This is called the *restitution-dominated* regime.

**Heavy Motors:** When motor mass becomes large, the drift velocity saturates at a level set by the gas anisotropy. This is called the *anisotropy-dominated* regime.

We conclude that the drift for light motors is affected primarily by the inelastic nature of the gas-motor interactions. Here the theory for the isotropic gas is a good approximation. In contrast, massive motors are more strongly influenced by the anisotropy of the gas, no matter how slight this may be.

In order to fully characterize the crossover from the restitution to the anisotropy-dominated regime, we consider the limit of a *massive motor*: $\mathcal{M} \to \infty$. In this limit the $\gamma_i$ term in Eq. (2.3b) simplifies,

$$\gamma(r, \mathcal{M}, \theta) \simeq \frac{1+r}{\mathcal{M}} \sin^2\theta =: \Gamma \sin^2\theta \,. \tag{4.17}$$

Due to this factorization of $\sin\theta$ and $\Gamma$, massive motors undergoing dissipative collisions ($r < 1$) behave like motors undergoing elastic collisions ($r = 1$) yet with a slightly higher mass. This is in

agreement with results for the granular Boltzmann equation [40, 41]. Consequentially, the limit of a massive motor corresponds to the limit $\Gamma \to 0^+$ and is independent of restitution, $r$.

We observe that, for small $\Gamma$,

$$d_{n,i} \simeq \Gamma^n \,, \tag{4.18a}$$
$$d_{1,0} \simeq (\alpha - 1) \cdot \Gamma \,. \tag{4.18b}$$

Hence, for isotropic gasses (where $\alpha = 1$), the matrix defined by Eq. (3.36) becomes lower-triangular in leading order of $\Gamma$. This corresponds to the decoupling of the time-evolution equations for the moments, as observed in [8]. In contrast, for $\alpha > 1$, the time evolution equations for the moments become coupled:

$$A \simeq \begin{pmatrix} 0 & 0 & 0 & \cdots \\ d_{1,0} & d_{1,1} & d_{1,2} & \cdots \\ 0 & 2d_{1,0} & 2d_{1,1} & \cdots \\ \vdots & \vdots & \vdots & \ddots \end{pmatrix} . \tag{4.19}$$

The asymptotic behaviour of Eq. (4.19) shall be the starting point of a perturbation theory around $(\Gamma, \alpha) = (0^+, 1)$. We assume that, in the limit $\Gamma \to 0^+$ the steady state is still largely independent of truncation size for small $(\alpha - 1)$. Hence, we find that the null space of the upper left $2 \times 2$ sub-matrix of Eq. (4.19) accurately determines the steady state drift due to anisotropy,

$$\langle V \rangle_{\text{ani}} \simeq -\frac{d_{1,0}}{d_{1,1}} \simeq \sqrt{\frac{\pi}{2}} \, (\sin\theta_0 - 1) \, (\alpha - 1). \tag{4.20}$$

Eq. (4.20) does not depend on $\mathcal{M}$. This is remarkable since it implies that the drift *velocity* of the massive motor is of the order of the gas-particle velocity (*i. e.* the dimensionless $\langle V \rangle_{\text{ani}}$ is of the order 1), even though the transferred momentum from the gas remains constant with increasing $\mathcal{M}$.

The crossover occurs when the drift for the isotropic case $\langle V \rangle_{\text{iso}} \simeq (1 - r)\mathcal{M}^{-1}\sqrt{\pi/2}(\sin\theta_0 - 1)/4$ [8] is of the same order as the drift due to anisotropy. Consequently the dimensionless number,

$$\beta := \frac{\langle V \rangle_{\text{ani}}}{\langle V \rangle_{\text{iso}}} = \frac{4\mathcal{M}(\alpha - 1)}{1 - r}, \tag{4.21}$$

characterizes the dominant driving of the motor. For $\beta \ll 1$, the dynamics is driven by inelastic collisions ($r < 1$), and for $\beta \gg 1$ the dynamics is driven by anisotropy ($\alpha > 1$). Plotting $\langle V \rangle / \langle V \rangle_{\text{ani}}$ as a function of $\beta$ provides an excellent data collapse (Fig. 4.8).

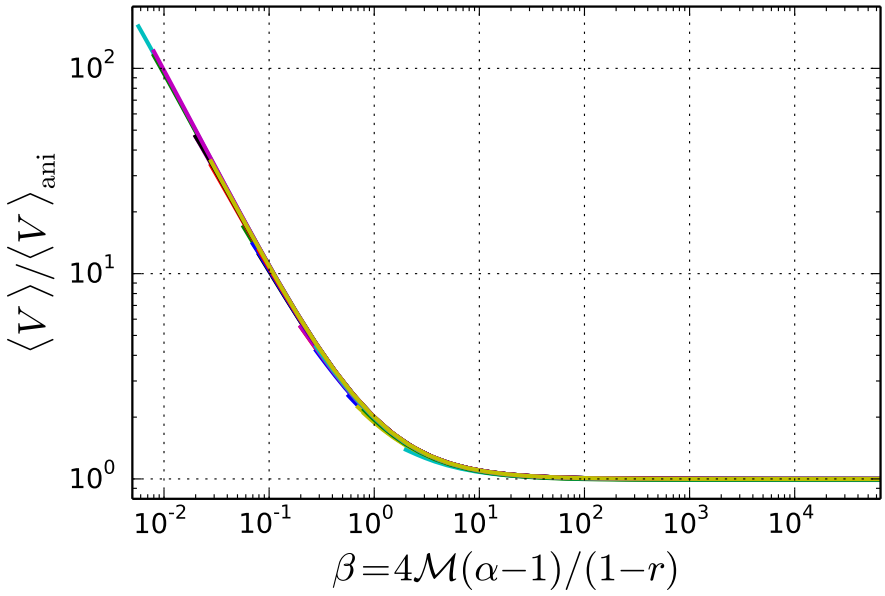


Figure 4.8: Master plot for the motor drift displating the data for all combinations of $\theta_0 = \pi/4$, $r \in \{0.3, 0.5, 0.8\}$, $\alpha \in \{1.02, 1.007, 1.002, 1.0007, 1.0002\}$; and $\theta_0 = \pi/10$, $r = 0.5$, $\alpha \in \{1.02, 1.007, 1.002, 1.0007, 1.0002\}$.

## 4.7 MOTOR TEMPERATURE

We define the motor temperature as the random component of the motor's kinetic energy

$$\mathcal{T} := \mathcal{M}\left(\left\langle V^2\right\rangle - \langle V\rangle^2\right) . \tag{4.22}$$

Fig. 4.9 shows that the temperature is independent of $\mathcal{M}$ for $\mathcal{M} \gtrsim 10$ and it is affected by inelastic collisions more severely than by anisotropy. In order to understand this dependence, we follow the perturbation theory of the previous section to determine the correction to $\mathcal{T}$ in first order of $(\alpha - 1)$.

Since the motor temperature contains a coefficient of $1/\Gamma$, we must expand $A$ at least to second order in $\Gamma$ in order to accurately evaluate the limit $\Gamma \to 0^+$. Based on Eqs. 4.18 we find

$$A \simeq \begin{pmatrix} 0 & 0 & 0 & 0 & \cdots \\ d_{1,0} & d_{1,1} & d_{1,2} & d_{1,3} & \cdots \\ d_{2,0} & 2d_{1,0}+d_{2,1} & 2d_{1,1}+d_{2,2} & 2d_{1,2}+d_{2,3} & \cdots \\ 0 & 3d_{2,0} & 3d_{1,1}+3d_{2,1} & 3d_{1,2}+3d_{2,2} & \cdots \\ \vdots & \vdots & \vdots & \vdots & \ddots \end{pmatrix} \tag{4.23}$$

This results in a further increase of the coupling between the different moments. In order to reliably compute $\langle V^2\rangle_{\rm ani}$, the null-space of at least the upper left $4 \times 4$ sub-matrix of Eq. (4.23) must be used. This yields the asymptotic expression for the temperature,

$$\frac{2}{1+r}\,\mathcal{T}_{\rm ani} \simeq 1 + \left[\frac{4-\pi}{4}(1-\sin\theta_0)^2 + \sin^2\theta_0\right](\alpha - 1). \tag{4.24}$$

The lower panel of Fig. 4.9, shows the converge onto this asymptotic value.

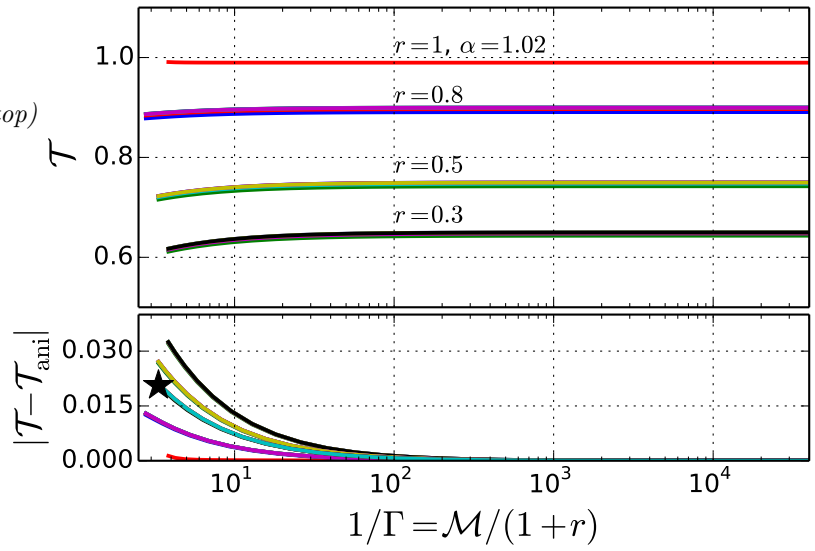


Figure 4.9: Data for all combinations of $\theta_0 = \pi/4$, $r \in \{0.3, 0.5, 0.8\}$, $\alpha \in \{1.02, 1.007, 1.002, 1.0007, 1.0002\}$; and $\theta_0 = \pi/10$, $r = 0.5$, $\alpha \in \{1.02, 1.007, 1.002, 1.0007, 1.0002\}$. *(top)* The motor temperature, $\mathcal{T}$, for $\theta_0 = \pi/4$, $r \in \{0.3, 0.5, 0.8\}$, $\alpha \in \{1.02, 1.007, 1.002, 1.0007, 1.0002\}$. *(bottom)* The difference between motor temperature and the asymptotic theory. For comparison, $\theta_0 = \pi/10$, $r = 0.5$, $\alpha \in \{1.02, 1.007, 1.002, 1.0007, 1.0002\}$ is also shown ($\star$).

Instead of using Eq. (4.24) to plot a master plot, Fig. 4.9 is far more instructive. In leading order, the temperature depends only on the coefficient of restitution, $r$. In contrast, the dependence of temperature on the anisotropy is a higher order effect. Fig. 4.9 shows that the coefficient of $\alpha - 1$ in Eq. (4.22) is small compared to 1: Fig. 4.9 shows the motor temperature for a range of $r$ and $\alpha$, yet the curves with the same $\alpha$ almost fall on top of one another.

## 4.8 MOTOR ENERGY AND EQUIPARTITION

Let us denote the average energy of a gas particle by $\epsilon$ and the kinetic energy of the sub-system[6] by $\mathcal{E}$. Many studies of systems out of equilibrium have noted that equipartition does not hold, even in the steady state [8, 9, 25, 32, 38]. In these studies, the violation of equipartition ultimately results in the relationship $\mathcal{E} = c\epsilon$, where $c \neq 1$ does not depend on $\mathcal{M}$.

6. In our case, this would be the motor

Consider the granular Brownian motor for inelastic collisions with a gas with isotropic particle velocities. Eq. (4.24) tells us that in the limit of large $\mathcal{M}$, the motor's temperature will depend only on the coefficient of restitution $\mathcal{T} \simeq (1 + r)/2$. Hence, the motor's kinetic energy remains the same fraction of $\epsilon$ independent of its mass.

The implication of Eq. (4.24) is relatively profound in the context of constant drift at large $\mathcal{M}$. $\mathcal{T}$ is the kinetic energy that is *not* part of the centre-of-mass kinetic energy of an ensemble of motors. Eq. (4.24) tells us that, no matter the mass of the motor, this part of the kinetic energy is constant. Moreover, since the motor drift *velocity* is constant also the centre-of-mass motion contains an increasing fraction of the energy. This way, $\mathcal{E}/\epsilon$ diverges with $\mathcal{M}$.

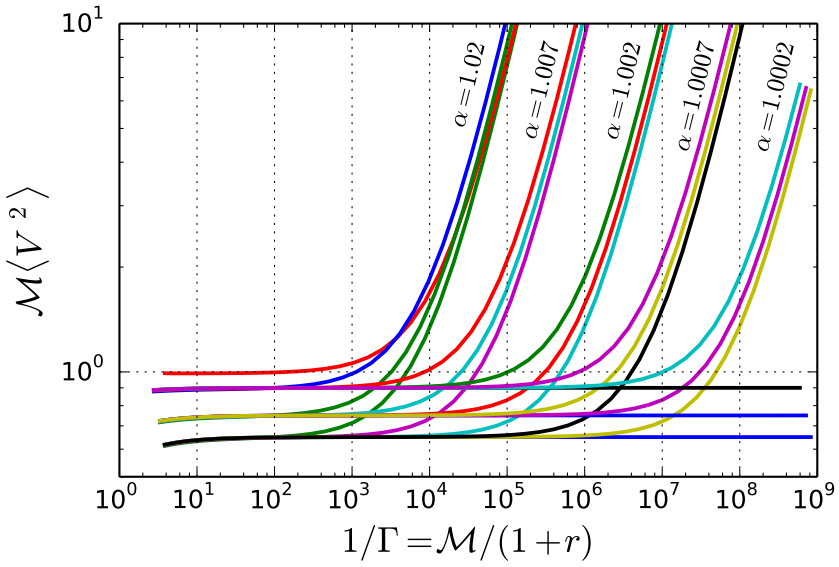


Figure 4.10: Motor kinetic energy as a function of mass. Data and color are in correspondence to Fig. 4.9. For an isotropic gas, the kinetic energy is independent of mass. The relation of motor kinetic energy to gas kinetic energy is a function only of $r$. For an anisotropic gas, regardless of $r$, the kinetic energy diverges.

Fig. 4.10 shows the kinetic energy of the motor as a function of mass. Indeed, for an anisotropic gas, the kinetic energy of the motor diverges. This is due to the diverging centre-of-mass energy. Hence, for increasing motor mass, the motor will have acquired and increasing amount of kinetic energy.

Equipartition is therefore not only broken with the motor's energy being restricted to a *fixed* of $\epsilon$. One can use $\mathcal{M}$ to tune the motor's kinetic energy to an *arbitrary* amount. Considering all the degrees of freedom[7], in the limit $\Gamma \to 0^+$ equipartition is then dramatically broken: *one* degree of freedom (the one representing the motor), contains an *infinite* amount of energy.

In this respect, it is analogous to granular Brownian motors (or pistons) with heterogeneous coefficients of restitution along their surface [11, 12]. Even though the observation that equipartition is broken so dramatically had not been made.

7. *i. e.* all degrees of freedom and the gas, plus one more degree of freedom due to the motor

## 4.9 SUMMARY

We have investigated the motion of a granular Brownian motor that is driven by inelastic collisions (particle-motor coefficient of restitution $r$) sampled from an anisotropic velocity distribution (with anisotropy $\alpha - 1$), modelled using a squeezed Gaussian, Eq. (4.4).

Examining the scaling of the drift with relative motor mass, $\mathcal{M}$, we identified a crossover from the motor drift arising due to inelastic gas-motor collisions, to a setting where it arises predominantly from the anisotropy of the gas. Examining the steady-state drift of the motor in the limit of large $\mathcal{M}$, we have identified a dimensionless parameter $\beta = 4\mathcal{M}(\alpha - 1)/(1 - r)$, Eq. (4.21), that is independent of wedge angle and yet fully characterizes the parameter dependence

of the motor drift. For $\beta \ll 1$ inelastic collisions drive the drift of the motor, and anisotropy is negligible; for $\beta \gg 1$ anisotropy dominates the drift and restitution in motor-gas collisions becomes negligible. In the latter regime we have identified a remarkably strong enhancement of the drift. It is of the order of gas particle *velocity*, even in the limit of infinite motor-particle mass ratios.

In the anisotropy-dominated regime, equipartition is broken dramatically. In an isotropic gas, the degree of equipartition-breaking is set entirely by the amount of dissipation. For an isotropic system, the motor can never acquire *more* kinetic energy than the average kinetic energy of the particles. However, In the anisotropic system, the motor acquires constant drift *velocity*, irrespective of mass. Hence, more massive motors will acquire more kinetic energy, with no upper bound.

Is this regime accessible experimentally? Laboratory experiments can have an anisotropy of the order of $\alpha \approx 2$,[8] and the most conservative estimate for simulations yields $\alpha \approx 1.12$ ([53] Fig 4, inset). Given maximally inelastic collisions ($r$ close to 0) this amounts to $\beta \approx 0.5\mathcal{M}$. For $\mathcal{M} > 10$ typical experimental realizations therefore probe, at best, the crossover regime rather than a regime where the drift solely arises from the inelastic collisions. If one wishes to probe the latter regime, isotropy of the gas particles must be enhanced by at least two orders of magnitude for the experimental setups we are aware of.

8. Matthias Schröter, private communications

The dramatic enhancement of the drift thus lies in an easily accessible regime, and it certainly calls for further experimental and numerical exploration.

## 4.10 OUTLOOK

According to Eq. (4.22) the motor's temperature is hardly affected by anisotropy compared to the effect of dissipation. Yet anisotropy can lead to significant drift. Our intuition from thermodynamics tells us that rectification is associated with a heat flow. When rectification occurs due to dissipation, then this heat flow takes the form of a flow of energy, from the gas, that is being dissipated. The motor's reduced temperature, when collisions are dissipative, reflects exactly this energy flow.

What if the collisions are elastic, yet the gas is anisotropic? Then there is still considerable drift, in spite of the negligible temperature difference. Heat can still flow. The second law of thermodynamics tells us that if there is a heat flow between two reservoirs with the same temperature, then this heat flow takes the form of entropy currents. When an impinging particle collides with the motor surface, then its velocity distribution is changed. However, we have prescribed that the velocity distribution of the gas does not

change. In this way, our model is implicitly re-arranging the velocity distribution after every collision. This comes as the cost of entropy.

While thermodynamics is not directly applicable to the Brownian motor, analogues to the second law have been formulated in the framework of stochastic-thermodynamics [3, 26, 28, 49]. Hence, entropy currents as they are defined within stochastic-thermodynamics appear to be a promising candidate for explaining the drift in the anisotropic regime.

# 5 Rectification Extremely far from Equilibrium: Brownian Motors in a Bath of Swimmers

## 5.1 Introduction

The most general message to take from the previous chapter is that even a small restriction of one degree of freedom of the gas particles results in a dramatic effect on the motor velocity. In light of this finding a natural question is to ask what happens if one degree of freedom is removed completely.

The present chapter therefore addresses the motion of the Brownian motor driven by collisions with particles of constant speed and uniformly random orientation. Real world systems that exhibit this kind of motion include self-propelled mechanical and chemical swimmers, as well as swimming bacteria. There is also an experimental realization of a bacterial Brownian ratchet where E. coli bacteria are driving an asymmetric cog [15].

## 5.2 Model

The treatment of a gas comprised of swimmers complicates matters mathematically. In order to retain oversight, we restrict ourselves to only a single wedge angle $\theta_0 = \pi/4$ and only to elastic collisions, $r = 1$. Investigations involving different wedge angles and coefficients of restitution showed no qualitatively different behaviour.

### *5.2.1 Gas Velocity Distribution*

Most work on swimmers focuses on the emergent dynamics due to swimmer–swimmer interaction. In this chapter we shall consider only the most essential feature of swimmers, that is, a swimmer is a particle with fixed speed and uniformly distributed orientation.

In the laboratory, one might expect a gas of such particles to look like a dilute gas of identical swimmers. As such, we consider a gas where all particles have the same speed $\nu$, but uniformly distributed orientation. Hence $\hat{v}_x^2 + \hat{v}_y^2 = \nu^2$ for every particle, and the associated velocity distribution is

$$\phi_\nu(\hat{v}_x, \hat{v}_y) = \frac{1}{\pi}\delta\left[\hat{v}_x^2 + \hat{v}_y^2 - \nu^2\right] . \tag{5.1}$$

Such a velocity distribution will faithfully describe a gas of swimmers as long as the concentration remains low enough to avoid any collective effects between different swimmers. The low-concentration criterion is not unique to this model, the anisotropic granular gas, dealt with in chapter 4, also required the concentration to be low enough to avoid the motor $\rightarrow$ gas coupling causing local velocity correlations [12, 13].

### *5.2.2 Dimensionless Units*

We may non-dimensionalize velocities using the speed of the gas particles, $\nu$. Hence, non-dimensional velocities[1] are given by $v := \hat{v}/\nu$. $\phi_\nu(\hat{v}_x, \hat{v}_y)\mathrm{d}\hat{v}_x\mathrm{d}\hat{v}_y = \phi_1(v_x, v_y)\mathrm{d}v_x\mathrm{d}v_y$ is automatically fulfilled.

1. denoted by un-hatted symbols

Gas density is used to non-dimensionalize time. This fixes the collision rate between motor and particles when the motor is at rest, see the $y$-value of Fig. 5.2.

As a consequence, only the choice of the coefficient of restitution, $r$, and the mass ratio, $\mathcal{M}$, influence the dynamics of the Brownian motor.

This leaves only two other parameters which may influence the dynamics of the Brownian motor: the coefficient of restitution, $r$, and the mass ratio of motor mass over gas-particle mass, $\mathcal{M} := M/m$.

## 5.3 TRANSITION RATES

For the model discussed in the previous section, the transition rates for collisions resulting in a velocity change from $V \rightarrow V+u$, are given by Eq. (3.9). Yet the expansion Eq. (3.40b), where the gas-velocity distribution is expanded in terms of independent Gaussian basis functions, is no longer possible since Eq. (5.1) does not separate into independent distributions for the $v_x$ and $v_y$ velocity components. A faithful expansion would require a 2–dimensional expansion which would be very tedious. Instead, it is faster to simply perform the

integral in Eq. (3.9), this yields:

$$W(V;u) = \sum_{i\in\{0,1,2\}} w_i(\theta_0) \frac{[\![-u\sin\theta_i]\!]}{\gamma^2(r,\mathcal{M},\theta_i)} \int_{\mathbb{R}} \phi_1\left(\frac{u}{\gamma(r,\mathcal{M},\theta_i)} + V + v_y\cot\theta_i, v_y\right) \mathrm{d}v_y \ , \tag{5.2}$$

which in turn can be integrated analytically. Due to the singular behaviour of $\phi_1(v_x, v_y)$, the integral in Eq. (5.2) is a principal-value integral. The domains $(V,u) \in \mathbb{D}^{\pm}$ over which the $\delta$-function in Eq. (5.2) takes non-vanishing values are given by

$$\mathbb{D}^+ := \left\{(V,u)\in\mathbb{R}^2 \middle| u \geq 0 \wedge 1 > (u/\Gamma_+ + V)^2\right\} \tag{5.3}$$

$$\mathbb{D}^- := \left\{(V,u)\in\mathbb{R}^2 \middle| u \leq 0 \wedge 2 > (u/\Gamma_- + V)^2\right\} \tag{5.4}$$

Following the same approach as the previous chapters, we arrive at the transition rates. They can be decomposed into forward and backward transitions

$$W(V;u) = W^+(V;u)[\![(V,u)\in\mathbb{D}^+]\!] + W^-(V;u)[\![(V,u)\in\mathbb{D}^-]\!] \ , \tag{5.5a}$$

where

$$W^+(V;u) = \frac{u}{\pi\Gamma_+^2}\frac{\sqrt{2}-1}{\sqrt{1-(u/\Gamma_+ + V)^2}} \ , \tag{5.5b}$$

$$W^-(V;u) = \frac{u}{\pi\Gamma_-^2}\frac{\sqrt{2}-2}{\sqrt{2}\sqrt{2-(u/\Gamma_- + V)^2}} \ . \tag{5.5c}$$

They involve dissipation-mass ratios $\Gamma_+ := \frac{1+r}{1+\mathcal{M}}$, and $\Gamma_- := \frac{1+r}{1+2\mathcal{M}}$, which are inspired by the massive-motor limit from the previous chapter. The fact that $r$ and $\mathcal{M}$ do not appear on their own[2] indicates that, in the limit of a massive motor, effects due to dissipation vanish. However, since $\Gamma_+ \neq \Gamma_-$ for $\mathcal{M}$ small, we expect dissipation to affect the motion when $\mathcal{M}$ is small.

2. And because $\Gamma_+ = \Gamma_-$ for $\mathcal{M} \gg 1$.

Let $\mathbb{D} := \mathbb{D}^+ \cup \mathbb{D}^-$. Fig. 5.1 shows a graphical representation of these transition rates and $\mathbb{D}$. The set $\mathbb{D}$ is not convex, it has a small "nose" for $V \in \left(-\sqrt{2}, -1\right)$. Consequently, for these values of $V$, $W(V,u)$ is non-zero for values of $u$ in a disjoint union two intervals. This is shown by the green line in the right panel of Fig. 5.1. The shaded area shows the interval of $u$ over which $W(-1.1,u)$ drops to zero as a result of this "nose". At some of the boundaries of $\mathbb{D}$, the transition rates develop rainbow singularities, that is, $W(V;u) \simeq 1/\sqrt{u^2-c}$.

When tracking the history of the motor directly the velocity, $V$, is known while the velocity increment, $u$, is sampled. Hence, it is

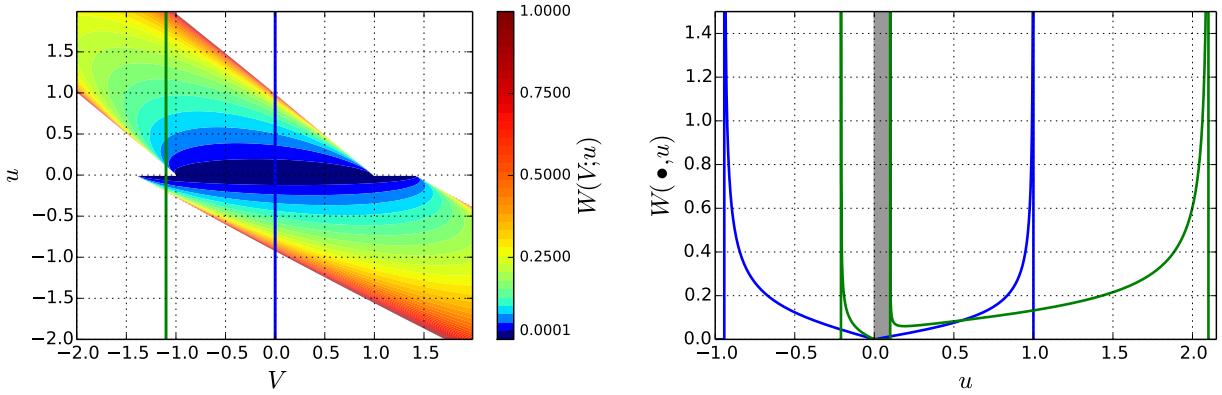


Figure 5.1: (left) Transition rates $W(V,u)$ of a collision resulting in an instantaneous velocity change $V \to V+u$, for the parameters $\mathcal{M}=1$ and $r=1$. Transition rates are represented by colour. White represents $(V,u) \notin \mathbb{D}$. The positions of the corners $V_c = -\sqrt{2}, -1, 1, \sqrt{2}$, are, independent of the parameters $\mathcal{M}$ and $r$. (right) Cross sections for constant $V$, of the transition rates shown in the left panel. The green and blue curves represent the transition rates for $V=-1.1$ and $V=0$ respectively, and correspond to the vertical lines shown in the left panel. The grey shaded area is the internal region in which the transition rates for $V=-1.1$ drop to zero.

not $\mathbb{D}$ (which defines the tuple $(V,u)$ for which $W(V;u) \neq 0$), but the intersection $\mathbb{D} \cap (\{V\} \times \mathbb{R})$ which defines the set of $u$ for which $W(V;u) \neq 0$ given $V$. Using Eq. (5.4), we find that

$$u \in \begin{cases} (a_-(V), a_+(V)) & V < -\sqrt{2} \\ (b_-(V), 0) \cup (a_-(V), a_+(V)) & -\sqrt{2} < V < -1 \\ (b_-(V), a_+(V)) & -1 < V < 1 \\ (b_-(V), 0) & 1 < V < \sqrt{2} \\ (b_-(V), a_+(V)) & V > \sqrt{2} \end{cases} , \tag{5.6a}$$

where $a_\pm(V)$ and $b_\pm(V)$ are the following linear functions of $V$

$$a_-(V) := -\Gamma_+ (1+V) \qquad a_+(V) := \Gamma_+ (1-V) \tag{5.6b}$$

$$b_-(V) := -\Gamma_- \left(\sqrt{2}+V\right) \qquad b_+(V) := \Gamma_- \left(\sqrt{2}-V\right) . \tag{5.6c}$$

Depending on $V$, the domain over which the probability distribution of velocity increments is defined can be one of the five in Eqs. (5.6). The transition rates are continuous within each of these intervals.

The disconnected domain, for $-\sqrt{2} < V < -1$ arises because a particle at the very top (or bottom) corner or the diagonal face (face 0 or 1 in Fig. 2.1), moving directly towards the face, can still catch up with the motor, if the motor moves with a velocity $-1 > V > -\sqrt{2}$. In this way, the motor's speed can be boosted to speeds faster than the gas particles.

The abrupt changes in the domain of $u$ imply, that the jump moments are not well behaved. The points $V = -\sqrt{2}, -1, 1, \sqrt{2}$

constitute points where the derivatives of the jump rates, $\partial_V^n [a_n(V)]$, are no longer smooth. An accurate model, needs to deal with piecewise definitions of the jump rates for each of these five sub-domains of $V$.

### 5.3.1 *Jump Moments*

The spatio-temporal data on the motor's motion is obtained by direct sampling of the motor trajectories (which will be described in section 5.4). Direct sampling is based on the jump *probabilities* of a velocity change $V \to V + u$, rather than the jump *rates* discussed so far. The conversion can easily be done with the collision rate given by the zeroth jump moment, $a_0(V)$,

$$a_0(V) = \frac{\sqrt{2}-1}{\pi} \begin{cases} \sqrt{1-V^2} + \sqrt{2-V^2} + V\left(\sin^{-1} V + \tan^{-1}\left(\dfrac{V}{\sqrt{2-V^2}}\right)\right) & |V| \leq 1 \\ \dfrac{\pi}{2}|V| + \sqrt{2-V^2} + V\tan^{-1}\left(\dfrac{V}{\sqrt{2-V^2}}\right) & 1 < |V| < \sqrt{2} \\ \pi|V| & |V| > \sqrt{2} \end{cases} \tag{5.7}$$

The rate $a_0(V)$ does not depend on $r$ and $\mathcal{M}$ since the collision rate must not depend on the motor mass or restitution coefficient, but only on motor speed and shape. The limiting behaviour of $a_0(V)$ for large $|V|$ also is consistent with our intuition. When the motor is travelling with a speed much larger than that of the swimmers, all particles will seem to have the same effective relative velocity. Moreover, since our model requires that the collision rate is proportional to the relative velocity, $a_0(V) \asymp \left(\sqrt{2}-1\right)|V|$.

Fig. 5.2 shows jump moments $a_0(V)$, $a_1(V)$ and $a_2(V)$ (for the later two, $\mathcal{M} = 1, 2$ and $r = 1, 0.1$, as denoted by the coloured symbols), and their $(n+1)$-st derivatives, which develop cusps whenever the domain of $u$ changes.

The points where the jump moments are not smooth dependent only on the wedge angle and motor shape. These points are always given by the borders of the intervals defining Eq. (5.6a): $V = -\sqrt{2}, -1, 1, \sqrt{2}$. While the jump moments, $a_n(V)$, might not be analytic, they are smooth enough not to generate additional source terms in the moment-hierarchy theory (see Lemma 1 in section 3.5). Hence, although it is still not formally correct to apply the traditional moment expansion, at least for large enough $\mathcal{M}$, the moment-expansion approach is a good approximation. Finally, for all $n$, the functions given by $\partial_V^{n+1}[a_n(V)]$ have a similar shape.

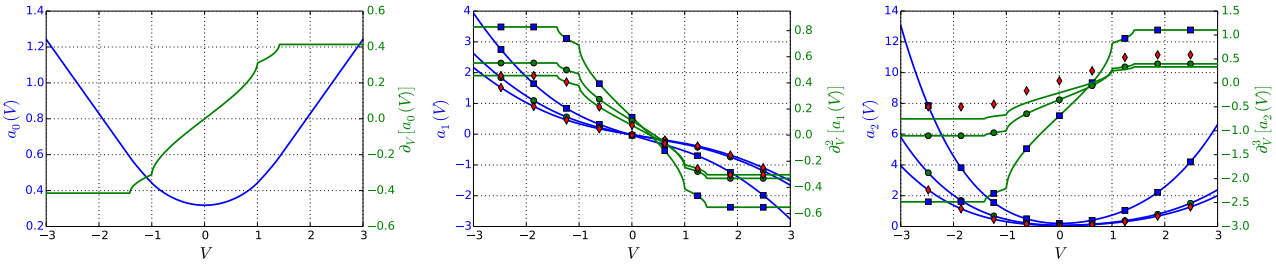


Figure 5.2: The color of the lines corresponds with the axis label color (blue,right; green, left). Colored symbols on lines denote different parameters. (blue squares) $\mathcal{M} = 1$, $r = 1$. (green cirlces) $\mathcal{M} = 2$, $r = 1$. (red diamonds) $\mathcal{M} = 1$, $r = 0.1$. (left) Motor–gas particle collision rate, $a_0(V)$ (blue line and left axis), and its first derivative (green line and right axis). It does not depend on $\mathcal{M}$, or $r$, therefore only one line is shown. At velocities significantly larger than particle velocity ($V = 1$), the collision rate becomes proportional to the motor speed. (centre) Average change of momentum, $a_1(V)$, (blue lines and left axis), and its second derivative (green, right axis). (right) Average energy transferred per collision, $a_2(V)$ (blue lines, left axis), and its third derivative (green, right axis). The derivatives are not differentiable for $V = -\sqrt{2}, -1, 1, \sqrt{2}$, where the domain of $u$ (the collisional velocity increments) changes abruptly. As expected, this is not a function of $\mathcal{M}$, nor $r$.

## 5.4 DIRECT SAMPLING OF TRAJECTORIES

In this section, we begin by looking at the motor trajectories. By directly sampling the transition rates we avoid the mathematical complications that arise due to a piecewise definition of the jump moments. Tracking motor trajectories has two added advantages over solving the moment-hierarchy:

1. It provides data on the spatio-temporal motor trajectories rather than only its velocity;

2. It provides direct data on the distribution of motor positions and velocities.

In order to track motor trajectories, we implement the slice sampling algorithm (Algorithm 2) introduced in Chapter 3, using the transition rates defined in Eqs. (5.5), and Eq. (5.7).

### *5.4.1 Verification of the Sampling Algorithm*

Agreement between the sampled velocity increments and Eqs. (5.5) are checked in Fig. 5.3 (left panel). It is also verified that there is no residual correlation between successive velocity increments (right panel). This was done by holding the motor stationary and sampling the velocity increments for fixed $V$.

The histogram of the sampled velocity increments agrees with the expected transition probability $P(u) := W(V; u)/a_0(V)$ (black lines) within the statistical noise. There are slightly larger deviations for the edges of the domain of $P(u)$, which we attribute to the rainbow singularities (as this deviation only occurs in a bin containing a singularity). Additionally there is excellent agreement

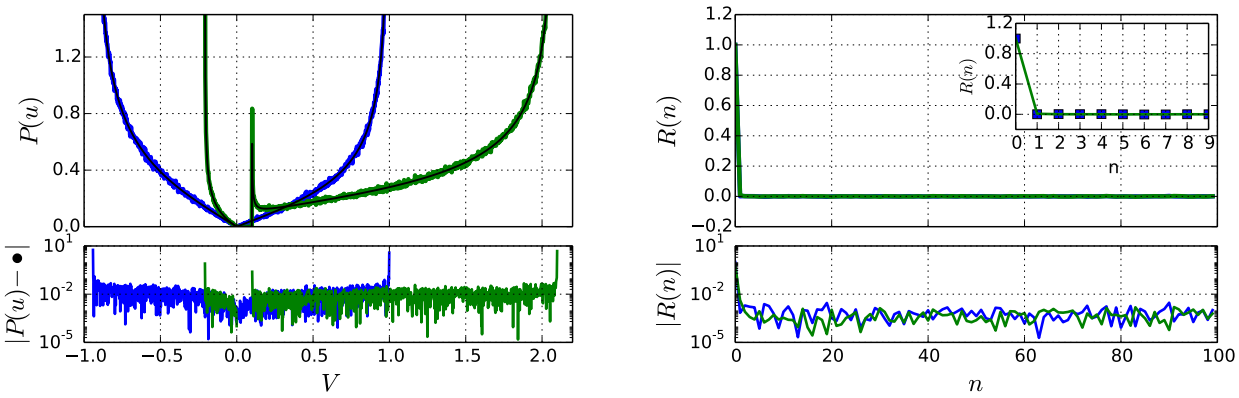


Figure 5.3: Consistency tests to ensure that the random velocity increments which are sampled by Algorithm 2 are indeed the desired random numbers. In this mode, random velocity increments are sampled without incrementing the motor velocity. The parameters correspond to those in Fig. 5.1. *Left top panel:* Histogrammed velocity increments. Black lines are comparisons with the desired random numbers. (left bottom) deviation of the histogram bin value from the desired amount. The increased deviation on the far sides is an artefact of the rainbow singularities. *Right panel* Autocorrelation function, $R(n) := \langle (u_{i+n} - \mu)(u_i - \mu)\rangle/\sigma^2$, for successively sampled random numbers. The bottom panel shows that, whithin the statistical noise the autocorrelation does drop to zero for $n \neq 0$. Hence successive collisions appear uncorrelated to all effective purposes. The inset shows a close-up of the data plotted in the main panel.

when the domain is disconnected, lending confidence to Algorithm 2 for dealing effectively with disconnected domains and functions that contain rainbow singularities.

Fig. 5.3 (right panel) shows that the autocorrelation function takes two values[3]:

$$R(n) := \frac{\langle (u_{i+n} - \mu)\,(u_i - \mu)\rangle}{\sigma^2} = \begin{cases} 1 & n = 0 \\ 0 & n \neq 0 \end{cases}, \qquad (5.8)$$

where $\mu = \langle u \rangle$ is the mean velocity increment for constant motor velocity and $\sigma^2 = \langle (u-\mu)^2 \rangle$ is its variance. This provides strong evidence that Algorithm 2 gives uncorrelated random collisions, with the correct distribution.

[3] The logarithmic plot in Fig. 5.3 (right panel) shows a constant residual correlation. This is because correlation was estimated using a finite sample size ($N = 10^6$ sampled $u$). Numerical examination shows that this residual decays as $1/N$.

## 5.4.2 *Stochastic Trajectories*

Motor trajectories have been sampled for a range of motor masses, ranging from $\mathcal{M} = 0.1$ to $\mathcal{M} = 10^4$ with $r = 1$ and $\theta_0 = \pi/4$.

Fig. 5.5 (left) shows a selection of these velocities. Remarkably, the motor drift reverses direction twice. For very small $\mathcal{M}$, the motor drifts towards the open end (as it did with the anisotropic gas). Then, for increasing $\mathcal{M}$, the motor enters a region where it drifts towards the sharp end for $0.38 < \mathcal{M} < 0.93$. For even larger $\mathcal{M}$, the motor drifts towards the open end again. Motor trajectories for early times are also shown, here the fluctuations are clearly visible. On the time scale of entire trajectories the drift

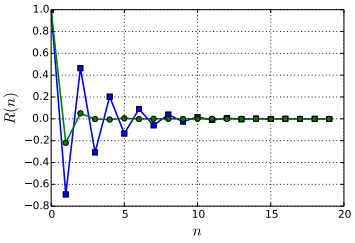


Figure 5.4: Motor velocity autocorrelation function, $R(n)$, two motor masses: $\mathcal{M} = 0.33$ (blue), 1.28 (green). Collisions are not $\delta$-correlated. But they appear to become $\delta$-correlated in the limit $\mathcal{M} \to \infty$.

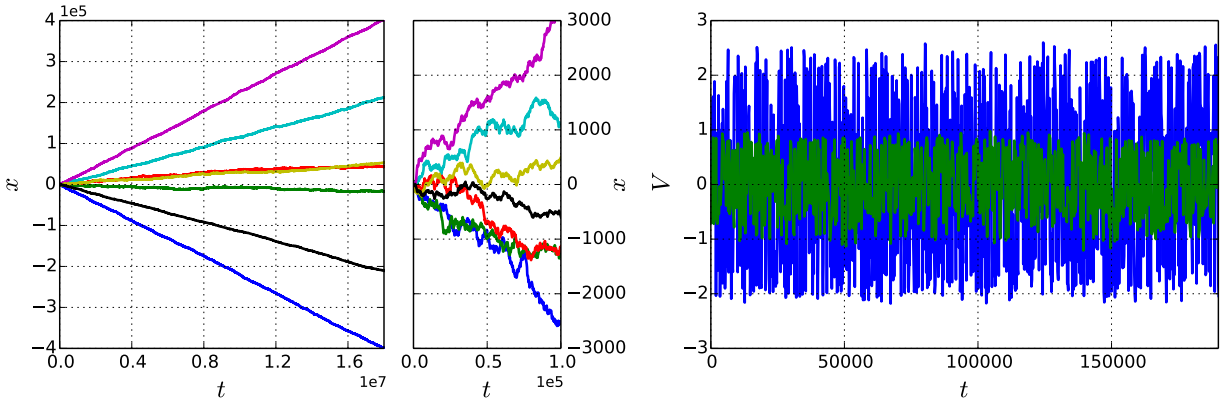


Figure 5.5: Some sampled trajectories showing that the remarkable reversion of the motor drift velocity. (left panel) Motor position for a series of parameters: $r = 1$ for all trajectories, $\mathcal{M} = 0.33$ (blue), 0.38 (green), 0.39 (red), 43 (cyan), 0.53 (purple), 0.87 (yellow), 1.28 (black). The left sub-plot shows every 100-th point in almost the entire sampled trajectory of the motor. We see that, to all intensive purposes, the motor has a constant drift velocity. The right sub-plot shows the time evolution of the motor position at the beginning of the trajectory. This reveals the fluctuations in the motor position. (right) Every 100-th initial motor velocity for $r = 1$ and $\mathcal{M} = 0.33$ (blue), 1.28 (green). The velocity fluctuates wildly, and might seem $\delta$-correlated, but this is a result of plotting only every 100-th point in the trajectory. Fig. 5.4 shows that, especially for the light motor (blue line) strong correlation and anti-correlations exist.

dominates the fluctuations in the motor position. Fig. 5.5 (right) shows part of the motor velocity for two different $\mathcal{M}$ (every 100-th point has been plotted). The velocities, $V$, appear $\delta$-correlated. However, this is not the case as can been seen from Fig. 5.4. For the light motor, $\mathcal{M} = 0.33$, $V$ shows significant correlations up to 10 collisions. For heavier motors, $V$ appears to become $\delta$-correlated, consistent with the observation in the previous chapter: the motor dynamics can be captured by the Fokker-Planck equation for large $\mathcal{M}$ (cf. Fig. 4.1 and section 4.5.1). This remains a tenuous claim as the Fokker-Planck equations require *Gaussian* velocity increments, yet Eqs. (5.5) produce anything but Gaussian velocity increments.

## 5.5 MOTOR VELOCITY DISTRIBUTION

We may use the data from the trajectories to compile histograms of the motor velocity distribution. Fig. 5.6 shows the large, and unusual variety of distributions possible for $P(V)$. The unusual shape initially suggests that the sampling algorithm is producing artefacts. Near all the unusual points observed in $P(V)$, the sampling algorithm was checked and it was observed that:

1. Sampled velocity increments are in agreement with Eqs. (5.5).

2. Sampled velocity increments are uncorrelated.

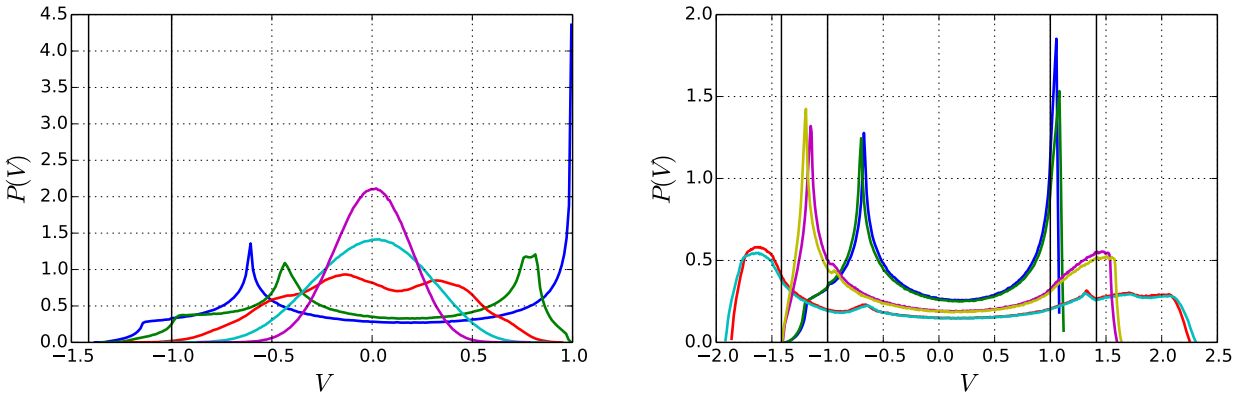


Figure 5.6: Motor velocity distributions for (left) motors heavier than gas particles and (right) motors lighter than the gas particles. Those intervals where the jump moments have a different series expansions are delimited by black vertical lines. For all distributions $r = 1$. (left) Motors significantly heavier than the gas particles show smooth distribution. $\mathcal{M} = 10.24$ (magenta), 5.12 (cyan), 2.56 (red). The distributions for heavy motors might look Gaussian, but they have finite support. Already when $\mathcal{M} = 2.56$ (red), does $P(V)$ become highly non-Gaussian, and its tail extends into the interval $V \in (-\sqrt{2}, -1)$. Once the motor's mass is close to that of the gas particles, $P(V)$ is dominated by singularities and starts to look very unusual. (right) An examination of the points where $V_{\text{drift}}$ changes direction, and the point where it is in the maximum positive direction. $\mathcal{M} = 0.93$ (blue), 0.9 (green), 0.52 (magenta), 0.5 (yellow), 0.31 (red), 0.30 (cyan). Even though the motor's drift velocity does something unusual at each of these points, the distributions undergo only gradual changes.

As such a straight forward failure of the sampling algorithm seems unlikely. It is more likely that the singularities in Eqs. (5.5) are generating singularities in $P(V)$.

Fig. 5.6 (left) shows the distribution for $r = 1$ and $1 \leq \mathcal{M} \leq 10.24$. We see that for reasonably heavy ($\mathcal{M} > 2.56$) motors, $P(V)$ looks reasonably well behaved and might be approximated well by using the moment-hierarchy technique. These distributions also stay out of the region $|V| > 1$, hence, the traditional theory for the moment-hierarchy (see section 3.5) probably holds for these mass ratios. Lighter motor then enter the regime where $P(V)$ becomes highly non-Gaussian and is eventually dominated by singularities as $\mathcal{M}$ decreases. This occurs *before* the motor drifts in the opposite direction. The presence of singularities in $P(V)$ is not an indicator of drift-direction reversal.

Fig. 5.6 (right) shows the motor velocity distributions for $r = 1$ and $0.3 \geq \mathcal{M} \leq 0.93$. In particular those points were chosen where $V_{\text{drift}}$ does something unusual. For example, those masses where the drift velocity changes direction or where it is at its maximal positive (towards the sharp end) velocity. We see that there are no extreme changes in the velocity distribution at these points, in fact, it seems that $P(V)$ changes smoothly with $\mathcal{M}$.

## 5.6 KINETIC THEORY

The traditional moment expansion can be applied as long as the motor velocity never exceeds $|V| > 1$. Looking at the motor velocity distributions, we see that for $\mathcal{M} \gtrsim 3$, there are almost no motors with velocity $|V| > 1$. For this range of motor masses it is reasonable to apply the traditional kinetic theory from section 3.5. Techniques based on moment-hierarchies are only suitable for determining the moments of $P(V)$ for massive motors.

An increasing number of collisions needs to be followed for large $\mathcal{M}$ When determining $P(V)$ by tracking motor trajectories. Here the moment-hierarchy technique gives answers where solving the master equation directly does not.

### 5.6.1 *Expansion of the Jump Moments*

The jump moments, $a_n(V)$, are the sum of the forward, $+$, and backward, $-$, jump moments

$$a_n(V) = a_n^+(V) + a_n^-(V) \,, \tag{5.9}$$

where

$$a_n^\pm(V) = \int_{\Omega(V)\cap\mathbb{R}^\pm} u^n W(V;u)\, \mathrm{d}u \,. \tag{5.10}$$

The forward and backward jump moments are defined over the respective half of the real numbers, $\mathbb{R}^\pm$. As long was the motor mass is sufficiently large, we may restrict ourselves to a domain of Eq. (5.10) is given by

$$\Omega(V) = (b_-(V), a_+(V)) = \left(-\Gamma_-\left(\sqrt{2}+V\right), \Gamma_+(1-V)\right) \tag{5.11}$$

We shall now follow the mathematical working to derive the power series expansion of the jump moments. Inspired by the result for Gaussian-like velocities, for example Eq. (3.41), the goal of this procedure is to arrive at a recursion relation for the expansion coefficients of $a_n^\pm(V)$. Without loss of generality, the working for the forward jump moments only will be presented here.

With the jump rates, Eq. (5.5b), inserted into Eq. (5.10), the expression for the jump rates becomes[4].

4. The final step of Eq. (5.12) is simply the transformation of variables $y := u/\Gamma_+$

$$\begin{aligned} a_n^+(V) &= \int_{\Omega(V)\cap\mathbb{R}^+} u^n W^+(V;u)\, \mathrm{d}u \\ &= \frac{\sqrt{2}-1}{\pi\Gamma_+^2} \int_0^{\Gamma^+(1-V)} \frac{u^{n+1}}{\sqrt{1-(u/\Gamma_+ + V)^2}}\, \mathrm{d}u \\ &= \Gamma_+^n \frac{\sqrt{2}-1}{\pi} \int_0^{1-V} \frac{y^{n+1}}{\sqrt{1-(y+V)^2}}\, \mathrm{d}y \,. \end{aligned} \tag{5.12}$$

Here the scaling of $a_n(V) \sim \Gamma_\pm^n$, familiar from the previous chapter[5]. The Integral in Eq. (5.12) cannot be readily calculated for general $n \in \mathbb{Z}^+$. However, this is not necessary for a power-series expansion, instead, we use the familiar expansion for the root,

$$\frac{1}{\sqrt{a-x^2}} = \sum_{i=0}^{\infty} \binom{-\frac{1}{2}-i}{-\frac{1}{2}} \frac{x^{2i}}{a^{\frac{1}{2}+i}} \,, \tag{5.13}$$

leading to the first expansion

$$a_n^+(V) = \Gamma_+^n \frac{\sqrt{2}-1}{\pi} \sum_{i=0}^{\infty} \binom{-\frac{1}{2}-i}{-\frac{1}{2}} \int_0^{1-V} (y+V)^{2i} y^{n+1} \, \mathrm{d}y \,. \tag{5.14}$$

Now the integral in Eq. (5.14) needs to be expanded in terms of $V$,

$$I_{k,n}(V) := \int_0^{1-V} (y+V)^k y^{n+1} \, \mathrm{d}y = \sum_{i=0}^{\infty} \frac{I_{n,k}^{(i)}(0)}{i!} V^i \,, \tag{5.15}$$

and so the sum in Eq. (5.14) can be done for each term in the expansion in Eq. (5.15) separately, giving the expansion coefficients. The expansion coefficients $I_{n,k}^{(i)}(0)/i!$ are the Taylor[6] expansion coefficients. The $i$-th derivative of $I_{k,n}$, $I_{k,n}^{(i)}$ can be easily found using Leibniz integration rule[7],

$$\partial_V I_{k,n}(V) = \underbrace{\int_0^{1-V} \partial_V \left[(y+V)^k\right] y^n \, \mathrm{d}y}_{k I_{k-1,n}(V)} - (1-V)^n \,. \tag{5.16}$$

Eq. (5.16) can be generalized to the $m$-th derivative, giving

$$\begin{aligned} \partial_V^m I_{k,n}(V) =& \frac{k!}{(k-m)!} I_{k-m,n}(V) \, [\![k \geq m]\!] \\ & - \sum_{i=0}^{m-1} \frac{(-1)^i n!}{(n-i)!} \frac{k!}{(k+i-m+1)!} (1-V)^{n-i} \,. \end{aligned} \tag{5.17}$$

Finally we evaluate the integral, $I_{k-m,n}$, to be used with Eq. (5.17). Integration by parts is the natural choice here, giving a recursion relation

$$\underbrace{\int_0^{1-V} (V+y)^k y^n \, \mathrm{d}y}_{I_{k,n}(V)} = \frac{(1-V)^{n+1}}{n+1} - \frac{k}{n+1} \underbrace{\int_0^{1-V} (y+V)^{k-1} y^{n+1} \, \mathrm{d}y}_{I_{k-1,n+1}(V)} \,. \tag{5.18}$$

Of course, what we want is the derivatives at $V = 0$, so we[8] substitute $V = 0$ into Eqs. (5.17) and (5.18),

$$I_{k,n}(0) =: I_{k,n} = \frac{1}{n+1} - \frac{k}{n+1} I_{k-1,n+1} \tag{5.19a}$$

$$I_{0,n} = \frac{1}{n+1} \,, \tag{5.19b}$$

5. Of course this scaling only makes sense for $\Gamma_+ = \Gamma_-$, as is the case in the limit of $\mathcal{M} \to \infty$.

6. The integral, $I_{k,n}(V)$ might seem tempting to expand via the binomial theorem, but the resulting expression for the coefficient of $V^i$ is just messy this way.

7. Also often called *differentiation under the integral sign*. For a good review, cf. [19].

8. A naive approach would be to recognise that $V = 0$ a bit earlier, and substitute for $V = 0$ before applying Eq. (5.18). This will give the wrong result, however, due to the boundary dependence of $I_{k,n}(V)$.

where the argument has been dropped for $V = 0$.

Returning to our original aim of finding the power-series expansion of the jump moments, Eq. (5.14) gives

$$\begin{aligned} a_n^+(V) &= \Gamma_+^n \frac{\sqrt{2}-1}{\pi} \sum_{k=0}^{\infty} \binom{-\frac{1}{2}-k}{-\frac{1}{2}} I_{k,n}(V) \\ &= \Gamma_+^n \frac{\sqrt{2}-1}{\pi} \sum_{i=0}^{\infty}\sum_{k=0}^{\infty} \binom{-\frac{1}{2}-k}{-\frac{1}{2}} \frac{I_{k,n}^{(i)}}{i!} V^i \end{aligned} \tag{5.20}$$

and so the expansion coefficients for $a_n^+(V)$ are given by:

$$d_{n,i}^+ = \Gamma_+^n \frac{\sqrt{2}-1}{\pi} \sum_{i=0}^{\infty}\sum_{k=0}^{\infty} \binom{-\frac{1}{2}-k}{-\frac{1}{2}} \frac{I_{k,n}^{(i)}}{i!} \quad \text{and,} \tag{5.21a}$$

$$I_{k,n}^{(i)} = \frac{k!}{(k-i)!} I_{k-i,n} [\![k \geq i]\!] - \sum_{j=0}^{i-1} \frac{(-1)^j n!}{(n-j)!} \frac{k!}{(k+j-i+1)!} \,. \tag{5.21b}$$

Where the $I_{k,n}$ terms are dependent only on the domain of $V$, therefore they can be computed using Eqs. (5.19) once and stored for repeated use. The scaling behaviour with respect to $\Gamma$ ofEq. (5.21a) is

$$d_{n,i} \simeq \Gamma^n \,, \tag{5.22}$$

which is the same behaviour[9] as Eq. (4.18a). Hence we use the same asymptotic theory discussed in section 4.6 to estimate the motor's steady state drift in the limit $\mathcal{M} \to \infty$, giving

$$\langle V \rangle_\infty \approx 1.03 \times 10^{-3} \,. \tag{5.23}$$

While this is still an order of magnitude less than the velocity of the gas, it is remarkable that this quantity does not vanish. This result is analogous to the result from chapter 4.

Fig. 5.7 compares the result from the motor trajectories with this prediction. There is overall agreement. The analysis based on the motor trajectories underestimates motor drift for very large motor mass. This is most likely because, for very heavy motors, many collisions are necessary to get a representative sample of the first moment of the distribution.

9. In the limit $\mathcal{M} \to \infty$, $\Gamma_+ = \Gamma_- =: \Gamma$

## 5.7 MOTOR DRIFT

We determine the motor drift using the first moment of the velocity distribution, $\langle V \rangle$. The results are shown in Fig. 5.7 (blue squares).

Alternatively, Fig. 5.5 indicates that the drift velocity can be estimated by extrapolating the motor displacement:

$$V_{\text{drift}} = \left\langle \frac{x_{n+N} - x_n}{t_{n+N} - t_n} \right\rangle_{\mathcal{X},N} \,, \tag{5.24}$$

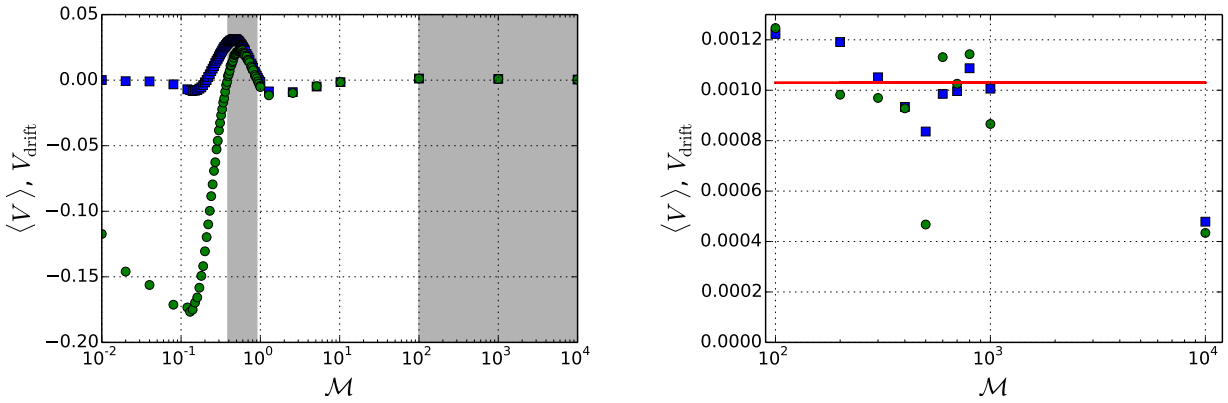


Figure 5.7: *Left panel:* Motor drift given by the first moment of the velocity distribution, $\langle V \rangle$ (blue squares). The drift velocity, $V_{\mathrm{drift}}$, is also measured directly from the motor displacement $x$ via Eq. (5.24) and $N = 1000$ collisions (green circles). Interestingly, they do not agree. Evaluating Eq. (5.24) for incommensurable $N$ shows that this result is independet of $N$. The grey shaded areas are those ranges of $\mathcal{M}$, where $V_{\mathrm{drift}} > 0$. *Right panel:* Motor drift for heavy motors. The result of the moment-hierarchy method is represented by the red line. It does not vanish for the limit $\mathcal{M} \to \infty$! The moment-hierarchy prediction agrees with the data from motor trajectories, in particular when one takes into account that trajectory-based measurements under-estimate the drift due to the limited sample time.

where the expectation value $\langle \bullet \rangle_{\mathcal{X},N}$ is taken over every $N$-th point[10] in the trajectory $\mathcal{X}$.

This estimate for the drift velocity is shown in Fig. 5.7 (green circles). Compared with $\langle V \rangle$, it is clear that the two estimates for drift velocity do not match. Since $V_{\mathrm{drift}}$ is based on the actual motion of the motor, it shall be called the *drift velocity* henceforth.

In section 5.4.2 we have seen is that for $0.38 \lesssim \mathcal{M} \lesssim 0.93$, the motor changes the *direction* in which it drifts. The changes in the motor drift direction are marked in grey areas (the motor drifts towards the pointed end in the grey regions) in Fig. 5.7.

The mismatch $V_{\mathrm{drift}} \neq \langle V \rangle$ highlights a breakdown of ergodicity as $V_{\mathrm{drift}}$ is a time average, and $\langle V \rangle$ is a ensemble average. The breakdown of ergodicity appears to coincide with the collision velocities becoming correlated (cf. section 5.4.2).

The faces 0 and 1 (cf. Fig. 2.1) are at an angle of $\pi/4$ with the axis of motion, as such particles colliding with these faces transfer less of their momentum to the motor than particles colliding with face 2. In this way, on average, the motor should be travelling at a faster velocity in the forward direction than in the backward direction. It stands to reason that the motor will move forwards *faster* than it travels backwards. The effect should become noticeable when $\Gamma_+ \neq \Gamma_-$, which is around $\mathcal{M} \simeq 1$.

The positive drift might eventually be offset by correlations in the free-flight time between collisions. When the motor is travelling quickly it is more likely to collide with a particle. Hence the forward time of free flight is less than the backward time of free flight. It therefore stands to reason that when velocities become anti-

10. To avoid artefacts due to correlated velocities, only one in every $N$ data points goes into the expectation value in Eq. (5.24).

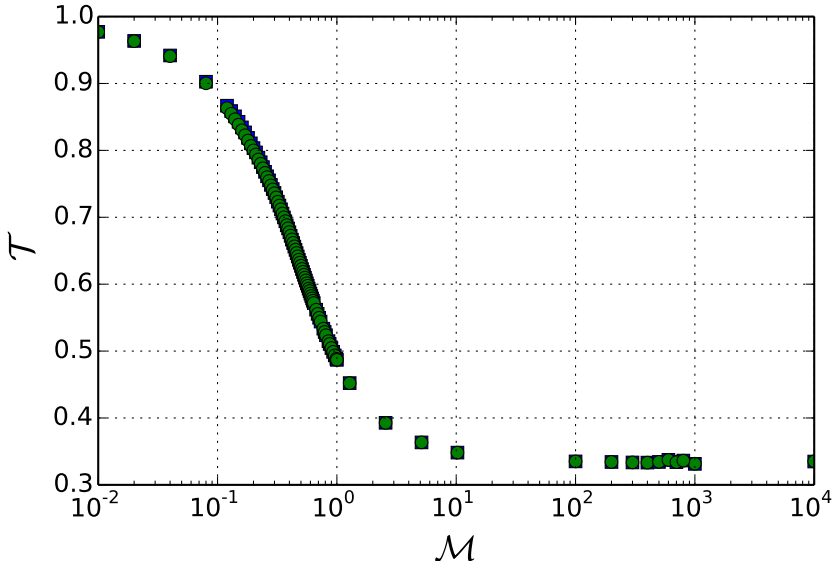


Figure 5.8: *Blue squares:* Motor temperature based on velocity statistics $\mathcal{T} = \mathcal{M}\langle(V - \langle V\rangle)^2\rangle$. *Green circles:* Motor temperature, with $V_{\text{drift}}$ as a measure for centre-of-mass velocity: $\mathcal{M}\left(\langle V^2\rangle - V_{\text{drift}}^2\right)$

correlated, as they are in Fig. 5.4, the motor spends more *time* going backwards. This appears to be the case when $\mathcal{M} \lesssim 0.38$.

In the limit for very massive motors, the result of the moment-hierarchy shown in Eq. (5.23) is in agreement with the motor trajectory data as shown in Fig. 5.7 (right panel). Especially when considering that the motor drift, for heavy motors, is underestimated using the trajectory data. A finite drift in the limit $\mathcal{M} \to \infty$ was also observed in chapter 4.

## 5.8 MOTOR TEMPERATURE

The motor temperature, Eq. (4.22), as a function of $\mathcal{M}$ is shown in Fig. 5.8 (blue squares). The motor drift velocity is fairly large for low motor masses. Since rectification classically associated with a heat flow, one might initially expect a larger difference in system and bath temperature whenever motor drift is large. Fig. 5.8 shows the opposite relationship: motor temperature is closest to the bath (*i. e.* to $\mathcal{T} = 1$) for low masses where drift is largest. This parallels our findings from chapter 4 where large drift occurs in the presence of a small motor–gas temperature difference.

When the motor mass is very large the drift becomes small. Yet in this regime we encounter the most is a significant temperature difference between motor and bath. It is reasonable that this temperature difference sustains the finite steady state drift for infinitely massive motors, Eq. (5.23).

Motor temperature is defined as the kinetic energy of the random velocity fluctuations (cf. section 4.7). Since motor drift, $V_{\text{drift}}$ no longer agrees with with first moment of the motor velocity

distribution, an alternative definition of motor temperature is

$$\mathcal{T} = \mathcal{M}\left(\langle V^2\rangle - V_{\text{drift}}^2\right) \ . \tag{5.25}$$

In Fig. 5.8, we compare Eq. (5.25) (green circles) with Eq. (4.22) (blue squares). Within the numerical error, they overlap perfectly. This might seem surprising at first, since there is an appreciable difference between $V_{\text{drift}}$ and $\langle V\rangle$, for low $\mathcal{M}$. Both estimates for motor temperature still give the same result because for low motor masses the temperature is dominated by $\langle V^2\rangle$.

## 5.9 SUMMARY

In this chapter, we have examined the motion of a Brownian motor, driven by collisions from a thermostatted bath where the particles have constant speed. This can be thought of as a model for a gas consisting of self-propelled swimmers in the absence of collective effects, such as swarming.

This particular choice of the gas velocity distribution, Eq. (5.1), cannot be factorized. Hence a the integral, Eq. (3.9) needs to be carefully treated from scratch. The resulting velocity transition rates develop rainbow singularities for certain finite velocity increments. As a consequence, the moment-hierarchy method cannot be applied to solve for the motor velocity distribution when $\mathcal{M} \lesssim 3$. Hence we have examined the motor trajectories directly.

The motor velocity distribution appears well behaved (looking almost Gaussian) for large $\mathcal{M}$, but develops singularities when $\mathcal{M} \lesssim 1$. Algorithm 2, with which motor trajectories were sampled, was checked to ensure that these singularities are not an artefact of the numerics.

For $\mathcal{M} \lesssim 1$, the first moment of the motor's velocity distribution, $\langle V\rangle$, does not agree with the linear drift in the motor position, $V_{\text{drift}}$, cf. Eq. (5.24). Since $\langle V\rangle$ is an ensemble average, and $V_{\text{drift}}$ is a time average, $\langle V\rangle \neq V_{\text{drift}}$ shows that this system becomes non-ergodic for $\mathcal{M} \lesssim 1$.

When $0.38 \lesssim \mathcal{M} \lesssim 0.93$, the motor drifts in the positive direction[11]. Outside this range of mass ratios, the motor drift is negative. The limit of $\mathcal{M} \to \infty$ appears to show non-vanishing positive drift. This parallels our findings from chapter 4.

11. Towards the sharp end

The motor temperature, shows the same counter-intuitive behaviour as in chapter 4. For those mass ratios where the drift is largest, the motor temperature is close to the temperature of the gas. Hence, again the heat flow is likely to be due to an entropy current, rather than an energy flow.

### 5.9.1 *Limitations of the Model*

When the motor becomes very light, it acts like a rattle; collisions flip its velocity causing it to alternately travel forwards and backwards at a large speed. When this rattling velocity becomes much larger than the particle velocity, the motor very effectively explores its surroundings. However, the model, does not include any data on the surroundings, *i. e.* collisions are sampled with the assumption of molecular chaos. Hence, this model fails when the time scale between collisions, $\tau_c$ exceeds the time scale of particles moving out of the neighbourhood of the motor. The mean free path, $l$, in the neighbourhood of the motor is given by the swimmer area density, $\rho$, assuming a uniform distribution $l = 1/\sqrt{\rho}$. Hence, for the model to be effective $\tau_c > l/v = 1/\sqrt{\rho}v_{\mathcal{T}}$, where $v_{\mathcal{T}}$ is the thermal motor velocity $v_{\mathcal{T}} = \sqrt{\mathcal{T}/m}$. This restricts the maximum density of the gas.

## 5.10 OUTLOOK

The drift for light motors is likely driven by an entropy flow between motor and gas because the largest motor drift occurs for those mass ratios where the temperature difference between gas and motor is smallest. While the drift for massive motors is likely driven by the energy flow due to the constant temperature difference between gas and motor. Hence, motor mass might tune the amount of entropy flow, compared to the energy flow. For this reason, this Brownian-motor model might be a instructive system to analyse from the perspective of stochastic thermodynamics [26, 32, 48, 49, 54].

The unusual behaviour of the motor drift, the motor temperature as well as the breakdown of ergodicity all call for further investigation. Real swimmers do not swim in a vacuum. Therefore, a natural next step would be to include the system of motor and swimmers in a medium of inert particles whose velocity distribution resembles a Gaussian. This might even resolve some of the mathematical difficulties, as the Gaussian medium would "smooth out" the singularities in the transition rates. This modification also vital to making this Brownian-motor model testable in the laboratory.

# Conclusion and Outlook

# 6

## 6.1 conclusion

In kinetic theory it is commonly assumed (under local equilibrium [7]) that particles have Gaussian-distributed velocities. This assumption is not valid for systems far from equilibrium. In the present thesis we addressed the problem of the Brownian motion of an anisotropic particle immersed in such a non-Gaussian gas.

In the present work, we have considered two common examples of a non-Gaussian distribution for gas particles

1. A granular gas [53];

2. A gas made up of swimmers [15]

How does the non-Gaussian velocity distribution of the gas particles effect the motion of this test particle?

Test particles with an asymmetric shape develop a finite steady-state drift when immersed in a gas with an non-Gaussian velocity distribution. Even when collisions between the test particle and the gas particles are elastic, we found that the test particle acquires a non-zero steady-state drift. In this respect it constitutes a Brownian motor.

### *6.1.1 Granular Gas: Slightly Anisotropic Velocity Distribution*

Inspired by the velocity distribution of a dry granular gas [53], which is shaken vertically, we have examined the Brownian motor drift and temperature as a function of shaking strength. The shaking strength translates to the degree of anisotropy of the velocity distribution of the gas.

Previous studies [8] have shown that for an isotropic gas, non-zero stead-state drift can be achieved if collisions between motor and gas are inelastic. Therefore, we compare the effect of anisotropy with the effect of inelasticity.

The temperature of the motor is effected first of all by the dissipation. Anisotropy has only higher order effects on the motor temperature: Even if the motor drift due to an anisotropic gas is comparable to the drift due to inelasticity, the motor's temperature

remains close to the gas temperature in the anisotropic regime. The heat flow, responsible for rectification, therefore is due to an entropy rather than an energy flow.

In the anisotropic regime, the drift *velocity* is of the order of the gas particle velocities. Hence, when the motor/particle mass ratio is increased, the motor's kinetic energy diverges. This is a very dramatic violation of equipartition: In the limit of a massive motor, the kinetic energy of the motor diverges.

### *6.1.2 Swimmers: Strong Deviation from a Gaussian velocity Distribution*

Inspired by dilute gases comprised of swimmers, we examined a gas where all particles have the same speed and random orientation. For such a model, the transition rates of the motor velocity develop rainbow singularities, and the kinetic theory employed for the anisotropic Brownian motor no longer applies.

Rather we study the dynamics by examining the numerical time evolution of the Markov process driving the motor. We have found that for low motor/particle mass-ratio the velocity distributions of the motor become highly non-Gaussian, even containing spikes and cusps that appear to be singularities.

Moreover the drift reverses as a function of mass-ratio. This has been linked to non-trivial velocity correlations. They arise for mass ratios less than 1 where ergodicity breaks down.

The motor temperature also exhibits counter-intuitive behaviour. For massive motors, the motor temperature is approximately a third of the gas temperature, independent of motor mass. In contrast, when the motor/particle mass ratio is low, and drift is large, the motor temperature is close to the temperature of the gas. This leads us to suspect that, for low mass ratio, rectification is driven by an entropy flow similarly to the anisotropic Brownian motor.

## 6.2 DISCUSSION AND OUTLOOK

In the present work we have examined two models for Brownian motors far from equilibrium. Common to both of these models is:

1. In the limit of a massive Brownian motor, the motor acquires a non-zero steady-state drift *velocity*;

2. There is a non-vanishing motor drift, even if the motor temperature is close the the gas temperature.

When the gas particle's velocity distribution is no longer Gaussian, fluctuations in the motor velocity are rectified resulting in finite drift. Our intuition from the second law of thermodynamics

tells us, that a finite steady-state drift occurs when the system is coupled to two baths and there is a heat flow between these two baths.

When collisions between motor and gas are dissipative, the flow of heat takes the form of an energy flow from the bath of thermostatted gas particles into the motor[1]. This manifests itself in the motor's temperature being lower than the gas temperature.

1. The coefficient of restitution introduced in Eq. (2.2b) models the dissipation of kinetic energy into the environment as heat and sound. Here this is the second bath.

However, the investigation of the anisotropic gas in chapter 4 has shown that a small amount of anisotropy can also lead to an equally strong drift. Yet for practical purposes the motor temperature is almost indistinguishable from the gas temperature. Here this heat flow no longer takes the form of an energy flow but rather amounts to an entropy current between the impinging gas particles and the post-collisional particles that have a much more disordered velocity distribution. Maintaining the impinging particles at a fixed distribution therefore requires continuous rearranging of the gas particles. This comes with the cost of entropy.

# Approximating a Distribution from its Moments

Here we shall review how a distribution may be estimated from its moments. For distributions defined on the set of real numbers, this is known as the Hamburger moment problem [36]. We will not address those spaces, where the Hamburger moment problem is not well defined.

Furthermore, the ability to transform moments back to a desired distribution also gives us a systematic way to find the relationship between the motor's moments and the moments of the gas.

## A.1 The Hamburger Moment Problem

The central idea of the Hamburger moment problem, is that we may express an arbitrary probability density function as the product

$$\phi(x) := \hat{\phi}(x)\omega(x) \tag{A.1}$$

of a "weight" function, $\omega(x)$, and a function $\hat{\phi}(x)$ which is to be determined. The weight function is understood as the weight function of the weighted inner product

$$\langle f, g\rangle_\omega := \int_\Omega f(x)g(x)\omega(x)\,\mathrm{d}x \tag{A.2}$$

This inner product implicitly defines a set of orthogonal polynomials[1], $H_n^{(\omega)}(x)$. Assuming that $\hat{\phi}(x)$ is an element[2] of the Hilbert space defined by Eq. (A.2), we may expand $\hat{\phi}(x)$ in terms of this set of orthogonal polynomials

$$\hat{\phi}(x) = \sum_{n=0}^{\infty} h_n^{(\omega)} H_n^{(\omega)}(x) \tag{A.3}$$

where the expansion coefficients, $h_n^{(\omega)}$ are then simply given by the weighted inner product $\langle H_n^{(\omega)}, \hat{\phi}\rangle_\omega$. Since $H_n^{(\omega)}$ is a polynomial of

1. Common choices for $\omega(x)$ is a Gaussian, or an exponential function., corresponding to Hermite or Laguerre polynomials, respectively.

2. When $H_n^{(\omega)}$ are the well known Hermite or Laguerre polynomials, completeness requires that $\hat{\phi} \in L^2(\mathbb{R}, \omega(x)\,\mathrm{d}x$ or $\hat{\phi}) \in L^2((0,\infty), \omega(x)\,\mathrm{d}x)$ respectively.

degree $n$, we may relate the expansion coefficients to the moments of $\phi(x)$

$$h_n^{(\omega)} := \langle H_n^{(\omega)}, \hat{\phi} \rangle_\omega = \langle \sum_k c_{n,k}^{(\omega)} x^k, \hat{\phi} \rangle_\omega = \sum_{k=0}^{n} c_{n,k}^{(\omega)} \langle x^k, \hat{\phi} \rangle_\omega \tag{A.4}$$

By the definition of $\hat{\phi}$, the inner product in the last term simply corresponds to the moments of $\phi$. Hence:

$$h_n^{(\omega)} = \sum_{k=0}^{n} c_{n,k}^{(\omega)} \langle x^k \rangle_\Omega \tag{A.5}$$

Thus, we can now substitute this expression for $h_{n,k}^{(\omega)}$ given by Eq. (A.5) into Eq. (A.3) giving

$$\hat{\phi}(x) = \sum_{n=0}^{\infty} h_n^{(\omega)} H_n^{(\omega)}(x) = \sum_{n=0}^{\infty} \sum_{k=0}^{n} h_n^{(\omega)} c_{n,k}^{(\omega)} x^k =: \sum_{k=0}^{\infty} b_k^{(\omega)} x^k \tag{A.6}$$

with the expansion coefficients $b_k^{(\omega)}$ depending solely on the moments $\langle x^k \rangle$. These expansion coefficients are given by rearranging the terms of the sum and identifying terms with the same power of $x$ yielding

$$b_k^{(\omega)} = \sum_{n=k}^{\infty} h_n^{(\omega)} c_{n,k}^{(\omega)} = \sum_{n=k}^{\infty} c_{n,k}^{(\omega)} \sum_{i=0}^{n} c_{n,i}^{(\omega)} \langle x^i \rangle_\Omega \tag{A.7}$$

This is still not practical for computation as it involves infinite sums. Hence the pragmatic choice would be to truncate Eqs. (A.6) and (A.7) at some finite order.

$$\hat{\phi}_N(x) := \sum_{k=0}^{N} b_k^{(\omega,N)} x^k \tag{A.8a}$$

$$\text{with:} \quad b_k^{(\omega,N)} := \sum_{n=k}^{N} c_{n,k}^{(\omega)} \sum_{i=0}^{n} c_{n,i}^{(\omega)} \langle x^i \rangle_\Omega \tag{A.8b}$$

To demonstrate this, we expand a Gaussian probability density function $P(x) = \exp\left[-(x-3)^2/2\right]/\sqrt{2\pi}$ in terms of Hermite polynomials using Eqs. (A.8) to different orders as is shown in Fig. A.1. The distribution choice of $\omega(x)$ was a *wider* Gaussian than $P(x)$. The reason for this, is that for the choice of $\omega(x) = P(x+3)$, Eqs. (A.8) experience some intermittent oscillations, before converging onto $P(x)$[3]. These oscillations die out readily when choosing a wider $\omega(x)$. In general, we have observed that there is a trade–off in the choice of $\omega(x)$. Choosing $\omega(x)$ *a little* wider than $P(x)$, prevents intermittent oscillations in the convergence of Eqs. (A.8) with respect to $N$. Yet, the closer our choice for $\omega(x)$ is to $P(x)$, the faster the convergence (as long as there are no intermittent oscillations). Hence we point out that even this relatively simple test case has

3. Here we see a typical limitation of numerics. When working analytically, the infinite sum in Eq. (A.6) can be evaluated without the problem of intermittent oscillations.

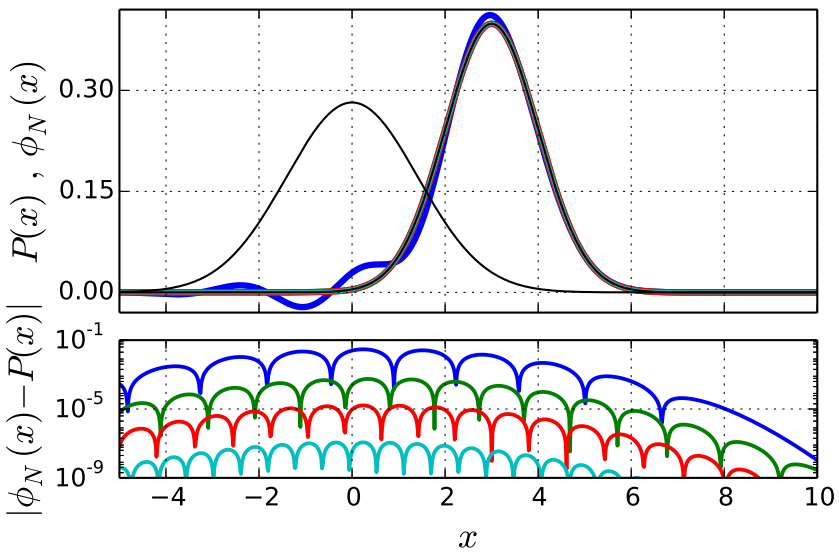


Figure A.1: Example of the expansion algorithm for a Gaussian probability density function $P(x)$. Using a Gaussian weight function, $\omega(x)$ represented by the black curve around the origin, results in a Hermite polynomial expansion, $\phi_N(x)$. $P(x)$ is shown as a thin black curved centred at $x = 3$. The coloured lines represent different truncations for $N = \{10, 20, 30, 60\}$ with steadily decreasing error (bottom panel).

shown that Eqs. (A.8) are not asymptotic expansions, in the sense that higher expansion order leads to better results. We therefore have the need to assess the goodness of our choice for $\omega(x)$. Since in general, only the moments of $\phi(x)$ are known, we at least need a measure which tells us whether observed significant deviations from $\omega(x)$ are *real*, or whether they are simply a result of not taking the expansion to infinity. This we shall do in the next section.

## A.2 COMPLETENESS OF THE MOMENT EXPANSION

Many orthogonal polynomials may be expressed in terms of a Rodrigues' formula.

$$H_n(x) = \frac{1}{\omega(x)} \partial_x^n \left[\omega(x) P_n(x)\right] \tag{A.9}$$

where $P_n(x)$ is a Polynomial. In general, Eq. (A.9) is only a polynomial, if $\partial_x^n[\omega(x)]/\omega(x)$ is a polynomial for all $n$. Never the less, we shall restrict ourselves to orthogonal polynomials which have a Rodrigues–type representation. This has the advantage of making the proof of completeness almost trivial[4].

We shall determine the conditions $\omega(x)$ has to fulfil, in order to be able to perform the expansion Eq. (A.3). For this we may use the following very useful theorem:

**Definition 20** Let $(\Omega, \Sigma, x)$ be a measure space, and $F(\Omega)$ be the set of all measurable functions from $\Omega$ to $\mathbb{R}$.

4. As we will see later, this form has the added advantage, that distributions with tails wider than $\omega(x)$ will not be contained in the Hilbert space of spanned by Eq. (A.9)

**Theorem 1** *The set*

$$L^p(\Omega) := \left\{ f(x) \in F(\Omega) \mid \int_\Omega |f(x)|^p \, \mathrm{d}x < \infty \right\} \tag{A.10}$$

*forms a complete metric space under the metric induced by the norm*

$$\|f\|_p := \left( \int_\Omega |f(x)|^p \, \mathrm{d}x \right)^{\frac{1}{p}} \tag{A.11}$$

In other words, the spaces of $p$–Integrable functions form a complete metric space. Consequentially every function $f$, such that $\|f\|_p < \infty$, may be written as the limit of a sequence of functions $f_n \in L^p(\Omega)$.

With the help of this theorem, completeness is almost trivial to proof.

**Lemma 2** *Say $\omega(x)$ is chosen, such that the polynomials, $H_n(x)$ are orthonormal with respect to the inner product $\langle \bullet, \bullet \rangle_\omega$ (see Eq. (A.2)). Then the set of these polynomials form a complete basis of*

$$L^2(\Omega, \omega(x)\mathrm{d}x) := \left\{ f(x) \in F(\Omega) \,\middle|\, \int_\Omega |f(x)|^2 \, \omega(x) \, \mathrm{d}x < \infty \right\} . \tag{A.12}$$

Proof For each $H_n$, we introduce the function

$$f_n(x) := H_n(x) \sqrt{\omega(x)} \, . \tag{A.13}$$

The $L^2$–norm induces an inner product $\|f\|_2^2 =: \langle f, f \rangle$. We see that $\langle f_n, f_m \rangle = \langle H_n, H_m \rangle_\omega$. Hence the orthogonality of the polynomials $H_n$ is carried over to the induced metric, induced by the $L^2$–norm. Since the $f_n$ are orthonormal, they form a complete (see Theorem 1) orthonormal basis of $L^2(\Omega)$. Hence the $H_n$ also form a complete orthonormal basis of $L^2(\Omega, \omega(x)\mathrm{d}x)$.

In other words, only $\hat{\phi} \in L^2(\Omega, \omega(x)\mathrm{d}x)$ can be expanded in terms of these polynomials.

The condition that $\|\hat{\phi}\sqrt{\omega}\|_2^2 = \langle f, f \rangle_\omega < \infty$ gives a useful test for the convergence of Eq. (A.6). Say we wish to expand the distribution $\rho(x)$ in terms of Eq. (A.6), that is to say, we only have the moments of $\rho(x)$, and we wish to accurately determine the distribution.

Say an expansion for $\hat{\phi}$ exists in terms of Eq. (A.6). Then

$$\infty > \left\langle \hat{\phi}, \hat{\phi} \right\rangle_\omega = \sum_{k=0}^{\infty} b_k^{(\omega)} \left\langle x^k, \hat{\phi} \right\rangle_\omega = \sum_{k=0}^{\infty} b_k^{(\omega)} \langle x^k \rangle_\Omega \tag{A.14}$$

And so we may arbitrarily choose[5] a given $\omega(x)$, and compute Eq. (A.8b) for some N. Then we may check that the series

$$\sum_{k=0}^{N} b_k^{(\omega,N)} \langle x^k \rangle_\Omega \tag{A.15}$$

is convergent for $N \to \infty$. Hence we can utilize the standard tests for convergence of series to estimate the quality of the moment expansion. In particular, we shall utilize the ratio test and the root test.

**Definition 21** Let $\sum_n c_n$ be a series where the $c_n \in \mathbb{R}$. We may define two limits:

$$r_{\mathrm{R}} = \lim_{n\to\infty} \frac{c_{n+1}}{c_n} \tag{A.16a}$$

and

$$r_{\mathrm{P}} = \lim_{n\to\infty} \sqrt[n]{|c_n|} \tag{A.16b}$$

**Theorem 2 (Ratio Test)** *Let the limit $r_{\mathrm{R}}$ exist. If $r_{\mathrm{R}} < 1$ the series is convergent. If $r_{\mathrm{R}} = 1$, the test is inconclusive. Otherwise the series is divergent.*

**Theorem 3 (Root Test)** *Let the limit $r_{\mathrm{P}}$ exist. If $r_{\mathrm{P}} < 1$ the series is convergent. If $r_{\mathrm{P}} = 1$, the test is inconclusive. Otherwise the series is divergent.*

**Remark 6** When only numerical data are available, it can be difficult to see whether $r_\bullet$ approaches a value less than one or not. A common solution is to plot Domb-Sykes plots of the series terms. That is, plotting either $c_n/c_{n+1}$ or $1/\sqrt[n]{|c_n|}$ against $1/n$. This makes extrapolation to large $n$ significantly easier, where the $y$–intercept gives $1/r_\bullet$.

### *A.2.1 Motivating Example*

However the limit $r_{\mathrm{P}}$ seems to exist. The Domb-Sykes plot for $r_{\mathrm{P}}$ is shown in Fig. A.3.

To illustrate that the convergence of Eq. (A.15) can be read of the Domb-Sykes plot for $c_n := b_n^{(\omega,N)} \langle x^n \rangle_\Omega$, we apply it to the expansion shown in Fig. A.1. We find that the limit $r_{\mathrm{R}}$ does not exist (the terms $c_n$ show rapid oscillations as shown by Fig. A.2).

The exploration of the Domb-Sykes plot Fig. A.3 also show an unusual behaviour of the limit $n \to \infty$: $|c_n|^{-1/n}$ approaches infinity *before* $n$ has approached infinity. In fact, for an expansion up to 60 moments, $|c_n|^{-1/n} \to \infty$ as $1/n \to 0.014$ (approximately). Furthermore, this finite value decreases with increasing expansion order. We therefore come to the conclusion that the finite–$n$ divergence is a result of letting $c_n = b_n^{(\omega,N)} \langle x^n \rangle_\Omega$ rather than $c_n = b_n^{(\omega)} \langle x^n \rangle_\Omega$,

5. In general, choosing a Gaussian for $\omega(x)$ is a good initial choice. Choosing an exponential requires knowledge of the moments defined on $\mathbb{R}^{\pm}$.

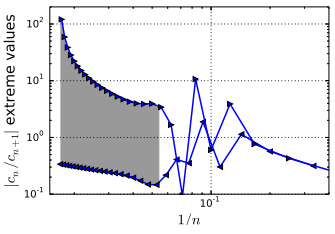


Figure A.2: Limiting behaviour of the ratio function for the expansions shown in Fig. A.1. The shaded area marks rapid oscillations.

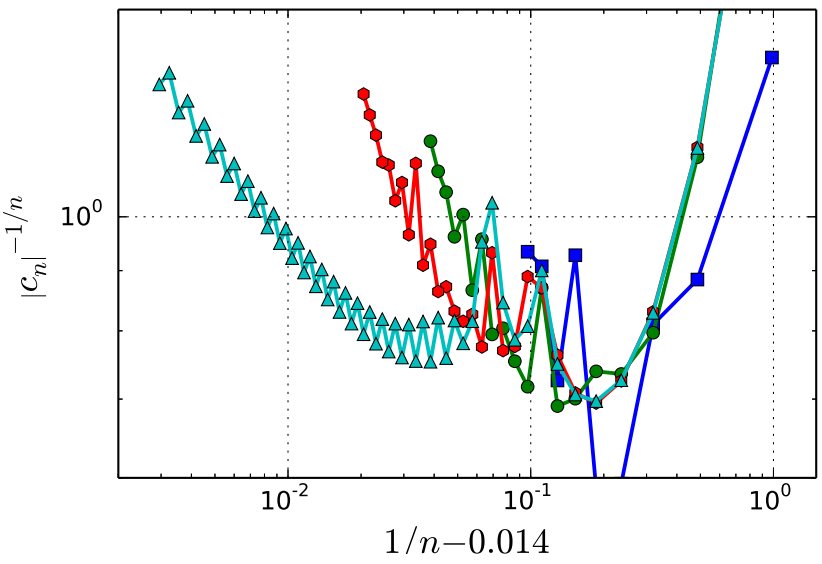


Figure A.3: Domb-Sykes plot, where $c_n := \left|b_n^{(\omega,N)} \langle x^n \rangle_\Omega\right|^{-1/n}$, for the expansion shown in Fig. A.1. The colours correspond to those used in Fig. A.1. The plot gives evidence that $r_\mathrm{P} < 1$ is likely.

*i. e.* it is due to the error of estimating $b_n^{(\omega)}$ from only finitely many moments.

This might seem a little precarious, however Fig. A.3 has established two important things:

*Eventual monotonicity*: To a high likelihood, the sequence $\{|c_n|^{-1/n}\}$ becomes monotonically rising (up to small oscillations which eventually die out).

*Eventual small* $r_\mathrm{P}$: $\exists N < \infty$ such that $|c_n|^{-1/n} < 1 \quad \forall n > N$.

Hence, the limit $r_\mathrm{P}$ likely exists and, if it does, it is likely to be less than 1.

To better understand the subtle usage of this test (and of the importance of choosing a good $\sigma$), we shall examine the case where $P(x)$ is expanded with a basis for which *sigma* is too small. The resulting estimate for $\phi_N(x)$ is shown in Fig. A.4.

Here we chose a value of $\sigma$ which formally still results in a convergent moment expansion. However, we are close to the theoretical limit (as we shall see in the next section). The expansion undergoes transient oscillations (green line) which die out once enough moments are used. These oscillations seem to occur where $P(x)$ disagrees most with $\omega(x)$.

The Domb-Sykes plot (Fig. A.4, left panel) shows that convergent behaviour alone is *not enough*! Both the blue and the green lines seem to converge onto $r_\mathrm{P} = 0$, with the green line converging fastest. Yet this latter case is clearly not a good expansion.

We see that the rate of convergence is not a good indicator that the limit $r_\bullet < 1$, if it exists. We must keep in mind that the Domb-Sykes plot is not so much *proof* of convergence, let alone a

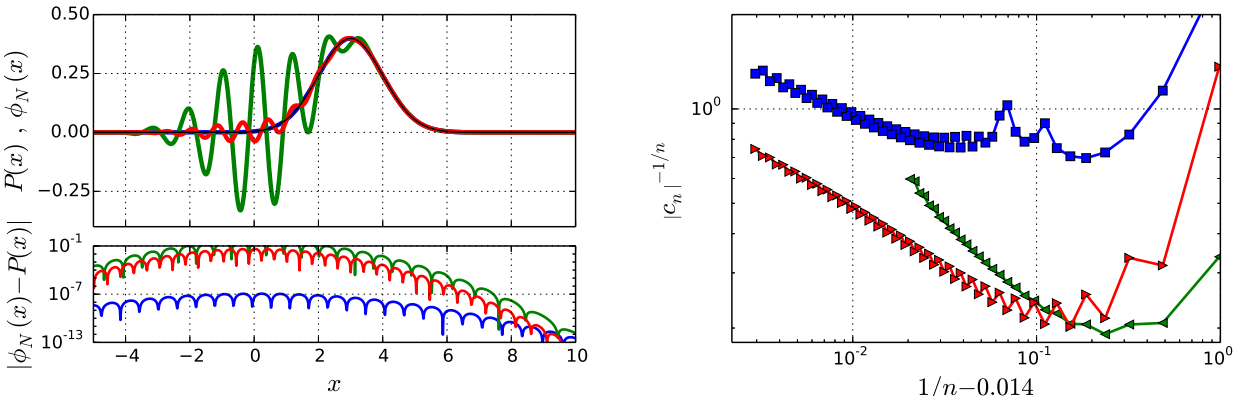


Figure A.4: Here we see an example of the intermittend breakdown: The green line reconstructs the distribution with the using the fewest moments. As we increase the number of moments considered we gradually converge onto the actual distribution.

tool accurately calculating the value of a limit. Yet it gives evidence (with varying degrees of confidence) that a series converges to a given limit.

Hence the Domb-Sykes plot gives a measure of the *quality* of the expansion. The following criteria seem reasonable for a high-quality expansion (Eq. (A.8)):

*Necessarily*: The Domb-Sykes plot needs to converge and become monotonic for low $x$-values.

*Quality*: The $y$ value at the lowest $x$ value characterizes the quality of the expansion.

Thus we shall only trust all the features of a distribution reconstructed from its moments, if the Domb-Sykes plot appears to readily converge to a value of $r_\bullet < 1$, and the $y$–value for lowest $x$–value is greater than 1.

## A.3 WEIGHT FUNCTION

For the scope of this work, we restrict our choices for $\omega(x)$ to either exponentials or Gaussians. The basis of orthonormal polynomials with respect to this class of inner products are the Laguerre polynomials for $\omega(x) = \exp[-x/\sigma]/2\sigma$, and the Hermite polynomials for $\omega(x) = \exp[-x^2/2\sigma]/\sqrt{2\pi\sigma}$. The weight function for Laguerre or Hermite polynomials can be indexed by an integer $p$ such that $\omega_p(x) \sim \exp[-x^p/p\sigma]$.

We will show in the subsequent sections, that these bases are sufficient for expanding distributions with exponential and Gaussian tails, respectively.

It is important to note, that the domain over which the polynomials are orthogonal (i.e. the domain of the inner product Eq. (A.2))

is implied by the finiteness of the weighted $L^2$–norm, $L^2(\Omega, \omega(x)\mathrm{d}x)$. This mean that the weighted norm $\| \bullet \|_{L^2(\Omega,\omega(x)\mathrm{d}x)}$ admits $\Omega = \mathbb{R}$ for Gaussian $\omega$. Yet for exponential $\omega$ and $\Omega = \mathbb{R}$, $\| \bullet \|_{L^2(\Omega,\omega(x)\mathrm{d}x)}$ is finite for no polynomials, except 0. Restricting $\Omega$ to the positive real line, that is $\Omega = \mathbb{R}^+$ is sufficient.

Hence the Laguerre-polynomial expansion is only defined for distributions over $\mathbb{R}^+$. There is a way around this though, by expanding $\hat{\phi}_+(x) := [\![x]\!]\hat{\phi}(x)$, and $\hat{\phi}_-(x) := [\![-x]\!]\hat{\phi}(x)$, that is the positive and negative part of $\hat{\phi}$ separately. Were each separate expansion follows the same algorithm as described in the previous section, yet involving the partial moments $\langle x^k \rangle_{\mathbb{R}^\pm}$.

### *A.3.1 Completeness given the Tails of the Distribution*

Let $\phi(x)$ be a distribution such that

$$\phi(x) \asymp \mathrm{e}^{-\frac{x^\alpha}{\alpha\delta}} \,. \tag{A.17}$$

In order to expand $\phi(x)$ in terms of

$$\omega(x) \asymp \mathrm{e}^{-\frac{x^p}{p\sigma}} \,, \tag{A.18}$$

then we wish to expand

$$\hat{\phi}(x) \asymp \mathrm{e}^{-\frac{x^\alpha}{\alpha\delta}+\frac{x^p}{p\sigma}} \tag{A.19}$$

in terms of Laguerre polynomials ($p = 1$), or Hermite polynomials ($p = 2$). The completeness of the weighted $L^2$–space requires that

$$\|\hat{\phi}\|_{L^2(\Omega_p,\omega_p(x)\mathrm{d}x)} \asymp \int_{\Omega_p} \mathrm{e}^{-2\left(\frac{x^\alpha}{\alpha\delta}-\frac{x^p}{p\sigma}\right)}\omega_p(x)\mathrm{d}x < \infty \tag{A.20}$$

where $\Omega_1 = \mathbb{R}^+$ and $\Omega_2 = \mathbb{R}$. It follows that whether or not $\hat{\phi}$ is in the appropriate $L^2$–space comes down to the convergence of the integral

$$\int_{\Omega_p} \mathrm{e}^{-2\left(\frac{x^\alpha}{\alpha\delta}-\frac{x^p}{p\sigma}\right)-\frac{x^p}{p\sigma}}\mathrm{d}x \tag{A.21}$$

Given

$$L := \frac{x^p}{p\sigma} - 2\frac{x^\alpha}{\alpha\delta} \asymp \begin{cases} \frac{1}{p\sigma}\, x^p & \text{if } p > \alpha \\ -\frac{2}{\alpha\delta}\, x^\alpha & \text{if } \alpha > p \\ \left(\frac{1}{p\sigma} - \frac{2}{\alpha\delta}\right) x^\alpha & \text{if } \alpha = p \end{cases} \tag{A.22}$$

the convergence of Eq. (A.21) is determined by the asymptotics of $L$. The integral[6]

$$\int_{\mathbb{R}^+} \mathrm{e}^{-\beta x^\lambda} = \begin{cases} \beta^{-1/\lambda}\Gamma\left[1+\frac{1}{\lambda}\right] & \text{if } \beta > 0 \\ \infty & \text{otherwise} \end{cases} \tag{A.23}$$

together with the asymptotics of $L$ allows us to reduce the convergence conditions of Eq. (A.21) to the following three cases:

6. where $\Gamma[\bullet]$ is the gamma function

$p > \alpha$: Eq. (A.21) diverges.

$\alpha > p$: Eq. (A.21) converges. For small $\lambda$, it's of the order of $\Gamma[\lambda^{-1}]$.

$\alpha = p$: Eq. (A.21) converges if only if $1/p\sigma - 2/\alpha\delta < 0$.

Hence we see that the tails of $\omega(x)$ need to be wider than the tails of $\phi(x)$. Consequently, distributions with Gaussian tails can be expanded by any exponential $\omega(x)$. $\phi(x)$ with tails wider than Gaussians, cannot be expanded in terms of Gaussian $\omega(x)$. When the tails of $\omega(x)$ and $\phi(x)$ are alike, $\sigma > \delta/2$. All in all, we see that the class of Laguerre polynomials is by far more general than the Hermite polynomials. They allow broader distributions to be expanded compared to Hermite polynomials, which cannot expand exponential distributions.

## A.4 GRAM–CHARLIER EXPANSION

Eq. (A.6) is also frequently called the Gram-Charlier expansion. It is important to note, that the integral domain, $\Omega$ in Eq. (A.2) is dependent on the choice of $\omega(x)$. Likewise the coefficients of the moment expansion Eq. (A.7) either take the generic moments, or the one-sided moments.

Hence, if we desired to expand $\hat{\phi}$ in terms of Laguerre Polynomials (this would be necessary, if the system we are describing has exponential tails), then the left-hand ($\langle\bullet\rangle_{\mathbb{R}^-}$) and the right-hand ($\langle\bullet\rangle_{\mathbb{R}^+}$) partial moments need to be treated separately to give the negative and positive part of $\phi$.

The versatility of the Laguerre polynomial expansion is demonstrated in Fig. A.5. The $\chi^2$ distribution could be accurately reconstructed from its moments. This would have not been possible using Hermite polynomials (as the $\chi^2$ distribution has exponential tails). Furthermore, a Gaussian distribution could also be accurately reconstructed. The convergence behaviour as demonstrated by the ratio test is shown in Fig. A.6. We see that the convergence of the Laguerre polynomial expansion for the Gaussian distribution seems much better than that of the Hermite polynomial expansion.

This represents a mathematical trade-off, the standard Gram-Charlier expansion, relying on expanding $\hat{\phi}$ in terms of Hermite polynomials, requires only the standard moment hierarchy (Eq. (3.34b) to be solved. Of course, then the tails of $\phi$ must not diverge from a Gaussian distribution too much. On the other hand, expanding $\hat{\phi}$ in terms of Laguerre polynomials, allows a greater range of distribution. This, however, requires the partial-moments, which cannot be determined using the moment-hierarchy method alone

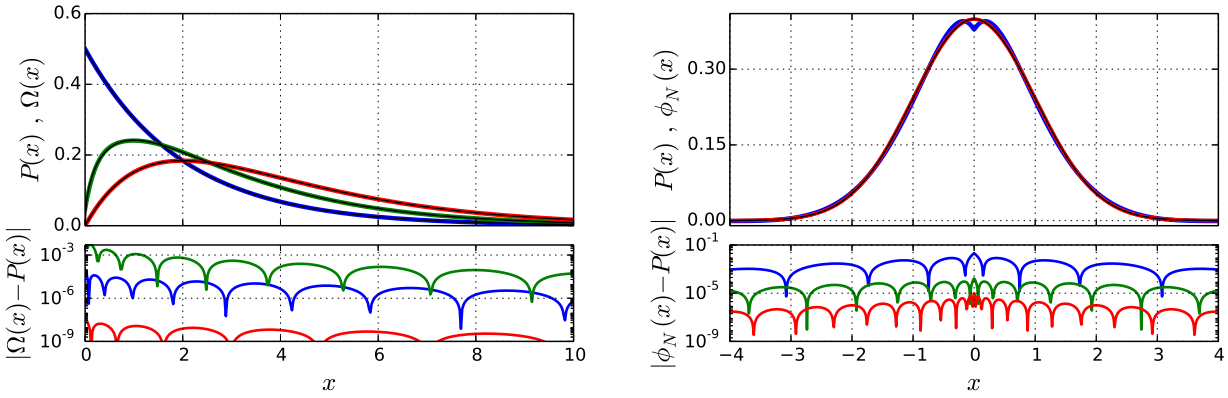


Figure A.5: *Left panel:* Here we have reconstructed several $\chi^2$ distributions from the partial moments. *Right panel:* Here we have used the partial moments to reconstruct a Gaussian distribution.

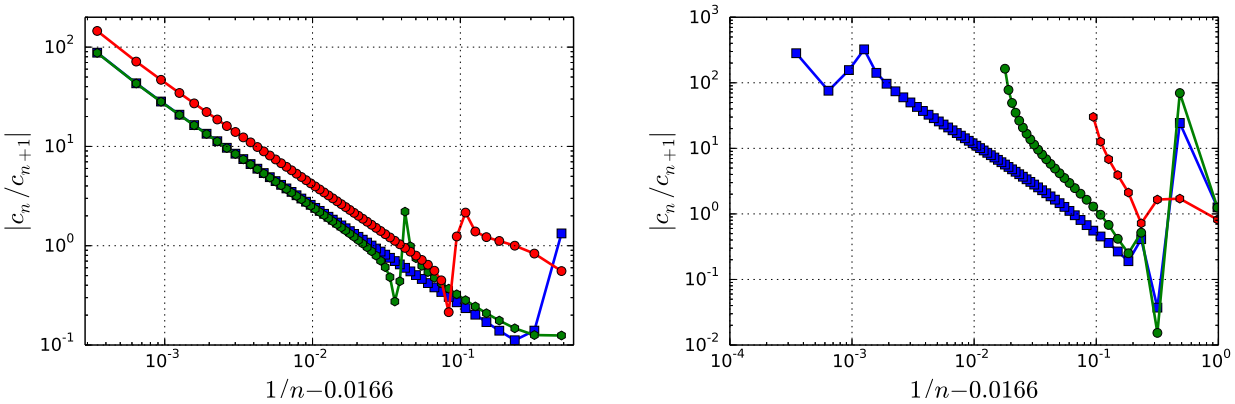


Figure A.6: Ratio tests for the Gram–Charlier Expansions in Fig. A.5. Colours are in correspondence to the curves in Fig. A.5.*Left panel:* $\chi^2$ distribution. *Right panel:* Gaussian distribution.

# Published Work

B

This appendix is an overview of the works published during the course of the PhD-programme.

## B.1 Role of granular gas anisotropy

This work is the published components of chapter 4. Here we discuss the influence on of an anisotropic velocity distribution on the drift and temperature of a granular Brownian motor.

## B.2 Arrest of the flow of wet granular matter

Not all granular gasses are non-cohesive. Here we examine granular matter that is cohesive by forming capillary bridges. For the purposes of this study, a capillary bridge is modelled as an attractive potential between two grains. This potential is formed only when grains initially collide. If they move apart with enough energy, the bridge is "broken" and its potential energy is dissipated. This is often called *wet* granular matter [27].

Similarly to the dry granular gas examined in chapter 4, energy needs to be injected into the wet granular flow[1] in order to prevent all motion from ceasing due to dissipation. In our paper we examine the minimal external forcing necessary to keep the granular flow in motion by an external body force.

1. For reasonable external forcing, wet granular matter resembles a fluid rather than a gas. So we shall call this a granular flow

## B.3 The statistics of droplet distributions on 2-dimensional substrates

The size distribution of droplets as they are nucleated on a 2-dimensional surface results from their interactions in a non-trivial way. A common technique, to problems which span many scales is scaling theory. We show here, that the traditional scaling theory

needs to be augmented by terms accounting different regimes for small and medium sized droplets.

PHYSICAL REVIEW E **87**, 040201(R) (2013)

# Granular Brownian motors: Role of gas anisotropy and inelasticity

Johannes Blaschke and Jürgen Vollmer
*Max Planck Institute for Dynamics and Self-Organization (MPI DS), 37077 Göttingen, Germany and*
*Faculty of Physics, Georg-August-University Göttingen, 37077 Göttingen, Germany*
(Received 13 February 2013; published 3 April 2013)

We investigate the motion of a two-dimensional wedge-shaped object (a granular Brownian motor), which is restricted to move along the $x$ axis and cannot rotate as gas particles collide with it. We show that its steady-state drift, resulting from inelastic gas-motor collisions, is dramatically affected by anisotropy in the velocity distribution of the gas. We identify the dimensionless parameter providing the dependence of this drift on shape, masses, inelasticity, and anisotropy: The anisotropy leads to dramatically enhanced drift of the motor, which should easily be visible in experimental realizations.

DOI: 10.1103/PhysRevE.87.040201 PACS number(s): 45.70.−n, 05.20.Dd, 02.50.−r, 05.40.−a

## I. INTRODUCTION

We investigate the motion of a two-dimensional wedge-shaped object, which we shall refer to as the motor (Fig. 1). It cannot rotate and is restricted to move along the $x$ axis as gas particles collide with it. When the motor experiences elastic collisions, there is a finite transient drift as the motor approaches thermal equilibrium with the gas [1]. A finite steady-state motion is achieved when the gas-motor collisions are inelastic [2–6]. The latter systems have consequently been called granular Brownian motors.

These motors are prototypes of systems where small particles collide with heavy objects that break reflection symmetry. Such models have been used to explore the rectification of thermal fluctuations [6–8], the adiabatic piston [9,10], and have lead to a novel treatment of nonequilibrium steady states [11]. In an experimental realization [4], it was demonstrated that they even obey nonequilibrium fluctuation theorems.

So far, however, all pertinent theoretical studies have been based on thermostated gases such that impacting particles are sampled from a Maxwellian velocity distribution. When thermostating via stochastic forcing, this is a reasonable assumption [3]. In contrast, experimental realizations of granular gases typically exhibit sustained heterogeneities in density and granular temperature [12–16]. Moreover, when shaking in the plane of observation, they exhibit noticeable anisotropy of the granular temperature [17]. Consequentially, we refer to them as anisotropic gases.

Here we revisit the approach by which [2,7,8] derived the theory for the isotropic case. Then we address the motion of the motor driven by an anisotropic gas.

## II. GAS VELOCITY DISTRIBUTION FUNCTION

Following [17], we model an anisotropic velocity distribution function (VDF) using a squeezed Gaussian

$$\phi(\hat{v}_x,\hat{v}_y) = \frac{m}{2\pi kT}\exp\left[-\frac{m}{2}\left(\frac{\hat{v}_x^2}{kT_x}+\frac{\hat{v}_y^2}{kT_y}\right)\right],$$

where $m$ is the particle mass, $k$ is Boltzmann's constant, $T \equiv \langle m(\hat{v}_x^2+\hat{v}_y^2)\rangle_\phi/2k$ is the gas temperature averaged over both degrees of freedom, and $T_x$ and $T_y$ are the granular temperatures in the $\hat{x}$ and $\hat{y}$ directions, respectively.

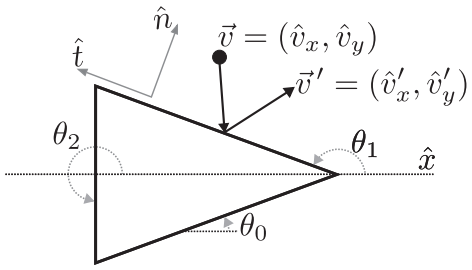


FIG. 1. A particle (black circle) colliding with the Brownian motor (triangular wedge with wedge angle $2\theta_0$). The angles of the edges $i \in \{0,1,2\}$ are measured counterclockwise from the positive $x$ axis to the outside of the motor, yielding $\theta_0$, $\theta_1 = \pi - \theta_0$, and $\theta_2 = 3\pi/2$, respectively.

Anisotropy is quantified via the squeezing parameter $\alpha^2 := T_y/T_x$. Here $\alpha \geqslant 1$ as we only address vertical shaking. Introducing dimensionless velocities $v := \hat{v}/\sqrt{2kT/m}$ and requiring $\phi(\hat{v}_x,\hat{v}_y)\,d\hat{v}_x\,d\hat{v}_y = \phi_\alpha(v_x,v_y)\,dv_x\,dv_y$ reduces the VDF to

$$\phi_\alpha(v_x,v_y) = \frac{2}{\pi}\frac{\alpha^2+1}{\alpha}\exp\left[-(\alpha^2+1)v_x^2-\left(\frac{1}{\alpha^2}+1\right)v_y^2\right], \tag{1}$$

which depends on $\alpha$ only and not on $m$, $k$, $T_x$, and $T_y$.

## III. GAS-PARTICLE INTERACTION

A collision event is illustrated in Fig. 1. The motor has dimensionless velocity $\vec{V} = V\hat{e}_x$ and a mass $M$. Collision rules depend on which side of the motor, $i \in \{0,1,2\}$, is being impacted and on the coefficient of restitution $r$.

Assuming no change in the tangential component of the gas particles velocity,

$$\vec{v}' \cdot \hat{t}_i = \vec{v} \cdot \hat{t}_i, \tag{2a}$$

where $\hat{t}_i = (\cos\theta_i, \sin\theta_i)$ is the vector tangential to the surface being impacted. In contrast, due to restitution, the reflection law for the normal direction becomes

$$(\vec{V}' - \vec{v}') \cdot \hat{n}_i = -r(\vec{V} - \vec{v}) \cdot \hat{n}_i, \tag{2b}$$

 

where $\hat{n}_i = (\sin\theta_i, -\cos\theta_i)$ is the normal vector. Single collisions obey conservation of momentum

$$v_x' + \mathcal{M}V' = v_x + \mathcal{M}V, \tag{2c}$$

where $\mathcal{M} := M/m$ is the mass ratio. Together Eqs. (2) determine the change in the motor velocity

$$u_i := V' - V = \gamma_i(v_x - V - v_y \cot\theta_i), \tag{3a}$$

where

$$\gamma_i \equiv \gamma(r,\mathcal{M},\theta_i) := (1+r)\frac{\sin^2\theta_i}{\mathcal{M}+\sin^2\theta_i}. \tag{3b}$$

## IV. TIME EVOLUTION OF THE MOTOR VDF

For independent collisions, the probability density $P_t(V)$ of finding a motor with velocity $V$ at time $t$ follows the master equation

$$\partial_t P_t(V) = \int_{\mathbb{R}} W(V-u;u)P_t(V-u)\,du - \int_{\mathbb{R}} W(V;-u)P_t(V)\,du, \tag{4}$$

where $W(V;u)\,du$ is the conditional probability of a motor experiencing a collision resulting in a velocity change $V \to V+u$. It can be expressed as an integral involving four specifications: selecting only those outcomes that (i) are commensurate with single collisions [Eqs. (3)] and (ii) collide with the outside of the motor's surface, (iii) weight single-particle collisions by the impact frequency, where the collision frequency for a stationary motor is used to nondimensionalize time, and (iv) sample over all possible impact speeds and the motor's sides, where $w_i(\theta_0)$ is the probability of picking the side $i$ [2]:

$$W(V;u) = \sum_{i\in\{0,1,2\}} \int_{\mathbb{R}}\int_{\mathbb{R}} \underbrace{\delta[u-\gamma(r,\mathcal{M},\theta_i)(v_x - V - v_y\cot\theta_i)]}_{\text{(i)}} \times \underbrace{\Theta[(\vec{V}-\vec{v})\cdot\hat{n}_i]}_{\text{(ii)}} \underbrace{(\vec{V}-\vec{v})\cdot\hat{n}_i}_{\text{(iii)}} \times \underbrace{\phi_\alpha(v_x,v_y)\,dv_x\,dv_y\,w_i(\theta_0)}_{\text{(iv)}}. \tag{5}$$

Consequentially, the steady-state solutions of Eq. (4) are selected by $\alpha$, $\gamma(r,\mathcal{M},\theta)$, and the wedge angle $2\theta_0$.

## V. SOLUTIONS TO THE MASTER EQUATION USING MOMENT HIERARCHIES

Given that $\forall n \in \mathbb{N}^+$ and $m \leqslant n$ the derivatives $\partial_u^m[u^n W(V;u)]$ vanish for $u \to \pm\infty$, the Kramers-Moyal [18] expansion can be applied to the moments $M_k(t) := \langle V^k\rangle = \int_{\mathbb{R}} V^k P(V,t)\,dV$. Together with the jump moments $a_n(V) := \int_{\mathbb{R}} u^n W(V;u)\,du$, we arrive at an evolution equation for the moments

$$\partial_t M_k(t) = \sum_{n=1}^{k}\binom{k}{n}\langle V^{k-n}a_n(V)\rangle. \tag{6}$$

In order to accommodate a more general velocity distribution, we compute the jump moments by expanding them as a power series

$$a_n(V) = \sum_{i=0}^{\infty} d_{n,i}V^i \tag{7}$$

such that Eq. (6) reduces to an infinite linear system

$$\partial_t M_k(t) = \sum_{l=0}^{\infty} A_{k,l}M_l \tag{8}$$

reminiscent of a matrix equation with matrix elements

$$A_{k,l} := \sum_{j=0}^{\min\{l,k-1\}}\binom{k}{k-j}d_{k-j,l-j}. \tag{9}$$

## VI. TIME-RESOLVED MOTOR VDF

In general, one still cannot solve the infinite matrix equation (8). Hence we truncate Eq. (7) at order $N$, which leads to

$$\partial_t M_k(t) = \sum_{l=0}^{N} A_{k,l}M_l. \tag{10}$$

The expansion coefficients $d_{n,i}$ in Eq. (7) are computed using the Taylor expansion coefficients $d_{n,i} = \frac{1}{n!}a_n^{(i)}(0)$, where $a_n^{(i)}(V)$ is the $i$th derivative of the $n$th jump moment. In order to compute these derivatives, the $\delta$ distribution in Eq. (5) is integrated out, resulting in nontrivial integrals. As long as $V = 0$, these can be evaluated using MATHEMATICA. The higher-order derivatives of these integrals are related to each other, allowing them to be computed recursively. This provides an analytical, albeit tedious, expression for Eq. (10).

Asymptotic analysis reveals that $d_{n,i} \sim -i^{-i/2}$ for large $i$, resulting in a combined truncation error in Eq. (10) of the order of $10^{-10}$ for $N = 20$. In this work we hence solve Eq. (10) for $N = 20$ and a wedge angle $\theta_0 = \pi/4$ unless stated otherwise. The initial condition will always be an ensemble where all the motors are at rest: $\vec{M}(0) = (1,0,0,\ldots)$.

Figure 2 illustrates typical time dependences of the motor drift $\langle V\rangle$ and motor temperature $\mathcal{T} := \mathcal{M}(\langle V^2\rangle - \langle V\rangle^2)$. (i) For elastic collisions and an isotropic gas, the ensemble undergoes a finite transient drift while it heats up to the temperature of the gas [1]. Subsequently, the drift ceases. (ii) When introducing inelastic gas-motor collisions, the steady state acquires a finite drift velocity and a temperature significantly lower than the gas [2]. (iii) Here we note that a small amount of squeezing $\alpha = 1.02$ causes a drift similar to the drift in a system with strongly inelastic collisions. Note that this squeezing hardly affects the temperature.

In the subsequent sections, we examine the parameter dependence of the steady-state drift $\langle V\rangle$ and motor temperature $\mathcal{T}$, respectively.

## VII. MOTOR DRIFT

The inset in Fig. 3(a) shows that for a fixed coefficient of restitution ($r = 0.3$), the drift velocity initially scales as $1/\mathcal{M}$. For large $\mathcal{M}$ and $\alpha \neq 1$ it approaches a constant value depending only on $\alpha$ and $\theta_0$. The $1/\mathcal{M}$ scaling is in agreement

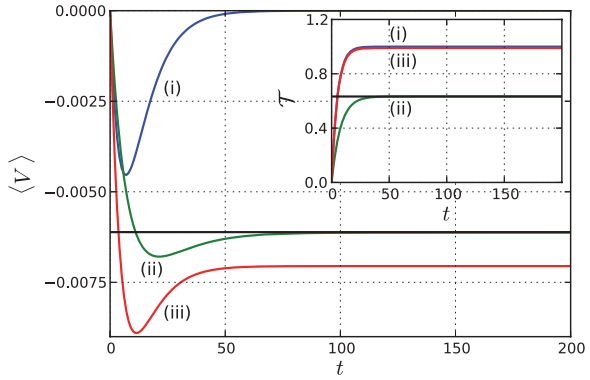


FIG. 2. (Color online) Ensemble drift $\langle V\rangle$ (main panel) and temperature $\mathcal{T}$ (inset) against $t$ for motors with mass ratio $\mathcal{M}=10$ and $\theta_0=\pi/4$. Blue lines (i) denote $r=1$ and $\alpha=1$, elastic collisions with an isotropic gas. Green lines (ii) denote $r=0.3$ and $\alpha=1$, strongly inelastic collisions with an isotropic gas. The motor relaxes to the values predicted by [2] (black horizontal lines). Red lines (iii) denote $r=1.0$ and $\alpha=1.02$, elastic collisions with a slightly anisotropic gas.

with the theory for the isotropic gas [2]. We conclude that the drift for light motors is affected primarily by the inelastic nature of the gas-motor interactions. Here the theory for the isotropic gas is a good approximation. In contrast, massive motors are more strongly influenced by the anisotropy of the gas, no matter how slight this may be.

In order to fully characterize this crossover, we consider the limit of a massive motor $\mathcal{M}\to\infty$. In this limit the $\gamma_i$ term in Eq. (3a) simplifies to

$$\gamma(r,\mathcal{M},\theta)\simeq\frac{1+r}{\mathcal{M}}\sin^2\theta=:\Gamma\sin^2\theta. \tag{11}$$

Due to this factorization of $\sin\theta$ and $\Gamma$, massive motors undergoing dissipative collisions ($r<1$) behave like motors undergoing elastic collisions ($r=1$) yet with a slightly higher mass. This is in agreement with results for the granular Boltzmann equation [19,20]. Consequentially, the limit of a massive motor corresponds to the limit $\Gamma\to 0^+$ and is independent of restitution, $r$.

We observe that, for small $\Gamma$,

$$d_{n,i}\sim\Gamma^n, \tag{12a}$$
$$d_{1,0}\sim(\alpha-1)\Gamma. \tag{12b}$$

Hence, for isotropic gas VDFs (where $\alpha=1$), the matrix defined by Eq. (9) becomes upper triangular in leading order of $\Gamma$. This corresponds to the decoupling of the time-evolution equations for the moments, as observed in [2]. In contrast, for $\alpha>1$, the time-evolution equations for the moments become coupled again:

$$A\simeq\begin{pmatrix}0&0&0&\cdots\\ d_{1,0}&d_{1,1}&d_{1,2}&\cdots\\ 0&2d_{1,0}&2d_{1,1}&\cdots\\ \vdots&\vdots&\vdots&\ddots\end{pmatrix}. \tag{13}$$

This shall be the starting point of a perturbation theory around $(\Gamma,\alpha)=(0^+,1)$. We assume that, in the limit $\Gamma\to 0^+$, the steady state is still largely independent of truncation size for small $\alpha-1$. Hence we find that the null space of the upper left $2\times 2$ submatrix of Eq. (13) accurately determines the steady-state drift due to anisotropy,

$$\langle V\rangle_{\rm ani}\simeq-\frac{d_{1,0}}{d_{1,1}}\simeq\sqrt{\frac{\pi}{2}}(\sin\theta_0-1)(\alpha-1). \tag{14}$$

Note that Eq. (14) does not depend on $\mathcal{M}$. This is quite astounding since it implies that the drift velocity of the massive motor is of the order of the gas-particle velocity (dimensionless $\langle V\rangle_{\rm ani}$ is of order 1), even though the transferred momentum from the gas remains constant with increasing $\mathcal{M}$.

The crossover occurs when the drift for the isotropic case $\langle V\rangle_{\rm iso}\simeq(1-r)\mathcal{M}^{-1}\sqrt{\pi/2}(\sin\theta_0-1)/4$ [2] is of the same order as the drift due to anisotropy. Consequently, the

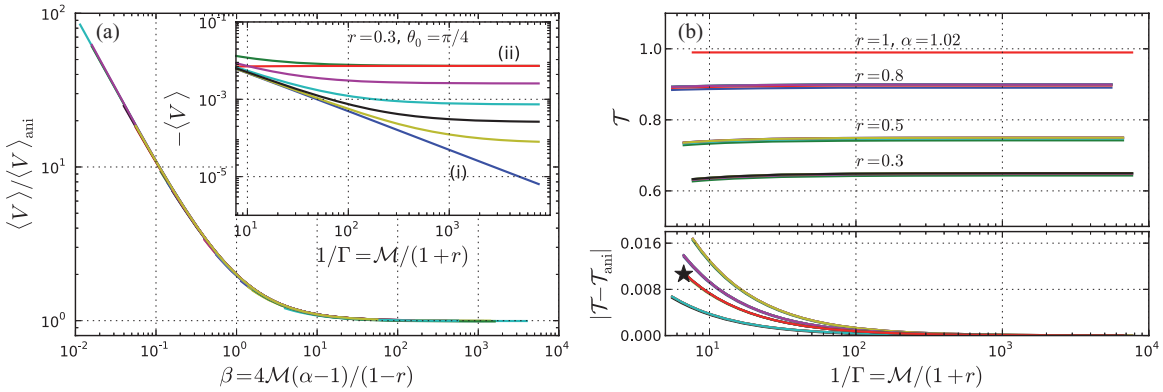


FIG. 3. (Color online) Data for all combinations of $\theta_0=\pi/4, r\in\{0.3,0.5,0.8\}$, and $\alpha\in\{1.02,1.007,1.002,1.0007,1.0002\}$ and $\theta_0=\pi/10$, $r=0.5$, and $\alpha\in\{1.02,1.007,1.002,1.0007,1.0002\}$. (a) Master plot for the motor drift where the inset illustrates the effect of varying $\alpha$. Curves for inelastic collisions with an isotropic gas with $r=0.3$ and $\alpha=1$ [straight blue line (i)] and elastic collisions with an anisotropic gas with $r=1$ and $\alpha=1.02$ [straight red line (ii)] are included for reference. All other curves show the drift for decreasing $\alpha\in\{1.02,1.007,1.002,1.0007,1.0002\}$ from top to bottom. (b) (top) Motor temperature $\mathcal{T}$ for $\theta_0=\pi/4$, $r\in\{0.3,0.5,0.8\}$, and $\alpha\in\{1.02,1.007,1.002,1.0007,1.0002\}$. (bottom) Difference between motor temperature and the asymptotic theory. For comparison, $\theta_0=\pi/10$, $r=0.5$, and $\alpha\in\{1.02,1.007,1.002,1.0007,1.0002\}$ are also shown ($\star$).

dimensionless number

$$\beta := \frac{\langle V\rangle_{\rm ani}}{\langle V\rangle_{\rm iso}} = \frac{4\mathcal{M}(\alpha-1)}{1-r} \tag{15}$$

characterizes the dominant driving of the motor. For $\beta \ll 1$ the dynamics is driven by inelastic collisions ($r < 1$) and for $\beta \gg 1$ the dynamics is driven by anisotropy ($\alpha > 1$). Plotting $\langle V\rangle/\langle V\rangle_{\rm ani}$ as a function of $\beta$ provides an excellent data collapse [Fig. 3(a)].

## VIII. MOTOR TEMPERATURE

Figure 3(b) shows that the temperature is independent of $\mathcal{M}$ for $\mathcal{M} \gtrsim 10$ and it is affected by inelastic collisions more severely than by anisotropy. We now follow the perturbation theory of the previous section to determine the correction to $\mathcal{T}$ in first order of $\alpha - 1$.

Since the motor temperature contains a coefficient of $1/\Gamma$, we must expand $A$ to second order in $\Gamma$. According to Eqs. (12), $A$ then takes the form

$$A \simeq \begin{pmatrix} 0 & 0 & 0 & 0 & \cdots \\ d_{1,0} & d_{1,1} & d_{1,2} & d_{1,3} & \cdots \\ d_{2,0} & 2d_{1,0}+d_{2,1} & 2d_{1,1}+d_{2,2} & 2d_{1,2}+d_{2,3} & \cdots \\ 0 & 3d_{2,0} & 3d_{1,1}+3d_{2,1} & 3d_{1,2}+3d_{2,2} & \cdots \\ \vdots & \vdots & \vdots & \vdots & \ddots \end{pmatrix}.$$

This results in a further increase of the coupling between the different moments. In order to reliably compute $\langle V^2\rangle_{\rm ani}$, the null space of at least the upper left $4\times 4$ submatrix of this matrix must be used, yielding the asymptotic expression for the temperature

$$\frac{2}{1+r}\mathcal{T}_{\rm ani} \simeq 1 + \left[\frac{4-\pi}{4}(1-\sin\theta_0)^2 + \sin^2\theta_0\right](\alpha-1). \tag{16}$$

The lower panel of Fig. 3(b) shows the convergence onto this asymptotic value.

## IX. CONCLUSION

We have investigated the motion of a granular Brownian motor that is driven by inelastic collisions (particle-motor coefficient of restitution $r$) with an anisotropic velocity distribution (with anisotropy $\alpha - 1$), modeled using a squeezed Gaussian [Eq. (1)]. Examining the scaling of the drift with relative motor mass $\mathcal{M}$, we identified a crossover from the motor drift arising due to inelastic gas-motor collisions to a setting where it arises predominantly from the anisotropy of the gas. Examining the steady-state drift of the motor in the limit of large $\mathcal{M}$, we have identified a dimensionless parameter $\beta$ [Eq. (15)] (independent of wedge angle). For $\beta \ll 1$ inelastic collisions drive the drift of the motor and anisotropy is negligible; for $\beta \gg 1$ anisotropy dominates the drift and restitution in motor-gas collisions becomes negligible. In the latter regime we have identified a remarkably strong enhancement of the drift: It is of the order of gas particle velocity, even in the limit of infinite motor-particle mass ratios. Is this remarkable regime accessible experimentally?

Many experiments, involving agitated granular matter, are kept in a steady state via shaking from the walls. Such systems always exhibit an anisotropic velocity distribution [17]. Laboratory experiments can have an anisotropy of the order of $\alpha \approx 2$ [21] and the most conservative estimate for simulations yields $\alpha \approx 1.12$ (see [17], Fig. 4, inset). Given maximally inelastic collisions ($r$ close to 0), this amounts to $\beta \approx 0.5\mathcal{M}$. For $\mathcal{M} > 10$ typical experimental realizations therefore probe, at best, the crossover regime rather than a regime where the drift solely arises from the inelastic collisions. If one wishes to probe the latter regime, the isotropy of the gas particles must be enhanced by at least two orders of magnitude for the experimental setups we are aware of.

The dramatic enhancement of the drift thus lies in an easily accessible regime and it certainly calls for further experimental and numerical exploration.

## ACKNOWLEDGMENTS

We are grateful to P. Colberg, S. Herminghaus, R. Kapral, W. Losert, D. van der Meer, L. Rondoni, and M. Schröter for enlightening discussions.

[1] S. Sporer, C. Goll, and K. Mecke, Phys. Rev. E **78**, 011917 (2008).
[2] B. Cleuren and C. Van den Broeck, Europhys. Lett. **77**, 50003 (2007).
[3] G. Costantini, A. Puglisi, and U. M. B. Marconi, Eur. Phys. J. Spec. Top. **179**, 197 (2010).
[4] S. Joubaud, D. Lohse, and D. van der Meer, Phys. Rev. Lett. **108**, 210604 (2012).
[5] A. Gnoli, A. Petri, F. Dalton, G. Gradenigo, G. Pontuale, A. Sarracino, and A. Puglisi (unpublished).
[6] G. Costantini, U. M. B. Marconi, and A. Puglisi, Europhys. Lett. **82**, 50008 (2008).
[7] P. Meurs, C. Van den Broeck, and A. Garcia, Phys. Rev. E **70**, 051109 (2004).
[8] P. Meurs and C. Van den Broeck, J. Phys.: Condens. Matter **17**, S3673 (2005).
[9] C. Gruber and J. Piasecki, Physica A **268**, 412 (1999).
[10] J. Piasecki and C. Gruber, Physica A **265**, 463 (1999).
[11] A. Fruleux, R. Kawai, and K. Sekimoto, Phys. Rev. Lett. **108**, 160601 (2012).
[12] J. P. D. Clewett, K. Roeller, R. M. Bowley, S. Herminghaus, and M. R. Swift, Phys. Rev. Lett. **109**, 228002 (2012).
[13] K. Roeller, J. P. D. Clewett, R. M. Bowley, S. Herminghaus, and M. R. Swift, Phys. Rev. Lett. **107**, 048002 (2011).
[14] P. Eshuis, D. van der Meer, M. Alam, H. J. van Gerner, K. van der Weele, and D. Lohse, Phys. Rev. Lett. **104**, 038001 (2010).

[15] P. Eshuis, K. van der Weele, D. van der Meer, and D. Lohse, Phys. Rev. Lett. **95**, 258001 (2005).

[16] J. R. Royer, D. Evans, L. Oyarte, Q. Guo, E. Kapit, M. E. Möbius, S. R. Waitukaitis, and H. M. Jaeger, Nature (London) **459**, 1110 (2009).

[17] D. van der Meer and P. Reimann, Europhys. Lett. **74**, 384 (2007).

[18] H. Risken, *The Fokker-Planck Equation: Methods of Solution and Applications* (Springer, Berlin, 1989).

[19] A. Puglisi, P. Visco, E. Trizac, and F. van Wijland, Phys. Rev. E **73**, 021301 (2006).

[20] J. Piasecki, J. Talbot, and P. Viot, Physica A **373**, 313 (2007).

[21] M. Schröter (private communication).

*J. Fluid Mech.* (2014), *vol.* 738, *pp.* 407–422.  

doi:10.1017/jfm.2013.587

# Arrest of the flow of wet granular matter

**Klaus Roeller[1], Johannes Blaschke[1,2], Stephan Herminghaus[1,2] and Jürgen Vollmer[1,2,†]**

[1]Max-Planck-Institut für Dynamik und Selbstorganisation (MPIDS), 37077 Göttingen, Germany

[2]Fakultät für Physik, Georg-August-Universität Göttingen, 37077 Göttingen, Germany

(Received 16 April 2013; revised 4 October 2013; accepted 30 October 2013;
first published online 6 December 2013)

We study the arrest of three-dimensional flow of wet granular matter subject to a sinusoidal external force and a gravitational field confining the flow in the vertical direction. The minimal strength of the external force that is required to keep the system in motion, i.e. the critical force, is determined by considering the balance of injected and dissipated power. This provides a prediction whose quality is demonstrated by a data collapse for an extensive set of event-driven molecular-dynamics simulations where we varied the system size, particle number, the energy dissipated upon rupturing capillary bridges, and the bridge length at which rupture occurs. The same approach also works for systems that are kept at a fixed density by confining walls. In both cases, this universal method provides the critical force irrespective of the flow profile, and without specifying the hydrodynamic equations.

**Key words:** complex fluids, granular media

## 1. Introduction

Sudden arrest of granular flows is a challenge to the theoretical description of granular flows in a hydrodynamic setting (Jaeger, Nagel & Behringer 1996; Kadanoff 1999; Silbert *et al.* 2001; Aranson & Tsimring 2006; Jop, Forterre & Pouliquen 2006; Borzsonyi & Ecke 2007; Forterre & Pouliquen 2008; Luding 2009; Schall & van Hecke 2010; Slotterback *et al.* 2012), as well as an important problem in the engineering sciences (GDR MiDi 2004). Its modelling involves two challenges: (*a*) appropriately incorporating the role of dissipation arising from the particle interactions into the framework of the balance equations underlying hydrodynamic transport equations; and (*b*) addressing the roles of shear stresses, of the spatial distribution of stress, and of yield stress in systems where the flow is spatially anisotropic.

Recent studies (Utter & Behringer 2008; Berardi *et al.* 2010; van Hecke 2010; Tordesillas *et al.* 2011) of granular systems with purely repulsive interactions put severe constraints on hydrodynamic descriptions of dense flows by pointing out a lack of scale separation of microscopic and relevant hydrodynamic time and length scales. Among other problems, this gives rise to a severe dependence of the effective material

† Email address for correspondence: juergen.vollmer@ds.mpg.de

properties on the preparation history (Lois *et al.* 2009). In contrast, hydrodynamic and continuum-mechanics considerations appear to provide a good description for granular systems where the hard-core collisions with restitution are augmented by (reversible) short-ranged attraction between particles (Trappe *et al.* 2001; Rognon *et al.* 2006, 2008). Arguably this is due to the separation of connectivity and rigidity percolation in response to attractive interactions (Lois, Blawzdziewicz & O'Hern 2007, 2008). This idealization of the particle interactions (Pitois, Moucheront & Chateau 2000) applies as long as high-impact-velocity collisions with high capillary numbers dominate the dynamics (see Kantak, Hrenya & Davis 2009; Donahue, Hrenya & Davis 2010*a* for recent applications). On the other hand, recent experimental (Liao & Hsiau 2010; Zhang *et al.* 2010; Remy, Khinast & Glasser 2012; Slotterback *et al.* 2012) and numerical (Remy *et al.* 2012) work on slowly moving shear flow in dense granular systems clearly underlines the important impact of dissipation due to the hysteretic formation and breaking of capillary bridges. Rather than accounting for the finite restitution in collisions and assuming reversible attractive forces, the present work therefore takes a complementary point of view: we explore slow flows in wet systems where dissipation is arising solely from the hysteretic nature of the capillary interaction between the wetting liquid and the particles, i.e. it is due to the formation and rupturing of capillary bridges between particles (Herminghaus 2005; Mitarai & Nori 2006). The hard-core collisions are elastic.

Shear forces that drive the flow can be modelled in various forms. Experimentally studying shear forces in granular systems can be done, for instance, by constructing two counter-rotating cylindrical walls (see Liao & Hsiau 2010 and references therein), by constructing a specialized shear cell (Ren, Dijksman & Behringer 2011), or by exploring a flow down an inclined plane (Quartier *et al.* 2000; Andreotti & Douady 2001; Andreotti, Daerr & Douady 2002; Rahbari *et al.* 2009). Moreover, in numerical models it is convenient to induce shear flow by applying a cosine force field (Schulz, Schulz & Herminghaus 2003; Herminghaus 2005; Roeller, Vollmer & Herminghaus 2009; Rahbari *et al.* 2010). Similarly to the method of images, this may be used to mimic zero flow velocity at the positions envisioned for the walls.

Here, we will focus on the arrest of flow when the force driving the flow falls below a threshold value $F_{ex}$. Considerations based on a system of sheared disks at a fixed density (Rahbari *et al.* 2010) suggest that the critical force, $F_{ex}$, results from the power balance between the energy-injection rate resulting from particle motion in the external force field, and the dissipation rate accounting for the rupture of capillary bridges between the particles.

Surprisingly, we show in the following that the same approach also describes the arrest of flow in a three-dimensional system with constant pressure. The motion in the third dimension is constrained by a hard wall at the bottom and a gravitational field in the vertical direction (figure 1*a*). For external driving forces close to $F_{ex}$ all particles accumulate at the bottom of the cell such that the packing density always lies slightly above random close packing.

This finding is quite remarkable since the setting of constant density (Rahbari *et al.* 2010) fundamentally differs from that of constant pressure: at high packing fraction, the constraint of constant density requires cooperative large-scale rearrangements when two particles pass each other. In contrast the constraint of constant pressure allows particles to pass each other with only local rearrangements. In spite of this considerable difference, the arrest of flow in both settings is obtained by an informed

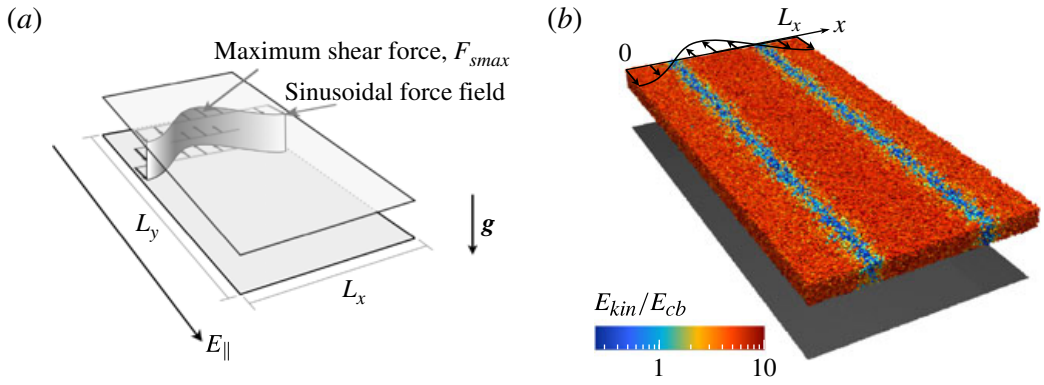


FIGURE 1. (Colour online) (*a*) Sketch of a system of width $L_x = L$ and length $L_y = 2L$ with periodic boundary conditions in the two lateral directions and elastically reflecting top and bottom plates. The space-dependent cosine-shaped force field is indicated by the vertical band and by arrows. Additionally, a gravitational force, $\boldsymbol{g}$, is acting downwards. (*b*) A snapshot of a simulation of $2.15 \times 10^5$ monodisperse spheres of diameter $d$ that interact via a hysteretic square-well potential (see § 2.1). The cosine-shaped shear force field, $\boldsymbol{F}_s(x)$, is sketched on top of the figure. The colour of each particle indicates its individual kinetic energy according to the colour bar at the bottom left. The system size is $L = 100\,d$ and $H = 12.5\,d$, and the filling height is $h = 8.8\,d$ for a shear force of amplitude $F_{smax} = 40\,E_{cb}/L$, i.e. $\hat{F}_{smax} = 0.15$.

inspection of the global energy budget. We argue that this approach hence provides a versatile, universal method to study the arrest of granular flows.

Our paper is organized as follows. In § 2 we describe the system, our numerical approach, and the dimensionless units adopted for modelling. Subsequently, in § 3 we first provide a two-dimensional discussion of the power injected into the systems by the external field, and the dissipated power due to the breaking of capillary bridges and work against gravity. This power balance provides a prediction for the critical force $F_{ex}$. In § 4 the predicted parameter dependence of $F_{ex}$ is compared to the numerical findings. Based on three scalar constants we describe the dependence of the stability boundary in the four-dimensional parameter space spanned by the system size $L$, the particle number $N$, the energy $E_{cb}$ dissipated upon rupturing capillary bridges, and the critical bridge length $s_{cb}$ where rupture occurs. (Here and in the following the subscript $cb$ refers to capillary bridge.) The values of the three constants are interpreted and derived from the model in § 5. In § 6 we augment the two-dimensional model by flow features reflecting the vertical extent of the bed in order to calculate the numerical values of these constants.

## 2. The model

The system is confined in a rectangular cuboid of size $L \times 2L \times H$ with periodic boundary conditions in the $x$- and $y$-directions, and solid, reflecting walls in the $z$-direction. This box contains $N$ particles whose motion is confined in the $z$-direction by a gravitational field of uniform acceleration, $\boldsymbol{g} = -g\hat{\boldsymbol{z}}$, where $\hat{\boldsymbol{z}}$ is the unit vector along the $z$-axis (see figure 1). For the shear flows studied in the present work particles never touch the upper wall of the container due to the gravitational confinement.

In the following ways this setting is fundamentally different from that of the two-dimensional flows considered by Rahbari *et al.* (2010).

(i) Rahbari *et al.* (2010) consider a flow at fixed density close to random close packing. In order to maintain constant density, particles passing each other in the flow require cooperative large-scale rearrangements of large portions of the system.

This is costly energetically, because it is accompanied by the breaking of a large number of capillary bridges.

(ii) Conversely, in gravity-confined granular beds, particles can pass each other via a slight, local expansion of the bed in the vertical direction. Only a few capillary bridges must be ruptured in the resulting fixed-pressure setting, even though the density of the bed is always very close to random close packing.

### 2.1. *Particle interactions*

In the present study we consider monodisperse spheres of diameter $d$, in order to suppress any additional dynamics arising from different particle sizes. In fact, polydisperse beads, which are subject to small shearing forces, segregate according to their size (Schulz *et al.* 2003).

The dynamics in the simulation is calculated using a standard event-driven molecular-dynamics method which has been described in detail by Fingerle *et al.* (2008), Huang, Roeller & Herminghaus (2009), Roeller *et al.* (2009), Ulrich *et al.* (2009*a*,*b*) and Roeller (2010). For the sake of a self-contained exposition we only briefly summarize the particle interactions. Following Herminghaus (2005) the effect of particle adhesion due to the capillary bridges is modelled as follows.

(i) Capillary interaction gives rise to pair forces between particles only.

(ii) Unless particles are connected by a capillary bridge they feel no force when they approach each other.

(iii) They collide elastically, and upon collision a capillary bridge is formed instantaneously. When the particle separate, this bridge gives rise to an attractive force which is modelled by placing the particle into a potential well with a depth $E_{cb}$, and a finite width $s_{cb}$.

(iv) The liquid bridge ruptures at the critical rupture separation, $s_{cb}$. A rupture event is modelled by removing the potential well. Consequentially the particles stop exerting a force on each other, until they touch once again.

In this manner the capillary bridge energy, $E_{cb}$, is dissipated whenever a capillary bridge is removed (i.e. ruptures) after a collision. Particle collisions, without bridge rupture, do not dissipate energy. They can, however, thermalize the particle velocities by redistributing kinetic energy from the ordered centre-of-mass motion into disordered motion. Henceforth, we shall refer to this as each particle's *thermal* degrees of freedom.

Work focusing on individual collisions (Davis, Rager & Good 2002; Antonyuk *et al.* 2009; Donahue *et al.* 2010*a*,*b*, 2012*a*,*b*; Gollwitzer *et al.* 2012) reports a multitude of features of particle collisions involving capillary interactions that cannot fully be captured by this model. On the other hand, the positions of phase boundaries of wet granular fluids appear to be universal in the sense that they only depend on $E_{cb}$ and $s_{cb}$, and not on other details of the particle interaction (Huang *et al.* 2009). For computational convenience all simulations shown in the present paper therefore adopt a hysteretic square-well potential, i.e. we use an event-driven algorithm where the potential takes the form of a square-well with hysteresis as outlined in (i)–(iv).

### 2.2. *Dimensionless units*

Masses are measured in units of the particle mass, $m$, distances in units of the particle diameter, $d$, and the time unit is fixed by measuring forces in terms of $mg$. Non-dimensionalized quantities are denoted by a hat. Unless stated otherwise, the

system size is $\hat{L} \times 2\hat{L} \times \hat{H} = 60 \times 120 \times 7.5$, and the number of monodisperse particles is $4.39 \times 10^4$, resulting in a filling height of $\hat{h} = 5.0$. Furthermore, the capillary interaction gives $\hat{E}_{cb} = 3/8$ and $\hat{s}_{cb} = 1/16$.

### 2.3. *Shear flow and arrest*

A shear flow is induced by applying a space-dependent external force field

$$\boldsymbol{F}_s(x) = F_s(x)\,\hat{\boldsymbol{y}} \quad \text{with } F_s(x) = F_{smax}\cos\frac{2\pi x}{L} \tag{2.1}$$

to the system (Hoover 1983; Schulz *et al.* 2003; Schulz & Schulz 2006; Rahbari *et al.* 2009, 2010), which accelerates particles along the $\hat{\boldsymbol{y}}$-direction. The particles are initially homogeneously distributed within the system with a Gaussian velocity distribution of mean granular temperature $T_g/E_{cb} = 40.0$.

For external forces with an amplitude, $F_{smax}$, slightly larger than the critical forcing, $F_{ex}$, the system approaches a fluid flow whose local centre-of-mass velocity follows the external field. (The kinetic energy of states above the flow threshold gradually grows. Eventually, for time scales much larger than those studied here, this can lead to flow instabilities (see Roeller *et al.* 2009).) In figure 1(*b*) we illustrate such a system by visualizing a flow in a larger simulation box, where $\hat{L} = 100$ and $\hat{H} = 12.5$, accommodating a greater filling height of $\hat{h} \simeq 8.8$, and an external force only 11% above $F_{ex}$. In that situation shear bands form such that the capillary bridges in the region around $L_x/4$ and $3L_x/4$ are ruptured, while in the other parts the network of capillary bridges evolves only slowly. For shear forces smaller than $F_{ex}$ the system eventually arrests in a solid state with a frozen network of nearest neighbours.

In passing we note that this arrest of flow is conceptually different from those jamming transitions where crowding and hard-core interactions prevent particles from passing each other, even at arbitrarily strong applied shear forces (Cates *et al.* 1998; Trappe *et al.* 2001; O'Hern *et al.* 2003; Drocco *et al.* 2005; Bi *et al.* 2011). This form of jamming is prevented here because the system can expand in the vertical direction where it is only bounded by gravity (see, for example Valverde, Quintanilla & Castellanos 2004 and references therein). Furthermore, the transition is also distinct from those observed in earlier studies on cohesive granular materials: we focus on the role of dissipation due to the hysteretic nature of capillary bridge ruptures, while previous studies (Trappe *et al.* 2001; Rognon *et al.* 2006, 2008) address conservative attractive forces. They implemented dissipation via grain friction and a restitution coefficient smaller than one (Rognon *et al.* 2006, 2008), or indirectly by treating the suspending fluid of attractive colloidal particles as an inert background (Trappe *et al.* 2001).

### 2.4. *Measuring $F_{ex}$*

The kinetic energy, $E_y$, of motion parallel to the driving shear force will serve as the order parameter to distinguish the dynamics. Rahbari *et al.* (2010) used the amplitude of the velocity profile in the direction of the external field (i.e. the amplitude of the velocity response in reaction to the applied force field, $F_{smax}$) as an order parameter. This has advantages when following the hysteresis loop of the response upon slowly decreasing and subsequently increasing $F_{smax}$. In the present study where we focus on the arrest of flow only, the kinetic energy, $E_y$, is a numerically stable and more easily accessible order parameter.

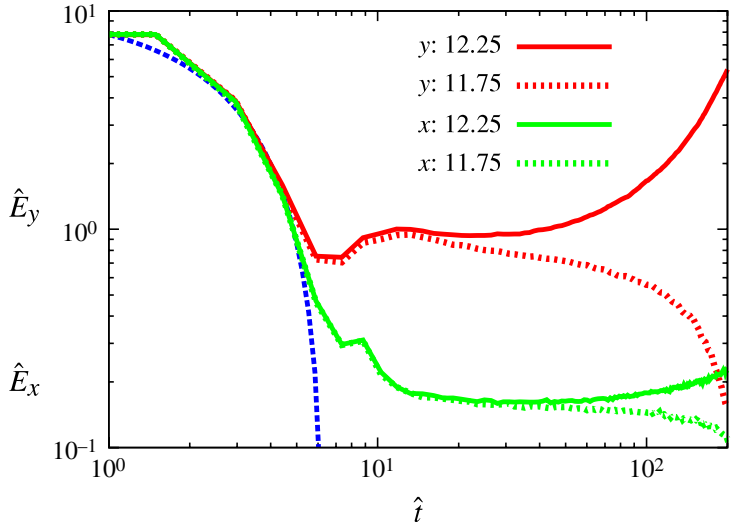


FIGURE 2. (Colour online) Time evolution of the kinetic energy, $\hat{E}_y$, of motion parallel to $\boldsymbol{F}_s$ (upper set of lines), and that in transverse direction, $\hat{E}_x$ (lower set of lines) for a system of size $\hat{L} = 50$ driven by shear forces with amplitude $\hat{F}_{smax} \simeq 0.235$ (dotted lines) and 0.245 (solid lines), respectively. Initially all curves approximately follow the dynamics of free cooling (dashed line, see Ulrich *et al.* 2009*b* for the derivation) until the kinetic energy reaches values of the order of $E_{cb}$. Subsequently, the applied field is too weak to support sustained flow, and one encounters arrest at finite times into a state with no system-spanning flow (dotted line). For larger amplitudes of the force, the field injects a sufficient amount of energy into the system to permit sustained motion (solid lines). They eventually enter a state where the flow shows a rich time-dependent dynamics (cf. Roeller *et al.* 2009).

In figure 2 its time evolution is shown together with the kinetic energy, $E_x$, of the motion transverse to the external field. When started in a state with high kinetic energy, the fluid first cools down in a manner closely reminiscent of free cooling (Ulrich *et al.* 2009*a*,*b*). Starting at $\hat{t} \simeq 10$ it has cooled so far that the acceleration due to the external field becomes noticeable over the initial kinetic energy. Depending on whether the external field is stronger or weaker than a sharp critical value, $\hat{F}_{ex}$, the fluid either gains sufficient energy to remain in the fluid state forever, or it settles into the arrested state. The phase boundary, $F_{ex}$, is calculated as the mean value between the neighbouring values of shear forces, $\hat{F}_{smax}$, which approach different final states. For the data shown in figure 2 it is $\hat{F}_{ex} \simeq 0.240$.

The phase boundary hence corresponds to the smallest external force that still leads to sustained shear flow. We demonstrate in the following that the flow at this threshold corresponds to motion in a liquid state where the energy injected by the external field is exactly balanced by dissipation due to rupture of capillary bridges.

## 3. Fluidization point: two-dimensional model

In this section we discuss the power balance of the flow. Energy is injected into the kinetic energy of the particles due to their motion in the external force field. In a steady state this power is balanced by the energy dissipation rate due to the inelastic particle collisions. For external forces close to $F_{ex}$ the granular temperature is small. Therefore, effects due to the thermal motion may be neglected, and the energy dissipation rate is dominated by the rupture of capillary bridges when particles pass each other in the flow field.

For all investigated systems the flow remains translationally invariant in the $y$-direction, in accordance with the symmetry of the forcing. Moreover, the density of the liquid cannot be distinguished from the random close packing density, $\phi_{rcp}$, and the height of the layer is spatially uniform. Consequently, the number of particles, $n(x)\,\mathrm{d}x$, in a thin rectangular cuboid of size $2L \times h \times \mathrm{d}x$ aligned parallel to the external field takes a constant value, $N/L$, where $N$ denotes the number of particles in the system and $L$ the system size transverse to the flow. This finding is in line with the expectation that a flow breaking the symmetries of the system or noticeably expanding the bed would give rise to higher dissipation.

### 3.1. *Energy injection rate*

Let $v_y(x)$ denote the profile of the flow established when applying the critical force $F_s(x) = F_{smax}\cos(2\pi x/L) \stackrel{!}{=} F_{ex}\cos(2\pi x/L)$. The input power that is injected by means of this external force acting on the particles is given by

$$\begin{aligned}\langle P_{forcing}\rangle &= \int_0^L v_y(x)\,F_s(x)\,n(x)\,\mathrm{d}x \\ &= \frac{N\,F_{ex}}{L}\int_0^L v_y(x)\,\cos\frac{2\pi x}{L}\,\mathrm{d}x. \end{aligned} \tag{3.1}$$

Up to the factor $N\,F_{ex}$ this amounts to the leading-order Fourier coefficient of the expansion of the velocity profile $v_y(x)$. Consequently, the injected power takes the form

$$\langle P_{forcing}\rangle = C_f N \Delta v_y\,F_{ex} \tag{3.2}$$

where $\Delta v_y$ is the amplitude of the velocity field. Admissible values of $C_f$ lie in the narrow range $0.5 < C_f < \pi/4$. The constant $C_f$ takes the value 0.5 when the velocity profile is faithfully approximated by its first even harmonic, i.e. $v_y(x) \simeq \Delta v_y\cos(2\pi\,x/L)$, and $C_f = \pi/4 \simeq 0.785$ in the other extreme case of plug flow. Hence, $C_f$ characterizes the shape of the velocity response to the applied external field.

### 3.2. *Energy dissipation rate*

For each particle the creeping flow enforces a change of neighbours (in the direction of the flow) with a rate $\dot\gamma = \mathrm{d}v_y/\mathrm{d}x$. Such a displacement results in an energy dissipation of $\dot\gamma\,\nu E_{cb}$ due to rupturing on average a number $\nu$ of capillary bridges per change of neighbours. The total power dissipated upon rupturing capillary bridges is thus given by

$$\langle P_{bridge}\rangle = \int_0^L n(x)\left|\frac{\mathrm{d}v_y}{\mathrm{d}x}\right|\,\nu\,E_{cb}\,\mathrm{d}x. \tag{3.3}$$

For every $L$-periodic function $v_y(x)$ with a single local maximum per period, this integral yields

$$\langle P_{bridge}\rangle = \frac{4\,N\,\Delta v_y}{L}\,\nu\,E_{cb}, \tag{3.4}$$

provided that $n(x) \equiv N/L$ is spatially uniform.

For the present system, rearrangements due to two particles passing each other are achieved by a slight vertical expansion of the particle bed. Assuming that there is no

height preference for the rearrangements, and that there are on average $h/2d$ particles in the column on top of the pair under consideration, a potential energy of

$$U = C_U \frac{h}{2d} mg\Delta h \tag{3.5}$$

is associated with the expansion. Here, $C_U$ accounts for the number of columns to be lifted, and $\Delta h$ to the expansion in height. Due to the frequent collisions in the dense bed the potential energy $U$ is immediately dissipated into thermal degrees of freedom (i.e. the random component of the particle velocities) of the granular fluid, and therefore it is not just a one-off investment. Rather, work has to be done against gravity each time particles move past each other. Multiplying this energy with the frequency of particle passages, $4N\Delta v_y/L$ (as given by (3.4)), therefore provides a second contribution to the energy dissipation,

$$\langle P_{grav} \rangle = \frac{4N\,\Delta v_y}{L} U = \frac{4N\,\Delta v_y}{L} C_U \frac{\Delta h}{2d} mgh. \tag{3.6}$$

### 3.3. *Predicting the critical force* $\hat{F}_{ex}$

Assuming that bridge rupture occurs only in the plane parallel to the applied force, the effect of the third dimension is then only to provide an additional energy sink due to gravity, $\langle P_{grav} \rangle$. Therefore, in a steady state the total dissipation rate, due to rupturing bridges and relaxation of $U$ into thermal degrees of freedom, has to balance the input power. We hence obtain

$$\begin{aligned} &\langle P_{forcing} \rangle = \langle P_{bridge} \rangle + \langle P_{grav} \rangle \\ &\Leftrightarrow F_{ex} L = aE_{cb} + bmgh \\ &\Leftrightarrow \hat{F}_{ex} \hat{L} = a\hat{E}_{cb} + b\hat{h}, \end{aligned} \tag{3.7a}$$

$$\text{with } a = \frac{4\nu}{C_f} \tag{3.7b}$$

$$b = \frac{2C_U \Delta \hat{h}}{C_f}. \tag{3.7c}$$

At this point, it is worth pointing out that the flow's response to the external force field is characterized by its amplitude, $\Delta v_y$, and the parameter, $C_f$, which characterizes the shape of the velocity response. The amplitude-dependence, $\Delta v_y$, cancels in the power balance. In the worst case, the parameter $C_f$ can vary by no more than a factor of 1.6. Furthermore, for external forcing close to $\hat{F}_{ex}$ the variability is expected to be even smaller. Hence, one expects that $\hat{F}_{ex}$ is well-approximated by (3.7) under the assumption that $C_f$ is a constant of order unity. Thus, it is not necessary to determine $C_f$ by calculating it from the flow directly.

The coefficient $a$ characterizes the mean number of capillary bridges ruptured in the flow as particles pass each other. Likewise $C_U$ counts how many rows of particles are lifted when the particles pass each other. As a consequence, $b\,mgh$ is the average amount of work done against gravity in the flow per unit time.

We hence predict that $\hat{F}_{ex}$ is inversely proportional to the system size $\hat{L}$, and that $\hat{F}_{ex}\hat{L}$ is a linear function of $\hat{E}_{cb}$ and the filling height $\hat{h}$. In the following section we compare these predictions to the results of the molecular-dynamics simulations.

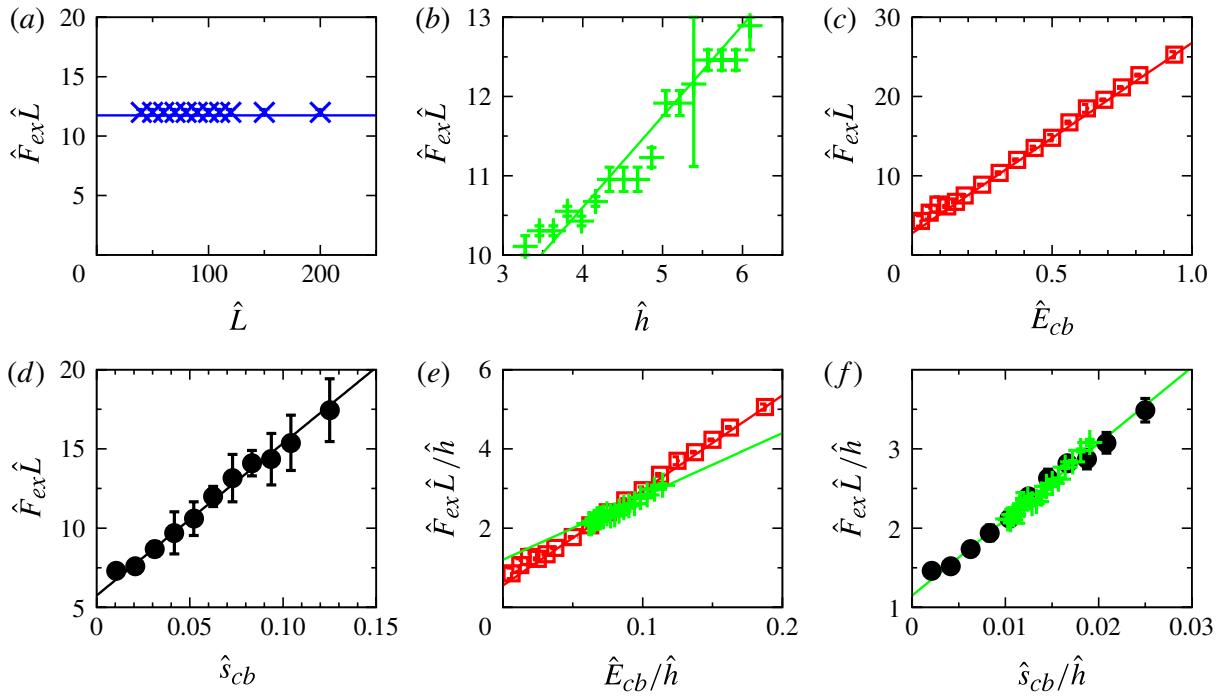


FIGURE 3. (Colour online) The parameter dependence of the critical driving forces, $\hat{F}_{ex}$, separating regions that lead to either solid or fluidized behaviour. The symbols indicate the phase boundary between the two phases, and solid lines are the theoretical predictions described in the main text. For most of the data points the numerical error in the phase boundary is smaller than the size of the symbol. (*a–d*) The phase boundary between the solid and the fluidized state upon varying different parameters: (*a*) system size, $\hat{L}$, (*b*) filling height $\hat{h}$, (*c*) dissipated energy, $\hat{E}_{cb}$, and (*d*) critical rupture separation, $\hat{s}_{cb}$. In (*e*) $\hat{F}_{ex}\hat{L}/\hat{h}$ is plotted as a function of $\hat{E}_{cb}/\hat{h}$ in order to demonstrated that the data of (*b*) and (*c*) are not compatible with the prediction, (3.7). (*f*) A collapse of the data of (*b*) and (*d*), when $\hat{F}_{ex}\hat{L}/\hat{h}$ is plotted as a function $\hat{s}_{cb}/\hat{h}$ in order to demonstrate that $\hat{s}_{cb}$ and $\hat{h}$, rather than $\hat{E}_{cb}$ and $\hat{h}$ may considered independent parameters to predict $\hat{F}_{ex}\hat{L}$. The method for performing the simulations is discussed in the text.

## 4. Comparison to numerical data

In figure 3(*a–d*) we explore the dependence of $\hat{F}_{ex}$ on the systems size, $L$, the filling height, $h$, the dissipated energy, $E_{cb}$, and the rupture length, $\hat{s}_{cb}$. Plotting $\hat{F}_{ex}$ as a function of the respective parameters provides sections through the phase diagram: there is sustained flow for values of $\hat{F}_s$ larger than $\hat{F}_{ex}$ and flow is arrested for smaller external forces.

### 4.1. *Parameter dependence of* $\hat{F}_{ex}$

(*a*) The system size $\hat{L}$ was varied whilst keeping the aspect ratio of the container constant at $L_y/L_x = 2$. At the same time the average particle number density was kept constant at $\phi = 0.43$ which means that the number of particles is changing in order to provide a fixed filling height, $\hat{h} \simeq 5$. As expected from (3.7) the value of $\hat{F}_{ex}\hat{L}$ is constant. We find that $\hat{F}_{ex}\hat{L} \simeq 12$ for fixed $\hat{E}_{cb} = 0.375$ and $\hat{h} \simeq 5$ (figure 3*a*).

(*b*) The filling height, $\hat{h}$, was varied by changing the number of particles in the system whilst keeping the geometry of the simulation volume and particle interactions fixed. The filling height is estimated as the filling height in the solid state when

assuming random close packing. As predicted by (3.7) the dependence of $\hat{F}_{ex}\hat{L}$ on $\hat{h}$ for a fixed $\hat{E}_{cb}$ is linear. In the simulations we find

$$\hat{F}_{ex}\hat{L} \simeq 6.0 + 1.2\,\hat{h} \tag{4.1}$$

for $\hat{E}_{cb} = 0.375$ (figure 3*b*).

(*c*) Whilst varying the capillary bridge energy, $E_{cb}$, the rupture separation, $\hat{s}_{cb} = 1/16$, filling height, $\hat{h} \simeq 5$, and the system size, $\hat{L} = 60$, were kept constant. Figure 3(*c*) shows the expected linear dependence of $\hat{F}_{ex}\hat{L}$ on $\hat{E}_{cb}$,

$$\hat{F}_{ex}\hat{L} \simeq 24\hat{E}_{cb} + 2.8. \tag{4.2}$$

Central to the assertion of linear dependence is that $C_f$ takes a constant value close to arrest. The slight deviation from the linear fit for small $\hat{E}_{cb}$ expresses a slight increase of the deviation of the velocity profile from a cosine profile.

(*d*) The critical rupture separation, $s_{cb}$, was varied for a fixed aspect ratio of width versus depth of the potential well, i.e. $E_{cb}$ was varied together with $s_{cb}$ at a fixed ratio of $R \equiv E_{cb}/s_{cb} = 6.0$. System size and filling height were fixed to $\hat{L} = 60$ and $\hat{h} = 5$, respectively. The resulting linear dependence

$$\hat{F}_{ex}\hat{L} \simeq 16\,R\,\hat{s}_{cb} + 6.0 \tag{4.3}$$

is shown in figure 3(*d*).

### 4.2. *Consistency checks: effects of the third dimension*

Merely finding linear dependences of $\hat{F}_{ex}$ on $\hat{h}$, $\hat{E}_{cb}$ and $\hat{s}_{cb}$ is not sufficient to show that (3.7) faithfully describes the arrest of flow. One also has to verify that the linear functions are mutually consistent for all sections through the phase diagram.

(*e*) In order to compare (4.1) and (4.2), their respective *y*-intercepts need to be expressed in terms of the quantity held constant in (*b*) and (*c*). The *y*-intercept of (4.1) may be written as $6.0 \simeq 16\,\hat{E}_{cb}$ given that $\hat{E}_{cb} = 0.375$. Whereas the *y*-intercept of (4.2) can be written as $2.8 \simeq 0.56\,\hat{h}$ for $\hat{h} = 5$. This gives two linear equations,

$$\hat{F}_{ex}\hat{L} \simeq 16\,\hat{E}_{cb} + 1.2\hat{h} \quad \text{according to (4.1)}, \tag{4.4a}$$

$$\hat{F}_{ex}\hat{L} \simeq 24\,\hat{E}_{cb} + 0.56\,\hat{h} \quad \text{according to (4.2)}, \tag{4.4b}$$

that must hold simultaneously if (3.7) is an accurate model. Plotting $\hat{F}_{ex}\hat{L}/\hat{h}$ versus $\hat{E}_{cb}/\hat{h}$ in figure 3(*e*) shows that this is clearly not the case. Consequentially the data shown in figure 3(*b*,*c*) lie on different straight lines. It is not admissible to interpret (3.7*a*) as a linear relation with constant coefficients $a$ and $b$, and $\hat{E}_{cb}$ and $\hat{h}$ as independent variables.

(*f*) In order to provide a physical interpretation of the origin of this deviation, we note that the data shown in figures 3(*d*) and 3(*b*) are compatible. Equation (4.3) is commensurate with (4.1) since the latter has a *y*-intercept of $6.0 = 16\,\hat{E}_{cb} = 16\,R\hat{s}_{cb}$ with $R = 6.0$ and $\hat{s}_{cb} = 1/16$, and since the *y*-intercept of (4.3) is $6.0 = 1.2\,\hat{h}$ with $\hat{h} = 5.0$.

In the following we show that a consistent description of the numerical data can only be achieved by assuming that $a$ has a weak, linear dependence on $\hat{h}$.

Equation (3.7) is consistent with the numerical data when taking into account a monotonic increase of the number of bridge ruptures for increasing $h/s_{cb}$. After

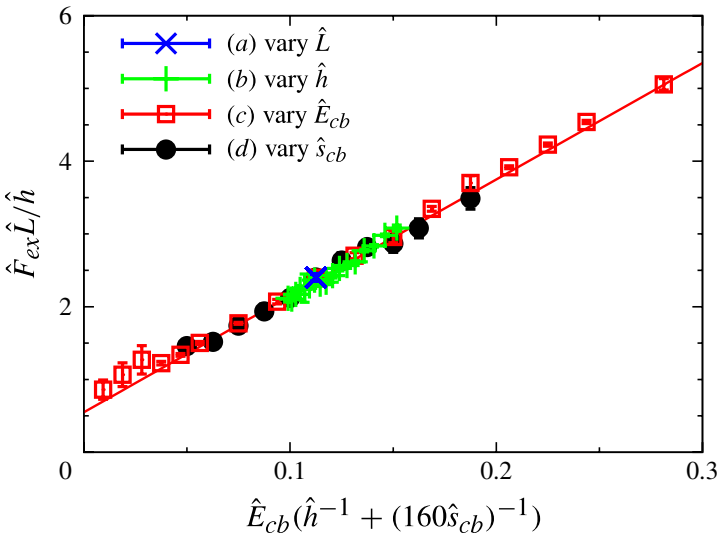


FIGURE 4. (Colour online) The solid line shows our theoretical prediction, (5.1) involving only three free parameters $\tilde{a}$, $\tilde{b}$, and $\tilde{\chi}$ whose values can also explicitly be calculated. It provides a master plot incorporating all data shown in the different panels of figure 3. The dependence of the critical force $F_{ex}$ on the system size, $\hat{L}$, the filling height, $\hat{h}$, the energy dissipated upon rupturing capillary bridges, $\hat{E}_{cb}$, and the critical rupture separation, $\hat{s}_{cb}$, is faithfully described. The data points referring to different system size are so close that they all lie on top of each other in this representation.

all, swapping events also lead to rupturing bridges along the sides of the vertically displaced column of particles on top of the considered site.

## 5. Fluidization point: three-dimensional model and data collapse

The likelihood of rupturing bridges in the vertical direction can be derived from the disparity between (4.3) and (4.2). They can only be consistent if the $y$-intercept of (4.3) comprises a contribution proportional to $R$, and if the slopes are adjusted accordingly, i.e. by decomposing the $y$-intercept as $6.0 = 1.2\,\hat{h} \simeq (0.55 + R/10)\,\hat{h}$ with $\hat{h} = 5$ and $R = 6.0$. Observing that $R \equiv E_{cb}/s_{cb}$ this provides an improved prediction

$$\hat{F}_{ex}\hat{L} \simeq \left(1 + \tilde{\chi}\,\frac{\hat{h}}{\hat{s}_{cb}}\right)\tilde{a}\hat{E}_{cb} + \tilde{b}\hat{h}. \tag{5.1a}$$

The agreement of all of our numerical data with this prediction is demonstrated in figure 4. It shows a master plot where all data shown in figure 3 collapse on a single line, (5.1$a$) with coefficients

$$\tilde{a} \simeq 16 \quad \text{bridge ruptures}, \tag{5.1b}$$

$$\tilde{b} \simeq 0.55 \quad \text{flow dilation}, \tag{5.1c}$$

$$\tilde{\chi} \simeq 1/160 \quad \text{out-of-plane bridge ruptures}. \tag{5.1d}$$

*A priori*, it is not clear whether these values comply with their physical interpretation. As a final step of the data analysis, we check our findings by estimating the expected values of the parameters $\tilde{a}$, $\tilde{b}$ and $\tilde{\chi}$.

### 5.1. *Determination of* $\tilde{a}$

In view of (3.7*b*) the parameter $a$ is related to the number, $\nu$, of capillary bridge ruptures in every particle exchange

$$a = \frac{4\,\nu}{C_f} \simeq 8\nu, \tag{5.2}$$

where we used the estimate $C_f \simeq 0.5$, as argued upon introducing this constant in (3.2). Moreover, in order to take into account the correction term for the height dependence introduced in (5.1) another factor $1 + \hat{h}/160\hat{s}_{cb}$ must also be considered. For the standard choice of parameters $\hat{h} = 5$ and $\hat{s}_{cb} = 1/16$ we hence find

$$\tilde{a} = \frac{4\nu}{C_f}\left(1 + \frac{\hat{h}}{160\hat{s}_{cb}}\right)^{-1} \simeq \frac{16}{3}\nu. \tag{5.3}$$

Finally, in a granular bed that is expanding to allow particles to pass each other the number $\nu$ of rupture events must be larger than 1, but still small. For $\nu = 3$ we hence recover the value $\tilde{a} = 16$ reported in (5.1*b*).

### 5.2. *Determination of* $\tilde{b}$

In order to see that the value for $b \simeq 0.55$ is also reasonable, we observe that subsequent rows of spheres in a close-packed structure are separated by a height distance $\hat{h}_{cp} = \sqrt{2/3} \simeq 0.816$ and that the saddle that has to be passed to roll from one minimum to a nearby minimum is at height $\hat{h}_{saddle} = \sqrt{3}/2 \simeq 0.866$. The minimum expansion in height to move over the potential landscape set up by the layers below is therefore of the order of $\Delta\hat{h} \simeq \hat{h}_{saddle} - \hat{h}_{cp} \simeq 0.05$. Potential wells in a disordered, only slightly expanded random packing, will still be of the same order of magnitude. Based on this estimate, on $C_f \simeq 0.5$, and on (3.7*c*) the number of columns, $C_U$, lifted in a swapping event amounts to

$$C_U \simeq 0.55\frac{C_f}{2\Delta\hat{h}} \simeq 2.8. \tag{5.4}$$

Lifting a small number of columns gives plausibility to $b \simeq 0.55$.

### 5.3. *Determination of* $\tilde{\chi}$

In order to gain insight into the order of magnitude of $\tilde{\chi}$ we note that the lifted column needs to rupture bonds all along its walls. Hence, $\nu$ is not merely dependent on its cross-section, as implied by assuming $\nu$ to be independent of $\hat{h}$. The number of bonds that are broken is then expected to scale linearly with column height and inversely proportional to $\hat{s}_{cb}$. After all, bonds are allowed to stretch to a finite length $\hat{s}_{cb}$, and the larger $\hat{s}_{cb}$ the lower the likelihood that the dilation requires a given bond (along the vertical walls of the pile of particles displaced vertically) to be broken. This leads to an additional number $\tilde{\chi}\,\nu\hat{h}/\hat{s}_{cb}$ of bonds broken per column. As we saw above, it increases the number of bond ruptures by $\sim$50 % which seems reasonable in a system with a packing height of only five layers and a rupture separation, $\hat{s}_{cb} = 1/16 = 0.065$ that is larger than the average height displacement, $\Delta\tilde{h} = 0.05$, of the column. After all, in such a situation only pre-stretched bonds are likely to rupture. Keeping this in mind, the small value of $\tilde{\chi}$ may be understood as a result of incorporating a factor of $\Delta\tilde{h}$ and a probability of $\sim 1/4$ to encounter a pre-stretched

bond in a layer of a column that is vertically displaced. In this interpretation the average number of layers in the column is $\hat{h}/2$.

## 6. Summary and outlook

The present study substantiates the finding that the transition from a fluidized to an arrested state in wet granular matter arises when the dissipation rate due to the rupture of capillary bridges in the shear flow can no longer be balanced by the power injection from the external field. Earlier work (Rahbari *et al.* 2010) showed that this approach provides a comprehensive understanding of the transition in settings where the density is fixed by a confining box. The present work addressed the flow of a bed kept at constant pressure by confining it in the vertical direction by a gravitational field. Just above the transition the flow is reminiscent of a slow plastic flow of the bed in the direction of the applied field: the bed expands only minimally in the vertical direction, and gravity keeps density, filling height, and pressure to values observed in an arrested packing. Also, for this gravitationally confined wet granular flow the power balance provides an accurate prediction, (5.1), of the critical force at which the flow ceases. This is demonstrated by a master plot, figure 4, showing a collapse of all numerical data obtained by varying four different characteristics of the system: the system size, the filling height, as well as the strength and critical rupture separation of capillary bridges. Our data collapse suggests that the prediction of the flow threshold involves only three constants characterizing the types of dissipative events:

(i) When the granular flow is confined by gravity, typically only 2–3 capillary bridges are ruptured upon swapping neighbouring particles moving with slightly different speed in the direction of the external forcing. This is a striking difference to wall-bounded flows (Rahbari *et al.* 2010) where this number diverges when the density approaches close packing.

(ii) In a gravity-confined granular bed the effortless passing of the particles is facilitated by a slight expansion of the granular bed where 2–3 columns of particles are lifted by a small amount to let the particles pass between neighbouring potential wells arising from the corrugations formed by the layer below. The associated potential energy is also dissipated.

(iii) With a small probability additional capillary bridges are broken due to the slight expansions in vertical direction.

The most remarkable finding of our study is that the critical force $F_{ex}$ can be determined from the forcing alone. No details of the flow's response are required to predict whether the flow will arrest. $F_{ex}$ can be calculated without specifying the hydrodynamic equations of the flow and determining their solution. We therefore conclude that the approach of balancing the energy input rate (due to the external force inducing the flow) and the dissipation rate (due the rupture of capillary bridges, when particles move past each other) provides a powerful framework to study the arrest of flow in wet granular materials. It provides a universal method to predict the threshold for the arrest of flow.

## Acknowledgements

We are indebted to M. Brinkmann, K. Daniels, W. Losert and M. Schröter for stimulating discussion. J.B., S.H., and J.V. gratefully acknowledge financial support by BP Exploration Operating Company Ltd.

## REFERENCES


ANDREOTTI, B., DAERR, A. & DOUADY, S. 2002 Scaling laws in granular flows down a rough plane. *Phys. Fluids* **14** (1), 415.

ANDREOTTI, B. & DOUADY, S. 2001 Selection of velocity profile and flow depth in granular flows. *Phys. Rev.* E **63** (3), 031305.

ANTONYUK, S., HEINRICH, S., DEEN, N. & KUIPERS, H. 2009 Influence of liquid layers on energy absorption during particle impact. *Particuology* **7** (4), 245–259.

ARANSON, I. S. & TSIMRING, L. S. 2006 Patterns and collective behaviour in granular media: theoretical concepts. *Rev. Mod. Phys.* **78** (2), 641.

BERARDI, C. R., BARROS, K., DOUGLAS, J. F. & LOSERT, W. 2010 Direct observation of stringlike collective motion in a two-dimensional driven granular fluid. *Phys. Rev.* E **81** (4), 041301.

BI, D., ZHANG, J., CHAKRABORTY, B. & BEHRINGER, R. P. 2011 Jamming by shear. *Nature* **480** (7377), 355–358.

BORZSONYI, T. & ECKE, R. E. 2007 Flow rule of dense granular flows down a rough incline. *Phys. Rev.* E **76** (3), 031301.

CATES, M. E., WITTMER, J. P., BOUCHAUD, J.-P. & CLAUDIN, P. 1998 Jamming, force chains, and fragile matter. *Phys. Rev. Lett.* **81** (9), 1841–1844.

DAVIS, R. H., RAGER, D. A. & GOOD, B. T. 2002 Elastohydrodynamic rebound of spheres from coated surfaces. *J. Fluid Mech.* **468**, 107–119.

DONAHUE, C. M., BREWER, W. M., DAVIS, R. H. & HRENYA, C. M. 2012*a* Agglomeration and de-agglomeration of rotating wet doublets. *J. Fluid Mech.* **708**, 128–148.

DONAHUE, C. M., DAVIS, R. H., KANTAK, A. A. & HRENYA, C. M. 2012*b* Mechanisms for agglomeration and deagglomeration following oblique collisions of wet particles. *Phys. Rev. E* **86**, 021303.

DONAHUE, C. M., HRENYA, C. M. & DAVIS, R. H. 2010*a* Stokes' cradle: Newton's cradle with liquid coating. *Phys. Rev. Lett.* **105**, 034501.

DONAHUE, C. M., HRENYA, C. M., DAVIS, R. H., NAKAGAWA, K. J., ZELINSKAYA, A. P. & JOSEPH, G. G. 2010*b* Stokes' cradle: normal three-body collisions between wetted particles. *J. Fluid Mech.* **650**, 479–504.

DROCCO, J. A., HASTINGS, M. B., OLSON REICHHARDT, C. J. & REICHHARDT, C. 2005 Multiscaling at point *j*: jamming is a critical phenomenon. *Phys. Rev. Lett.* **95** (8), 088001.

RAHBARI, S. H. E., VOLLMER, J., HERMINGHAUS, S. & BRINKMANN, M. 2009 A response function perspective on yielding of wet granular matter. *Europhys. Lett.* **87**, 14002.

FINGERLE, A., ROELLER, K., HUANG, K. & HERMINGHAUS, S. 2008 Phase transitions far from equilibrium in wet granular matter. *New J. Phys.* **10** (5), 053020.

FORTERRE, Y. & POULIQUEN, O. 2008 Flows of dense granular media. *Annu. Rev. Fluid Mech.* **40**, 1–24.

GDR MIDI, 2004 On dense granular flows. *Eur. Phys. J.* E **14**, 341–365.

GOLLWITZER, F., REHBERG, I., KRUELLE, C. A. & HUANG, K. 2012 Coefficient of restitution for wet particles. *Phys. Rev. E* **86**, 011303.

VAN HECKE, M. 2010 Jamming of soft particles: geometry, mechanics, scaling and isostaticity. *J. Phys.: Condensed Matter* **22** (3), 033101.

HERMINGHAUS, S. 2005 Dynamics of wet granular matter. *Adv. Phys.* **54** (3), 221–261.

HOOVER, W. G. 1983 Nonequilibrium molecular dynamics. *Annu. Rev. Phys. Chem.* **34** (1), 103–127.

HUANG, K., ROELLER, K. & HERMINGHAUS, S. 2009 Universal and non-universal aspects of wet granular matter under vertical vibrations. *Eur. Phys. J. Special Topics* **179**, 25–32.

JAEGER, H. M., NAGEL, S. R. & BEHRINGER, R. P. 1996 Granular solids, liquids, and gases. *Rev. Mod. Phys.* **68** (4), 1259–1273.

JOP, P., FORTERRE, Y. & POULIQUEN, O. 2006 A constitutive law for dense granular flows. *Nature* **441**, 727–730.

KADANOFF, L. P. 1999 Built upon sand: theoretical ideas inspired by granular flows. *Rev. Mod. Phys.* **71** (1), 435–444.

KANTAK, A. A., HRENYA, C. M. & DAVIS, R. H. 2009 Initial rates of aggregation for dilute, granular flows of wet particles. *Phys. Fluids* **21**, 023301.

LIAO, C.-C. & HSIAU, S.-S. 2010 Experimental analysis of dynamic properties in wet sheared granular matter. *Powder Technol.* **197** (3), 222–229.

LOIS, G., BLAWZDZIEWICZ, J. & O'HERN, C. S. 2007 Jamming in attractive granular media. *Proc. Appl. Maths. Mech.* **7** (1), 1090605–1090606.

LOIS, G., BLAWZDZIEWICZ, J. & O'HERN, C. S. 2008 Jamming transition and new percolation universality classes in particulate systems with attraction. *Phys. Rev. Lett.* **100**, 028001.

LOIS, G., ZHANG, J., MAJMUDAR, T. S., HENKES, S., CHAKRABORTY, B., O'HERN, C. S. & BEHRINGER, R. P. 2009 Stress correlations in granular materials: an entropic formulation. *Phys. Rev.* E **80**, 060303.

LUDING, S. 2009 Towards dense, realistic granular media in 2d. *Nonlinearity* **22** (12), R101–R146.

MITARAI, N. & NORI, F. 2006 Wet granular materials. *Adv. Phys.* **55** (1–2), 1–45.

O'HERN, C. S., SILBERT, L. E., LIU, A. J. & NAGEL, S. R. 2003 Jamming at zero temperature and zero applied stress: the epitome of disorder. *Phys. Rev.* E **68** (1), 011306.

PITOIS, O., MOUCHERONT, P. & CHATEAU, X. 2000 Liquid bridge between two moving spheres: an experimental study of viscosity effects. *J. Colloid Interface Sci.* **231**, 26–31.

QUARTIER, L., ANDREOTTI, B., DOUADY, S. & DAERR, A. 2000 Dynamics of a grain on a sandpile model. *Phys. Rev.* E **62** (6), 8299.

RAHBARI, S. H. E., VOLLMER, J., HERMINGHAUS, S. & BRINKMANN, M. 2009 A response function perspective on yielding of wet granular matter. *Europhys. Lett.* **87** (1), 14002.

RAHBARI, S. H. E., VOLLMER, J., HERMINGHAUS, S. & BRINKMANN, M. 2010 Fluidization of wet granulates under shear. *Phys. Rev.* E **82** (6), 061305.

REMY, B., KHINAST, J. G. & GLASSER, B. J. 2012. Wet granular flows in a bladed mixer: experiments and simulations of monodisperse spheres, *AIChE J.* (submitted).

REN, J., DIJKSMAN, J. A. & BEHRINGER, R. P. 2011 Linear shear in a model granular system. *CHAOS*.

ROELLER, K. 2010. Numerical simulations of wet granular matter. PhD thesis, University Goettingen.

ROELLER, K., VOLLMER, J. & HERMINGHAUS, S. 2009 Unstable Kolmogorov flow in granular matter. *CHAOS* **19** (4), 041106.

ROGNON, P. G., ROUX, J.-N., NAAÏM, M. & CHEVOIR, F. 2008 Dense flows of cohesive granular materials. *J. Fluid Mech.* **596**, 21–47.

ROGNON, P. G., ROUX, J.-N., WOLF, D., NAAÏM, M. & CHEVOIR, F. 2006 Rheophysics of cohesive granular materials. *Eur. Phys. Lett.* **74** (4), 644.

SCHALL, P. & VAN HECKE, M. 2010 Shear bands in matter with granularity. *Annu. Rev. Fluid Mech.* **42** (1), 67–88.

SCHULZ, B. M. & SCHULZ, M. 2006 The dynamics of wet granular matter. *J. Non-Crystalline Solids* **352** (42–49), 4877–4879.

SCHULZ, M., SCHULZ, B. M. & HERMINGHAUS, S. 2003 Shear-induced solid–fluid transition in a wet granular medium. *Phys. Rev.* E **67** (5), 052301.

SILBERT, L. E., ERTAŞ, D., GREST, G. S., HALSEY, T. C., LEVINE, D. & PLIMPTON, S. J. 2001 Granular flow down an inclined plane: Bagnold scaling and rheology. *Phys. Rev.* E **64** (5), 051302.

SLOTTERBACK, S., MAILMAN, M., RONASZEGI, K., VAN HECKE, M., GIRVAN, M. & LOSERT, W. 2012 Onset of irreversibility in cyclic shear of granular packings. *Phys. Rev.* E **85** (2), 021309.

TORDESILLAS, A., LIN, Q., ZHANG, J., BEHRINGER, R. P. & SHI, J. 2011 Structural stability and jamming of self-organized cluster conformations in dense granular materials. *J. Mech. Phys. Solids* **59**, 265–296.

TRAPPE, V., PRASAD, V., CIPELLETTI, L., SEGRE, P. N. & WEITZ, D. A. 2001 Jamming phase diagram for attractive particles. *Nature* **411**, 772–775.

ULRICH, S., ASPELMEIER, T., ROELLER, K., FINGERLE, A., HERMINGHAUS, S. & ZIPPELIUS, A. 2009*a* Cooling and aggregation in wet granulates. *Phys. Rev. Lett.* **102** (14), 148002.

ULRICH, S., ASPELMEIER, T., ZIPPELIUS, A., ROELLER, K., FINGERLE, A. & HERMINGHAUS, S. 2009*b* Dilute wet granular particles: nonequilibrium dynamics and structure formation. *Phys. Rev.* E **80** (3), 031306.

UTTER, B. & BEHRINGER, R. P. 2008 Experimental measures of affine and nonaffine deformation in granular shear. *Phys. Rev. Lett.* **100**, 208302.

VALVERDE, J. M., QUINTANILLA, M. A. S. & CASTELLANOS, A. 2004 Jamming threshold of dry fine powders. *Phys. Rev. Lett.* **92** (25), 258303.

ZHANG, J., MAJMUDAR, T. S., TORDESILLAS, A. & BEHRINGER, R. P. 2010 Statistical properties of a 2D granular material subjected to cyclic shear. *Granul. Matt.* **12** (2), 159–172.

# Breath Figures: Nucleation, Growth, Coalescence, and the Size Distribution of Droplets

Johannes Blaschke,[1,2] Tobias Lapp,[1,2] Björn Hof,[1] and Jürgen Vollmer[1,2]
[1]*Max-Planck-Institut für Dynamik und Selbstorganisation (MPIDS), 37077 Göttingen, Germany*
[2]*Fakultät für Physik, Georg-August-Universität Göttingen, 37077 Göttingen, Germany*
(Received 27 March 2012; published 10 August 2012)

The analysis of the size distribution of droplets condensing on a substrate (breath figures) is a test ground for scaling theories. Here, we show that a faithful description of these distributions must explicitly deal with the growth mechanisms of the droplets. This finding establishes a gateway connecting nucleation and growth of the smallest droplets on surfaces to gross features of the evolution of the droplet size distribution.

DOI: 10.1103/PhysRevLett.109.068701 PACS numbers: 68.43.Jk, 05.65.+b, 89.75.Da

Classical questions regarding breath figures involve the influence of material defects and impurities on the droplet patterns [1–5]. Presently, they are used as self-assembling templates in microfabrication [4,6–10] and as highly efficient means for heat exchange in cooling systems [5,11–13]. They are also promising candidates for water recovery in (semi-)arid regions [14,15]. For these applications, a detailed knowledge of the droplet size distribution and the average droplet growth speed is vital. Here, we demonstrate that the state of the art scaling theory [16–20] fails to describe data from simulations [21] and laboratory experiments [22], Fig. 1. A faithful description must, therefore, explicitly address the microscopic growth mechanisms of droplets.

Classical scaling [16,17] asserts that on clean surfaces the coagulation of droplets organizes the systems into a state where the number of droplets, $n(s, t)$, per unit droplet volume and surface area takes a universal scaling form,

$$n(s, t) = s^{-\theta} f\left(\frac{s}{S}\right), \quad \text{with } S = S(t). \tag{1a}$$

Here, $s$ denotes the droplet volume, $\theta$ is a scaling exponent, $f(x)$ is a dimensionless function, and $S(t)$ is the volume of the largest droplets encountered at time $t$, i.e., the average volume of droplets in the *bump* of the distributions shown in Fig. 1.

Since $n(s, t)$ has a dimension of length to the power $-5$ the exponent $\theta$ must be set to a value of $\theta = 5/3$ [17–19]. The time evolution of $S(t)$ is found by observing that the total volume of all droplets grows linearly in time when a constant volume flux impinges onto the surface. In agreement with experimental and numerical observation [17–19], this entails $S(t) \sim t^3$. Moreover, a lower cutoff to the scaling at a scale $s_0/S$ has been accounted for by a polydispersity exponent $0 < \tau < 2$ [23]. For our numerical scheme, where the mass flux onto the surface is implemented as sustained addition of droplets of size $s_0$ to random positions of the surface and where overlapping droplets are subsequently merged [22], it was predicted [20] to be

$$x \ll 1 \Rightarrow f(x) \sim x^{\theta-\tau}, \qquad \tau = 19/12. \tag{1b}$$

The scaling, Eq. (1a), provides an excellent data collapse of the *bump* and the *dip* of the numerical, Fig. 1(a), and the experimental data, Fig. 1(b). Beyond the *dip* one can discern a self-similar scaling regime, Eq. (1b), in the numerical data, and in only those experimental data with the vastest range of droplet sizes. On the other hand, in either case—and particularly pronounced in the experimental data—noticeable deviations, *tails*, from the scaling prediction arise for small values of $s/S$.

In the following, we show that these deviations result from features of droplet growth at the small length scale, $s_0$. Similar to the approaches in the theory of critical phenomena [24,25] or of the effect of rough boundaries in turbulent flows [26,27], scaling will be recovered by asymptotic analysis [28], which allows us to explicitly account for different growth mechanisms of small droplets. Universal and nonuniversal features of the asymptotic droplet density distribution will be disentangled by discussing the consequences of the different growth mechanisms for the small droplets in the numerical and experimental setting, respectively.

*Relation to fractal packings.*—To explore the role of the lower cutoff of scaling, we consider the droplet arrangement in breath figures as an example of a fractal packing of disks (see [29–31] for recent applications in other fields), and adopt scaling arguments developed to characterize (disordered) fractal structures to the problem at hand: We assert that in the scale-separation limit, $s_0 \ll S$, the free surface area, i.e., the area not covered by droplets, approaches a fractal with a fractal dimension $d_f < 2$. Self-similarity with fractal dimension $d_f$ amounts, then, to the statement that in an area of size $S^{2/3}$ a number

$$N(s_*, S) \sim \left(\frac{S^{1/3}}{s_*^{1/3}}\right)^{d_f} = \left(\frac{s_*}{S}\right)^{-d_f/3} \tag{2}$$

of regions of size $s_*^{2/3}$ are required to cover the complement of the surface area covered by all droplets larger than $s_*$.

 

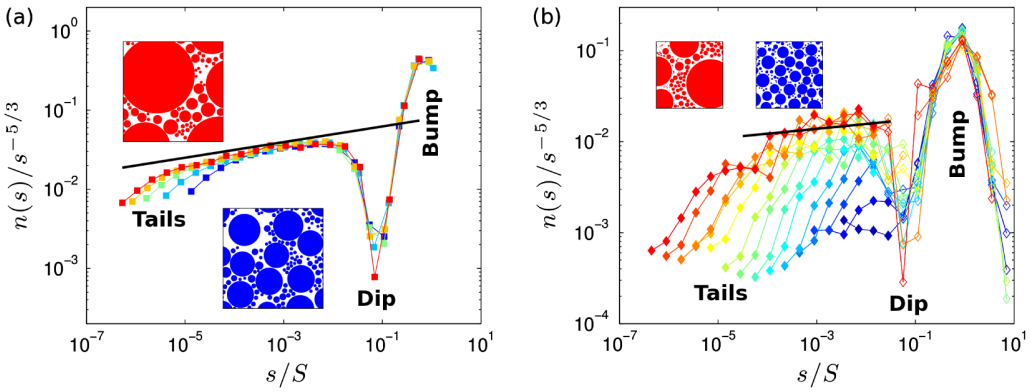


FIG. 1 (color online). Scaling plots of the droplet number density $n(s, t)$ for (a) numerical and (b) experimental data, for (a) $8 \times 10^6$ (rightmost *tails*), $12 \times 10^6$, $16 \times 10^6$, $20 \times 10^6$, and $24 \times 10^6$ (leftmost *tails*) droplets added to a domain of size $1600 \times 1600$ [22], and (b) water droplets on a polyethylene film [21] where eventually the droplet diameters cover the range from a few microns to a few millimeters. The respective positions of the *tail*, *dip*, and *bump* of the distributions are indicated, and the slope, $\theta - \tau = 1/12$, of the scaling prediction, [Eq. (1b)], is shown by solid lines. The insets show snapshots of the breath figures at an early [blue, (lower) right] and a late [red, left] time, respectively. Movies of their time evolution and full details of data assimilation and evaluation, as well as plots of the raw data are given in the Supplemental Material [22].

The fraction of this area in the considered domain of size $S^{2/3}$ amounts to

$$p(s_*, S) = N(s_*, S)\frac{s_*^{2/3}}{S^{2/3}} \sim \left(\frac{s_*}{S}\right)^{(2-d_f)/3}. \tag{3}$$

Following [29], we denote the surface area not covered by droplets as *porosity*, $p(t)$. It is obtained by evaluating Eq. (3) for the size $s_0$ characterizing the small-scale cutoff of the fractal, $p(t) = p(s_0, S(t))$.

By its definition the porosity is related the area $A_d$ covered by droplets in a region of area $A_s$ via $p(t) = 1 - A_d/A_s$: when the surface area in between droplets approaches a fractal of zero measure one obtains

$$\int_{s_0}^{\infty} a(s)n(s, t)ds \equiv \frac{A_d}{A_s} = 1 - p(t) \xrightarrow{s_0/S \to 0} 1,$$

where $a(s)$ denotes the area covered by droplets of size $s$. Using Eq. (1a) with $\theta = 5/3$, Eq. (1b), $a(s) \sim s^{2/3}$, and introducing $x = s/S$ one obtains

$$p(t) = 1 - \frac{A_d}{A_s} \sim \int_0^{s_0/S} x^{-1} f(x)\, dx \sim \int_0^{s_0/S} x^{\theta-\tau-1} dx = \left(\frac{s_0}{S(t)}\right)^{\theta-\tau}, \tag{4}$$

and comparing Eqs. (4) and (3) yields

$$\theta - \tau = (2 - d_f)/3. \tag{5}$$

Hence, the nontrivial scaling, Eq. (1b), of $f(x)$ for small $x$ reflects the fractality of the arrangements of droplets in breath figures with a large scale separation $s_0 \ll S$, that can faithfully be regarded as a fractal.

This provides an independent, more accurate means to test the polydispersity exponent: For $\tau = 19/12$ and $S \sim t^3$, Eq. (4) implies $p(t) \sim t^{-1/4}$. Remarkably, none of our data follow this prediction [Figs. 1(b) and 5(b) in the Supplemental Material [22]]. Rather than $1/4$, we find 0.30 for the numerical and 0.16 for the experimental data.

Hence, the different microphysics of droplet growth and merging leads to (slightly) different fractal dimensions and a different small-scale cutoff of scaling. To disentangle the intermediate self-similar scaling regime from the large scale (arising from the first generation of droplets, cf. [32]) and the small-scale physics, we introduce cutoff functions $\hat{f}(s/S)$ and $\hat{g}(s/s_0)$ for large and small droplets, respectively. $\hat{f}(x) \equiv f(x)/x^{\theta-\tau}$ takes a constant value $\hat{f}_0$ for $x \ll 1$, and it accounts for the *dip* and the *bump* in $n(s, t)$ for $s \simeq S$. Similarly, $\hat{g}(s/s_0)$ accounts for the *tails* of $n(s, t)$. As shown in the insets of Fig. 2, it approaches constant values for $s \gg s_0$, and it takes a scaling form for all times. To arrive at a complete description of the droplet size distribution, we further discuss this lower cutoff.

*Incorporating the lower cutoff.*—We start by writing the total volume of droplets of size $s$ per unit volume $ds$ and unit surface area in the form

$$s\, n(s, t) = S^{-2/3}\left(\frac{s}{S}\right)^{-d_f/3} \hat{f}(s/S)\, \hat{g}(s/s_0). \tag{6}$$

This expression states that in the scaling regime $s_0 \ll s \ll S$ the overall volume of droplets of size $s$ on an area of size $S^{2/3}$ is proportional to the number of droplets, Eq. (2), of the considered size.

In equation (6) the fractal dimension $d_f$ and the function $\hat{g}(s/s_0)$ are *not* universal. We, henceforth, adopt the values for $d_f$ determined by fitting the porosity, and we follow the evolution of droplets smaller than $s_*$ over a small time interval from $t$ to $t + dt$ in order to relate the form of

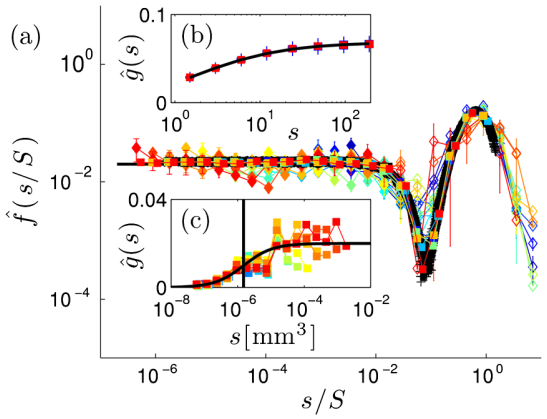


FIG. 2 (color online). Master plot of the universal cutoff function, $\hat{f}(s/S)$, which comprises all numerical and experimental data shown in Fig. 1 (using the same symbols), as well as additional numerical data shown as black crosses (every $5 \times 10^4$ frames of 44 runs where $4.23 \times 10^7$ droplets are added eventually). The insets show $\hat{g}(s)$ for (b) numerical and (c) experimental data at all times. Their shapes (solid lines) reflect the respective small-scale droplet growth mechanisms, Eqs. (10) and (11). The vertical line in (c) marks $s_0$.

$\hat{g}(s/s_0)$ to different nucleation and growth mechanisms of small droplets. Let the considered area on the substrate and the time interval $dt$ be chosen such that this growth is not influenced by the merging of droplets larger than $s_*$. When $s_*$ is so small that $\hat{f}(s_*/S)$ takes the constant value $\hat{f}_0$, Eq. (6) entails

$$s_* \, n(s_*, t) = \hat{f}_0 \, S^{-2/3} \left(\frac{s_*}{S}\right)^{-d_f/3} \hat{g}(s_*/s_0).$$

In order to determine $\hat{g}(s_*/s_0)$ we observe that the volume density of the droplets smaller than $s_*$ amounts to the cumulative distribution

$$V(s_*) = \int_{s_0}^{s_*} s n(s,t) ds = \frac{\hat{f}_0}{S^{2/3}} \int_{s_0}^{s_*} \left(\frac{s}{S}\right)^{-d_f/3} \hat{g}(s/s_0) ds. \quad (7)$$

For values of $s_*$ in the scaling regime the increase of volume is accounted for by increasing the integral domain. Therefore, an infinitesimal increase of $s_*$ to $s_* + \dot{s}\, dt$ in the time interval $dt$ amounts to an increase of the volume density of droplets,

$$\frac{dV}{dt} = \frac{V(s_* + \dot{s}dt) - V(s_*)}{dt} = \frac{\hat{f}_0}{S^{2/3}} \left(\frac{s_*}{S}\right)^{-d_f/3} \hat{g}(s_*/s_0)\, \dot{s}. \quad (8a)$$

On the other hand, this change must be due to the volume flux $\Phi$ onto the fraction of area covered by droplets,

$$\frac{dV}{dt} = p(s_*, S)\Phi \sim \left(\frac{s_*}{S}\right)^{(2-d_f)/3} \Phi. \quad (8b)$$

Equating the expressions for $dV/dt$, Eqs. (8a) and (8b), and dropping the subscript $*$, one obtains

$$\hat{g}(s/s_0) \sim \frac{\Phi}{\hat{f}_0} \frac{s^{2/3}}{\dot{s}}. \quad (9)$$

This expression provides the desired connection of the average speed $\dot{s}$ of the growth of droplets of size $s$ to the form of the small-scale cutoff $\hat{g}(s/s_0)$ of $n(s, t)$: it explains how different microscopic droplet growth laws give rise to different nonuniversal cutoff functions $\hat{g}(s/s_0)$, and how the universal scaling is recovered for $s \gg s_0$. After all, the volume growth of large droplets in breath figures is always proportional to the area exposed to the surface flux [16,17,20], $\dot{s} \sim \Phi s^{2/3}$. Equation (9) allows us to disentangle universal and nonuniversal contributions to $n(s, t)$. This major finding of our theoretical treatment is now substantiated by working out the multiscaling predictions for the data shown in Fig. 1.

*Scaling numerical data.*—When a small droplet, of size $s_0$, has been added to the surface, it is merged with a droplet on the surface when the droplets overlap. As a consequence, a droplet of radius $s^{1/3}$ will capture small droplets of radius $s_0^{1/3}$, that are added in a distance smaller than $s^{1/3} + s_0^{1/3}$ from its center. In the absence of other droplets, this growth amounts to

$$\dot{s} \simeq \Phi \left[s^{1/3} + s_0^{1/3}\right]^2 = \Phi s^{2/3} \left[1 + \left(\frac{s_0}{s}\right)^{1/3}\right]^2.$$

The term in square brackets accounts for an enhanced growth of small droplets $s \gtrsim s_0$, which ceases rapidly for increasing $s$. In practice, the decay is even faster since the capture regions of neighboring droplets overlap. To fit the simulation data, Fig. 2(b), one needs a nontrivial prefactor 0.76 and an exponent close to 0.78 rather than 1/3,

$$\hat{g}(s/s_0) \simeq 0.07 \left[1 + 0.76 \left(\frac{s_0}{s}\right)^{0.78}\right]^{-2}. \quad (10)$$

Using Eq. (6) and $\theta - \tau = 0.3$ this provides a perfect data collapse of all numerical data, Fig. 2(a).

*Scaling experimental data.*—In the experimental setting, the growth rate of the droplets has two contributions. For small droplets, growth is limited by the diffusion of water molecules on the substrate towards the contact line of the droplet. As derived in [33] and observed in the experiments of [32], the radius of small droplets grows then like $r \sim t^{1/4}$, such that $\dot{s} \sim \Phi s^{-1/3}$. For larger droplets, the volume flux from the vapor phase onto the droplets is again proportional to the exposed droplet surface, such that $\dot{s} \sim \Phi s^{2/3}$. These growth contributions combine to

$$\dot{s} \sim \Phi s^{2/3} \left(1 + \frac{s_0}{s}\right) \Rightarrow \hat{g}(s/s_0) = b \left(1 + \frac{s_0}{s}\right)^{-1}, \quad (11)$$

where $s_0 \simeq 1.5 \times 10^{-6}$ mm$^3$ is the crossover size scale and $b \simeq 2 \times 10^{-2}$ is a normalization constant. Inserting Eq. (11) into Eq. (9) provides an excellent prediction for $\hat{g}(s/s_0)$, Fig. 2(c). Also, for the experimentally measured droplet size distributions, one obtains a perfect data collapse of the

appropriately scaled droplet number density $n(s, t)$ for all different times, Fig. 2(a).

*Discussion.*—For the numerical data, $s_0$ amounts to the volume of the smallest droplets in the system, Fig. 2(b), and for the experimental data it is about one order of magnitude larger than the smallest observed droplets, Fig. 2(c). In either case $\hat{g}(s)$ saturates for $s \gtrsim 10^2 s_0$. On the other hand the scaling behavior Eq. (1b) is only accessible for values of $s$ below the *dip* of the distribution, i.e., for $s \lesssim 10^{-2}$ S. It can, hence, only be resolved in simulations where $10^{-4} \ll s_0/S$, resulting in the observed scaling regime of about 1–2 decades, in the numerical data, Fig. 1(a), and in the experimental data with the largest accessible scale separation, Fig. 1(b).

Because of the relatively small scaling range, the droplet size distribution of breath figures cannot merely be idealized as a self-similar process with a single relevant length scale $S(t)$ [16–19]. Rather, one explicitly has to cope with the growth law of the smallest droplets in the system. Via its (slight) effect on the fractal dimension characterizing the free space in between the droplets, Eq. (5), it sets the value of the polydispersity exponent $\tau$, and it leads to massively different cutoff functions $\hat{g}(s/s_0)$, Figs. 2(b) and 2(c), that can completely dominate the shape of the droplet size distribution, Fig. 1(b).

When both the large scale and the small scale cutoffs are properly accounted for via Eqs. (10) and (11), a remarkable data collapse of all experimental *and* numerical data into a single plot is achieved, Fig. 2(a). This recovery of scaling establishes a novel gateway connecting features of the microscopic droplet growth on surfaces to gross features of the evolution of the droplet size distribution.

We are grateful to Bruno Eckhardt, Jens Eggers, Franziska Glaßmeier, Walter Goldburg, Siegfried Großmann, Andrew Scullion, and Stephan Herminghaus for enlightening discussions, and to our referee for very valuable feedback on the manuscript.

[1] Rayleigh, Nature (London) **86**, 416 (1911); J. Aitken, *ibid.* **90**, 619 (1913).
[2] T. J. Baker, Philos. Mag. Ser. 6 **44**, 752 (1922).
[3] G. P. Lopez, H. A. Biebuyck, C. D. Frisbie, and G. M. Whitesides, Science **260**, 647 (1993).
[4] J. Lepopoldes and P. Damman, Nature Mater. **5**, 957 (2006).
[5] B. S. Sikarwar, N. K. Battoo, S. Khandekar, and K. Muralidhar, J. Heat Transfer **133**, 021501 (2011).
[6] A. Böker *et al.*, Nature Mater. **3**, 302 (2004).
[7] M. Haupt, S. Miller, R. Sauer, K. Thonke, A. Mourran, and M. Moeller, J. Appl. Phys. **96**, 3065 (2004).
[8] Y. Wang, A. S. Özcan, C. Sanborn, K. F. Ludwig, and A. Bhattacharyya, J. Appl. Phys. **102**, 073522 (2007).
[9] K. Rykaczewski, J. Chinn, M. L. Walker, J. H. J. Scott, A. Chinn, and W. Jones, ACS Nano **5**, 9746 (2011).
[10] A. Z. Samuel, S. Umapathy, and S. Ramakrishnan, ACS Appl. Mater. Interfaces **3**, 3293 (2011).
[11] M. Mei, B. Yu, M. Zou, and L. Luo, Int. J. Heat Mass Transfer **54**, 2004 (2011).
[12] R. N. Leach, F. Stevens, S. C. Langford, and J. T. Dickinson, Langmuir **22**, 8864 (2006).
[13] J. W. Rose and L. R. Glicksman, Int. J. Heat Mass Transfer **16**, 411 (1973).
[14] I. Lekouch, M. Muselli, B. Kabbachi, J. Ouazzani, I. Melnytchouk-Milimouk, and D. Beysens, Energy **36**, 2257 (2011).
[15] V. Nikolayev, D. Beysens, A. Gioda, I. Milimouka, E. Katiushin, and J.-P. Morel, J. Hydrol. **182**, 19 (1996).
[16] D. Beysens, A. Steyer, P. Guenoun, D. Fritter, and C. Knobler, Phase Transit. **31**, 219 (1991).
[17] P. Meakin, Rep. Prog. Phys. **55**, 157 (1992).
[18] J. L. Viovy, D. Beysens, and C. M. Knobler, Phys. Rev. A **37**, 4965 (1988).
[19] F. Family and P. Meakin, Phys. Rev. A **40**, 3836 (1989).
[20] J. A. Blackman and S. Brochard, Phys. Rev. Lett. **84**, 4409 (2000).
[21] Droplet patterns are obtained from water droplets suspended from a polyethylene film covering a glass plate kept at a temperature of 20 °C which is placed about 5 cm atop a water bath with a temperature of 60 °C. See Supplemental Material at http://link.aps.org/supplemental/10.1103/PhysRevLett.109.068701 for details on the experimental method as well as raw data and a movie of the evolution.
[22] See Supplemental Material at http://link.aps.org/supplemental/10.1103/PhysRevLett.109.068701 for full details on the numerical method as well as raw data and a movie of the evolution.
[23] S. Cueille and C. Sire, Phys. Rev. E **55**, 5465 (1997).
[24] L. P. Kadanoff, W. Götze, D. Hamblen, R. Hecht, E. A. S. Lewis, V. V. Palciauskas, M. Rayl, J. Swift, D. Aspnes, and J. Kane, Rev. Mod. Phys. **39**, 395 (1967).
[25] R. Hilfer, Phys. Rev. Lett. **68**, 190 (1992).
[26] G. I. Barenblatt and A. J. Chorin, Proc. Natl. Acad. Sci. U.S.A. **101**, 15 023 (2004).
[27] N. Goldenfeld, Phys. Rev. Lett. **96**, 044503 (2006).
[28] G. I. Barenblatt, *Scaling* (Cambridge University Press, New York, 2003).
[29] H. J. Herrmann, G. Mantica, and D. Bessis, Phys. Rev. Lett. **65**, 3223 (1990); S. S. Manna and H. J. Herrmann, J. Phys. A **24**, L481 (1991); S. D. S. Reis, N. A. M. Araújo, J. S. Andrade, Jr., and H. J. Herrmann, Europhys. Lett. **97**, 18004 (2012).
[30] A. Amirjanov and K. Sobolev, Model. Simul. Mater. Sci. Eng. **14**, 789 (2006).
[31] F. Varratoa and G. Foffia, Mol. Phys. **109**, 2663 (2011).
[32] D. Fritter, C. M. Knobler, and D. A. Beysens, Phys. Rev. A **43**, 2858 (1991).
[33] T. M. Rogers, K. R. Elder, and R. C. Desai, Phys. Rev. A **38**, 5303 (1988).

# Acknowledgements

I would like to thank apl. Prof. Dr. Jürgen Vollmer for his academic guidance over the years. His ability to distil very complicated physical problems into their elegant essence has made this dissertation possible. Our discussions where extremely insightful and have shaped my understanding of the physical world.

I also would like to thank Christin Büchner, above all for her emotional and moral support. She has given me an infinite reservoir of strength that has helped me to complete this work. I also thank her for proof-reading the earliest versions of this dissertation.

For proof-reading, I would like to thank James Clewett and Artur Wachtel. They are excellent teachers. Our interesting and fruitful discussions have helped improve the sanity and the quality of this dissertation.

For their scientific guidance, and for the interesting discussions, I would like to thank Bernhard Altaner and Laura Stricker. Their advice has guided my research and helped me evaluate my findings in a new light.

# Bibliography


[1] D Abbott, B R Davis, and JMR Parrondo. The problem of detailed balance for the Feynman-Smoluchowski engine (FSE) and the multiple pawl paradox. *AIP Conference Proceedings*, 511:213–218, 2000.

[2] R Dean Astumian. Thermodynamics and kinetics of a Brownian motor. *Science*, 276(5314):917–922, 1997.

[3] A Barrat, A Puglisi, E Trizac, P Visco, and F Van Wijland. *Fluctuations in granular gases*. Mathematical Models of Granular Matter. Springer, 2008.

[4] E Ben-Naim, B Machta, and J Machta. Power-law velocity distributions in granular gases. *Phys. Rev. E*, 72(2):021302, August 2005.

[5] Johannes Blaschke and Jürgen Vollmer. Granular Brownian motors: Role of gas anisotropy and inelasticity. *Phys. Rev. E*, 87(4):040201, April 2013.

[6] S I Blinnikov and R Moessner. Expansions for nearly Gaussian distributions. *Astron. Astrophys. Suppl. Ser.*, 130(astro-ph/9711239. MPA-1051):193–205. 13 p, November 1997.

[7] Sydney Chapman and T G Cowling. *The Mathematical Theory of Non-uniform Gases*. An Account of the Kinetic Theory of Viscosity, Thermal Conduction and Diffusion in Gases. Cambridge University Press, 1970.

[8] B Cleuren and Christian Van den Broeck. Granular Brownian motor. *EPL*, 77(5):50003, January 2007.

[9] Bart Cleuren and Ralf Eichhorn. Dynamical properties of granular rotors. *J Stat Mech-Theory E*, 2008(10):P10011, 2008.

[10] James P D Clewett, Klaus Roeller, R M Bowley, Stephan Herminghaus, and Michael R Swift. Emergent Surface Tension in Vibrated, Noncohesive Granular Media. *Phys. Rev. Lett.*, 109(22), 2012.

[11] G Costantini, U M B Marconi, and A Puglisi. Noise rectification and fluctuations of an asymmetric inelastic piston. *EPL*, 82(5): 50008, 2008.

[12] G Costantini, A Puglisi, and U M B Marconi. Granular ratchets. *Eur. Phys. J. Spec. Top.*, 179(1):197–206, May 2010.

[13] Giulio Costantini, Umberto Marini Bettolo Marconi, and Andrea Puglisi. Granular Brownian ratchet model. *Phys. Rev. E*, 75(6):061124, June 2007.

[14] Bruno Crosignani and Paolo Di Porto. Random Fluctuations of Diathermal and Adiabatic Pistons. *Found Phys*, 37(12): 1707–1715, August 2007.

[15] R Di Leonardo, L Angelani, D Dell'Arciprete, G Ruocco, V Iebba, S Schippa, M P Conte, F Mecarini, F De Angelis, and E Di Fabrizio. Bacterial ratchet motors. *Proc. Natl. Acad. Sci. U.S.A.*, 107(21):9541–9545, 2010.

[16] Peter Eshuis, Ko van der Weele, Devaraj van der Meer, and Detlef Lohse. Granular Leidenfrost Effect: Experiment and Theory of Floating Particle Clusters. *Phys. Rev. Lett.*, 95(25): 258001, December 2005.

[17] Peter Eshuis, Devaraj van der Meer, Meheboob Alam, Henk Jan van Gerner, Ko van der Weele, and Detlef Lohse. Onset of Convection in Strongly Shaken Granular Matter. *Phys. Rev. Lett.*, 104(3):038001, January 2010.

[18] Peter Eshuis, Ko van der Weele, Detlef Lohse, and Devaraj van der Meer. Experimental Realization of a Rotational Ratchet in a Granular Gas. *Phys. Rev. Lett.*, 104(24):248001, June 2010.

[19] Harley Flanders. Differentiation Under the Integral Sign. *The American Mathematical Monthly*, 80(6):615, June 1973.

[20] Crispin W Gardiner. *Handbook of stochastic methods: for physics, chemistry and the natural sciences; 2nd ed.* Springer series in synergetics. Springer, Berlin, 1997.

[21] Eric A Gislason. A close examination of the motion of an adiabatic piston. *American Journal of Physics*, 78(10):995–1001, 2010.

[22] A Gnoli, A Petri, F Dalton, G Gradenigo, G Pontuale, A Sarracino, and A Puglisi. Brownian ratchet in a thermal bath driven by Coulomb friction. *arXiv*, November 2012.

[23] C Gruber and J Piasecki. Stationary motion of the adiabatic piston. *Physica A*, 268(3):412–423, 1999.

[24] P K Haff. Grain flow as a fluid-mechanical phenomenon. *Journal of Fluid Mechanics*, 1983.

[25] Peter Hänggi. Artificial Brownian motors: Controlling transport on the nanoscale. *Rev. Mod. Phys.*, 81(1):387–442, March 2009.

[26] R J Harris and G M Schütz. Fluctuation theorems for stochastic dynamics. *J Stat Mech-Theory E*, 2007(07):P07020–P07020, July 2007.

[27] K Huang, K Roeller, and S Herminghaus. Universal and non-universal aspects of wet granular matter under vertical vibrations. *Eur. Phys. J. Spec. Top.*, 179(1):25–32, May 2010.

[28] S Joubaud, D Lohse, and Devaraj van der Meer. Fluctuation theorems for an asymmetric rotor in a granular gas. *Phys. Rev. Lett.*, 108(21):210604, 2012.

[29] Ryoichi Kawai, Antoine Fruleux, and Ken Sekimoto. A hard disc analysis of momentum deficit due to dissipation. *Phys. Scr.*, 86(5):058508, October 2012.

[30] Stefan Luding. Towards dense, realistic granular media in 2D. *Nonlinearity*, 22(12):R101–R146, 2009.

[31] Marcelo O Magnasco and Gustavo Stolovitzky. Feynman's Ratchet and Pawl. *Journal of Statistical Physics*, 93(3-4): 615–632, May 1998.

[32] U Marconi, A Puglisi, and L Rondoni. Fluctuation-dissipation: Response theory in statistical physics. *Phys. Rep.*, January 2008.

[33] J Clerk Maxwell. On the Dynamical Theory of Gases. *Phil. Trans. R. Soc. Lond.*, 157(0):49–88, January 1867.

[34] P Meurs and Christian Van den Broeck. Thermal Brownian motor. *J. Phys. Cond. Mat.*, 17:S3673, 2005.

[35] P Meurs, Christian Van den Broeck, and A Garcia. Rectification of thermal fluctuations in ideal gases. *Phys. Rev. E*, 70:051109, January 2004.

[36] R M Mnatsakanov. Hausdorff moment problem: Reconstruction of probability density functions. *Statistics & Probability Letters*, 78(13):1869–1877, 2008.

[37] R M Neal. Slice Sampling. *Annals of statistics*, 2003.

[38] Kiri Nichol and Karen Daniels. Equipartition of Rotational and Translational Energy in a Dense Granular Gas. *Phys. Rev. Lett.*, 108(1), January 2012.

[39] J Piasecki and C Gruber. From the adiabatic piston to macroscopic motion induced by fluctuations. *Physica A*, 265(3): 463–472, 1999.

[40] J Piasecki, J Talbot, and P Viot. Exact solution of a one-dimensional Boltzmann equation for a granular tracer particle. *Physica A*, 373:313–323, January 2007.

[41] Andrea Puglisi, Paolo Visco, Emmanuel Trizac, and Frédéric van Wijland. Dynamics of a tracer granular particle as a nonequilibrium Markov process. *Phys. Rev. E*, 73(2):021301, February 2006.

[42] Peter Reimann. Brownian motors: noisy transport far from equilibrium. *Phys. Rep.*, 361(2):57–265, 2002.

[43] H Risken and H D Vollmer. On solutions of truncated Kramers-Moyal expansions; continuum approximations to the Poisson process. *Z. Physik B - Condensed Matter*, 66(2):257–262, 1987.

[44] Hannes Risken. *The Fokker-Planck Equation*. Methods of Solution and Applications. Springer Verlag, Berlin, January 1989.

[45] Klaus Roeller, James P. D. Clewett, R. M. Bowley, Stephan Herminghaus, and Michael R. Swift. Liquid-Gas Phase Separation in Confined Vibrated Dry Granular Matter. *Phys. Rev. Lett.*, 107(4):048002, July 2011.

[46] J R Royer, D.J. Evans, L Oyarte, Q Guo, E Kapit, M E Möbius, S R Waitukaitis, and H M Jaeger. High-speed tracking of rupture and clustering in freely falling granular streams. *Nature*, 459(7250):1110–1113, 2009.

[47] Thomas Schwager and Thorsten Pöschel. Coefficient of restitution and linear–dashpot model revisited. *Granular Matter*, 9 (6):465–469, October 2007.

[48] Udo Seifert. Entropy Production along a Stochastic Trajectory and an Integral Fluctuation Theorem. *Phys. Rev. Lett.*, 95(4): 040602, July 2005.

[49] Udo Seifert. Stochastic thermodynamics, fluctuation theorems and molecular machines. *Rep. Prog. Phys.*, 75(12):126001, November 2012.

[50] Susan Sporer, Christian Goll, and Klaus Mecke. Motion by stopping: Rectifying Brownian motion of nonspherical particles. *Phys. Rev. E*, 78(1):011917, 2008.

[51] Julian Talbot, Alexis Burdeau, and Pascal Viot. Analysis of a class of granular motors in the Brownian limit. *Phys. Rev. E*, 82(1):011135, July 2010.

[52] Christian Van den Broeck and R Kawai. Brownian Refrigerator. *Phys. Rev. Lett.*, 96(21):210601, June 2006.

[53] Devaraj van der Meer and P Reimann. Temperature anisotropy in a driven granular gas. *EPL*, 74(3):384–390, January 2007.

[54] Artur Wachtel. Fluctuation Spectra and Coarse Graining in Stochastic Dynamics. *arXiv*, November 2013.